GROWTH AND CHARACTERIZATION OF EPITAXIAL GRAPHENE FILMS BY MOLECULAR BEAM EPITAXY

BY

CHANDRA SHEKHAR MOHAPATRA

DISSERTATION

Submitted in partial fulfillment of the requirements
for the degree of Doctor of Philosophy in Physics
in the Graduate College of the
University of Illinois at Urbana-Champaign, 2012

Urbana, Illinois

Doctoral Committee:

Associate Professor Nadya Mason, Chair
Professor James N Eckstein, Director of Research
Associate Professor Smitha Vishveshwara
Professor John D Stack

ABSTRACT

Growing macroscopic graphene films with the aim of making graphene commerically viable is being researched a lot recently. Although graphene isolated by exfoliation of Highly Oriented Pyrolytic Graphite (HOPG) crystals has been in place for sometime now, its micro sample size has triggered the research to produce wafer-scale graphene films. Chemical Vapor Deposition (CVD) of graphene on metallic substrates and thermal decomposition of SiC are two such efforts in the direction of producing wafer-scale graphene films but none of these techniques are full-proof. While CVD graphene needs to be transferred from a metallic substrate to an insulating one for device applications, graphene synthesized through thermal decomposition relies so much on the rate of Silicon (Si) sublimation that getting a uniform graphene coverage remains a challenge.

In this dissertation, I attempt to grow epitaxial graphene by Molecular Beam Epitaxy (MBE) by depositing Carbon (C) from a high purity solid graphite source where the growth rate of graphene, the rate of deposition and the substrate temperature can be controlled independently. In this research work, I studied the growth of graphene on two substrates with hexagonal symmetry: c-plane sapphire and 4H-SiC $(000\bar{1})$. Both these substrates are decently lattice matched to graphene. The dynamics of the growth process which is dependent on the substrate used is studied in detail. It will be reported that in both the substrates, the growth starts in an epitaxial manner and progresses to being polycrystalline with increase of thickness. The MBE grown films are systematically analyzed with in-situ RHEED, ex-situ XPS, AFM, Raman Spectroscopy and Electrical Transport.

Clear evidence of tensile stress is seen in the AFM and Raman studies in the

graphene films grown on c-plane sapphire. Whereas, Raman studies confirm the presence of compressive stress in the graphene films grown on 4H-SiC $(000\bar{1})$ where the mismatch of the coefficient of thermal expansion (CTE) plays an important role. Raman studies show a clear evidence of the defect peak (D) in all the films grown on c-plane sapphire no matter how smooth the morphology is. However, the D peak is absent in very thin epitaxial graphene grown on 4H-SiC $(000\bar{1})$ substrates. The symmetrical nature of the 2D peak in the Raman studies of multi-layered graphene films grown on both c-plane sapphire and 4H-SiC $(000\bar{1})$ indicate the presence of random stacking order. Electrical transport in both the classes of graphene films shows a non-metallic behavior: power law behavior in the high temperature regime and a generalized Variable Range Hopping (VRH) type behavior at low temperatures. The low temperature transport of graphene grown on c-plane sapphire will be shown to be an interplay of both 2D and 3D Mott VRH. Whereas, Efros Shklovskii VRH plays a dominant role in the low temperature transport of graphene grown on 4H-SiC $(000\bar{1})$. With all these findings in mind, some potential solutions are proposed which would take this research forward.

To my family, for their love and support.

ACKNOWLEDGMENTS

First and foremost, I would like to thank my research advisor Prof Jim Eckstein, whose continuous support and inspiration made it possible for this project to become a reality. I still recall his words in his email to me 4.5 years back - "We have system D sitting in decent enough vacuum; lets grow graphene in it". I feel honored that he chose to entrust me with this challenging project and sharing with me his passion to explore newer physics in newer materials. The training and experience that I have gained all these years under his guidance has made me a better scientist.

I am grateful to my former lab-mates, Paul Welander and Xiaofang Zhai for their mentoring and for answering all my silly and curious questions. I can not forget the day I had joined the group and Paul introduced me to the UHV technology by saying - "Its all about opening a bunch of valves and closing another bunch". Xiaofang taught me a lot about oxide MBE, the training of which I carried forward into the present project of graphene MBE. I also thank Mike Vissers, Tim Mc Ardle and Kevin Inderhees who were always there to render any help I needed in fixing System D. Special thanks to Stephanie Law for creating that stimulating atmosphere at "our end of the tube". I thank all my fellow lab mates: Mao Zheng, Alison Dove, Gus Olson, Brian Mulcahy and Zack Yoscovits for their continued motivation and friendship. I offer my best wishes to the newcomers Can and Carolyn for a successful graduate career.

This project would have been incomplete without the expertise of several CMM staff. My sincere thanks to Doug Jeffers for all his help and encouragement in fixing the MBE system, especially the heater stage. I owe a lot to Steve Burdin

for his expertise in fixing the age-old Temescal electron gun control unit. Thanks to machinist, Jim Brownfield without whose help I could have never fixed the electron-gun water lines. I express my sincere thanks to Rick Haasch and Scott Mac Laren who have provided a lot of insight in explaining the results related to XPS and AFM respectively. I also thank Bharat Sankaran, Tao Shang and Mike Marshall in maintaining the instruments in the Microfab facility.

My deepest gratitude goes to my wonderful parents; Dad, Subash Chandra Mohapatra and Mom, Malati Mohapatra for their unflagging love and support. It always feels that they are right beside me even though they are almost 9,000 miles away. I can not help but admire the "never give up" spirit of my Mom, who has been fighting a tough battle against cancer for the last 8 years and still going strong. To my sister, Jolly I would like to thank her for all those light banter and encouragement. I would like to express my heartiest thanks to my lovely wife, Sucheta for being there for me through everything. The way she has been handling her graduate studies in Iowa and shuttling to Champaign every weekend during those intense weeks of experiments is commendable. Last but not the least, my deeply felt thanks to all my friends in Champaign-Urbana (Vikas, Tarun, Sonal, Adnan, Shilpa, Pritam, Mitrabhanu, Nachiket, Stanimir to mention a few) for creating such a warm social circle and making my stay here so enjoyable. A special thanks to my IIT-Physics friends who have stood by me through thick and thin from my undergraduate days. I am not able to mention all of your names here, but I would cherish your friendship for all the years to come.

TABLE OF CONTENTS

LIST OF TABLES

LIST OF FIGURES

LIST OF ABBREVIATIONS

HOPG	Highly Oriented Pyrolytic Graphite
MBE	Molecular Beam Epitaxy
ML	Mono Layer
CVD	Chemical Vapor Deposition
QCM	Quartz Crystal Monitor
RHEED	Reflection High Energy Electron Diffraction
AFM	Atomic Force Microscopy
XPS	X-ray Photoelectron Spectroscopy
AES	Auger Electron Spectroscopy
ARXPS	Angle Resolved X-ray Photoelectron Spectroscopy
VRH	Variable Range Hopping
WL	Weak Localization
CTE	Coefficient of Thermal Expansion
PMMA	Polymethyl Methacrylate
PET	Polyethylene Terephthalate
PBN	Pyrolytic Boron Nitride
MRL	Frederick Seitz Material Research Laboratory
CMM	Center for Microanalysis and Materials
IPA	Isopropyl Alcohol
TCE	Trichloro Ethylene

UHV	Ultra High Vacuum
STM	Scanning Tunneling Microscopy
LEED	Low Energy Electron Diffraction
FWHM	Full width at Half Maximum
BiSFET	Bilayer Pseudo Spin Field Effect Transistor
FET	Field Effect Transistor
CMP	Chemical Mechanical Polished

CHAPTER 1

INTRODUCTION

Graphene on an insulator has been elusive to the scientific community for a long time until 2004 when the Manchester group led by Nobel Laureates Geim and Novoselov isolated graphene on a Si/SiO_2 substrate exfoliated from the commercially available Highly Oriented Pyrolytic Graphite (HOPG) crystal. This method of isolating graphene is so easy and cost effective that it is adopted by researchers all over the world leading to an explosion of research efforts in order to understand the secrets of this new two dimensional material.

The great interest in graphene is mainly because of its unique electronic structure which shows a linear energy dispersion relation in the low energy region close to the Dirac points where the conduction band and the valence band meet at a point. This makes the charge carriers in graphene massless very similar to a photon. This is the reason why graphene becomes the perfect candidate where Quantum Electrodynamics can be studied in a condensed matter system. Because of the relativistic nature of the charge carriers which are chiral in nature, very interesting quantum phenomena have been experimentally observed. These include the anomalous Quantum Hall Effect and the observation of Berry's phase [24, 25] and the experimental observation of Klein tunneling in graphene p-n junctions [26]. Graphene being a natural two dimensional electron gas, the Quantum Hall Effect is so robust that it can be observed even at room temperatures [27]. Researchers have even observed Fractional Quantum Hall Effect in suspended graphene [28, 29]. The key paper that sparked the research explosion was the observation of electric field effect in atomically thin graphene [30]. Hall bars were fabricated on graphene and are found to have a mobility as high as 250,000 $\frac{cm^2}{V.s}$

[31]. This high mobility makes graphene the perfect material to fabricate terahertz transistors [32].

In addition to its outstanding electronic properties, graphene also has many exciting material properties. It is the strongest material ever measured with a breaking strength of 42 N/m and Young's Modulus of 1 TPa [33]. Graphene has a very high thermal conductivity [34] and is impermeable to gases including He [35].

As spectacular as these findings about graphene might sound, the underlying problem of manufacturing single layer graphene still persists. Obtaining a perfect sheet of atoms one layer thick spread over a wafer poses a lot of technical challenges. But, this is a key challenge if graphene has to be made commercially viable. In addition to the method of micro-mechanical cleavage of graphene from HOPG wafer (already described), there are two other methods which are actively researched for large-scale manufacturing capabilities : Chemical Vapor Deposition (CVD) of graphene onto transition metals and thermal decomposition of SiC. Micro-mechanical cleavage being the simplest is the most popular method which yields graphene samples that are micro-sized and hence limited to academic use. CVD of graphene on transition metal substrates has the potential to produce macro-sized graphene samples defined by the dimension of the underlying metallic substrate. But, the CVD grown graphene needs to be transferred to an insulating substrate to be put to device applications which is a non-trivial process. Growth of graphene on SiC by thermal decomposition is more promising since the graphene is directly grown on an insulator and can potentially produce macro-sized graphene films. But, this method of graphene growth relies too much on the rate of Si sublimation which is responsible for graphene formation. Hence, getting a uniform coverage of graphene over the dimension of SiC wafer is not easy here. All these techniques of graphene production will be described in detail in the next chapter.

In an effort to circumvent some of the existing problems in graphene synthesis, I attempt to grow graphene by depositing Carbon (C) on insulating substrates

from a high purity Carbon source by Molecular Beam Epitaxy (MBE). The usage of MBE in the area of semiconductors is not new. Independent control over the growth rate of carbon and the substrate temperature can be achieved in an MBE growth process. This is missing in the growth of graphene by thermal decomposition of SiC. Not only sub-monolayer level accuracy can be achieved by MBE, but also the presence of multiple source materials at disposal make the growth of graphene based heterostructures possible. This is the basic motivating factor on the basis of which the research presented in this dissertation is undertaken. The motivation and the technical aspects of the MBE growth process are presented in greater detail in Chapter 3.

As is true for any MBE growth process, a substrate which satisfies the epitaxy with the material to be grown needs to be chosen. Unfortunately, in my case there are no insulating substrates available in the epi-ready (ready to be grown upon) form which are exactly lattice matched to graphene. Hence, I attempt to grow graphene on substrates with hexagonal symmetry which are not exactly lattice matched to graphene. The substrates I have explored in this dissertation are c-plane sapphire and C terminated 4H-SiC which have a hexagonal symmetry similar to graphene and have a decent lattice matching to graphene. The dynamics of the graphene growth process is very much dependent on the choice of the substrate and this forms the essence of this dissertation. The change in the character of graphene films grown when the substrate is switched from c-plane sapphire to 4H-SiC $(000\bar{1})$ is studied in greater detail. It is reported here that the graphene film grown on c-plane sapphire is so strained to the substrate that the film surface ruptures into hexagonal shaped facets whereas no such faceting of the surface happens in the growths on 4H-SiC $(000\bar{1})$. It will be shown with the help of Raman spectroscopy that the graphene films grown on c-plane sapphire are under tensile stress whereas the graphene grown on 4H-SiC $(000\bar{1})$ are under compressive stress. But, in both the cases, the graphene starts to grow in an epitaxial manner and progresses into a polycrystalline mode with increase of thickness. Both XPS and Raman studies confirm that the grown film is graphitic

in nature. Electrical transport studies performed on graphene grown on both c-plane sapphire and 4H-SiC $(000\bar{1})$ show that the temperature dependent sheet resistance follow a power law behavior at high temperatures. Whereas, the low temperature transport departs from the power law behavior and will be described to follow a generalized Variable Range Hopping (VRH) behavior. It will be shown that the low temperature transport in the graphene films grown on c-plane sapphire is an interplay of both 2D and 3D Mott VRH whereas Efros Shklovskii VRH plays a dominant role in case of graphene grown on 4H-SiC $(000\bar{1})$. All the growths are analyzed in the light of in-situ Reflection High Energy Electron Diffraction (RHEED), ex-situ X-Ray Photoelectron Spectroscopy (XPS), Atomic Force Microscopy (AFM), Raman Spectroscopy and Electrical Transport.

The coming pages of this dissertation deal with the graphene growth process on the two distinctly different class of hexagonal substrates. Chapter 2 sets up the background of graphene where the lattice structure and electronic properties of graphene is discussed in addition to the existing methods of graphene synthesis which are discussed in the light of their advantages and disadvantages. The basic motivation of growing graphene by MBE is discussed in Chapter 3 where the epitaxial growth techniques associated with the MBE growth is dealt with. The analytical methods employed to analyze the MBE grown films : AFM, XPS, Raman Spectroscopy and Electrical Transport are described in Chapter 4 from the perspective of analyzing a graphene film. Chapter 5 describes the MBE growth process of graphene films on c-plane sapphire and 4H-SiC $(000\bar{1})$ with the help of RHEED, estimation of the thickness of the grown films with the help of XPS and a description of the morphology of the grown films with the help of AFM. Chapter 6 presents the results of the Raman spectroscopy of the MBE grown graphene films on these two substrates. The electrical transport studies of the MBE grown graphene films on both c-plane sapphire and 4H-SiC $(000\bar{1})$ substrates are described in Chapter 7. And finally in Chapter 8, I conclude my thesis with a short survey of possible directions of future research.

CHAPTER 2

GRAPHENE AND ITS BACKGROUND

The unique structural and electronic properties of graphene arise mainly due to its lattice structure. This chapter introduces the detailed description of the band structure of graphene where it will be established why the charge carriers are chiral and Dirac-like with a brief touch-up on the concept of pseudospin. Since the graphene films described in this dissertation will be mostly more than single layer, a small description of the the band structure of the bilayer graphene becomes essential. The past methods of isolating and synthesizing graphene will be discussed at the end in the light of their advantages and disadvantages which would throw some light why the method of growing graphene by MBE becomes crucial.

2.1 Lattice structure and Electronic properties of graphene

This section introduces the lattice structure of graphene and its stacking sequence. The band structure of the single layer graphene will be formulated which shows the Dirac-like character of the charge carriers followed by the description of the bilayer case.

2.1.1 Graphene: structure and stacking sequence

Graphene is a single sheet of graphite which consists of identical graphene layers stacked up in a certain periodic sequence. Fig 2.1 shows the crystal lattice structure of graphene. The carbon atoms in a graphene layer are covalently bound through sp^2 hybridized σ bonds to form a hexagonal two-dimensional array. The

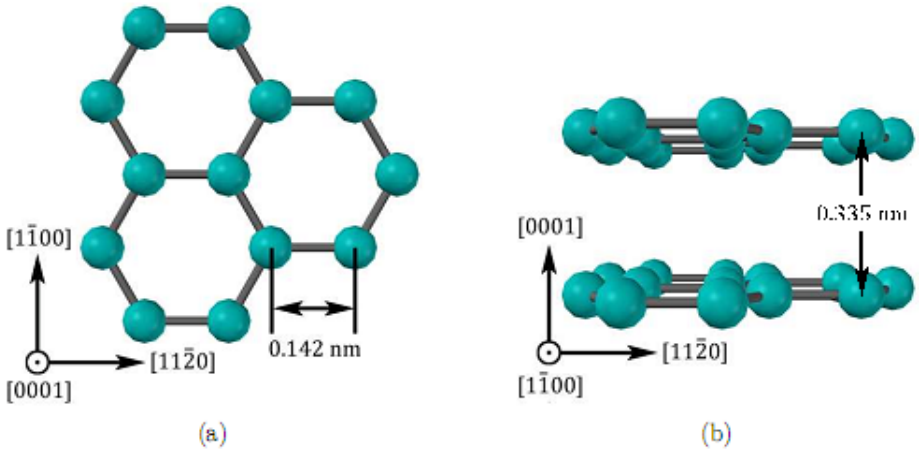

Figure 2.1: The crystal structure of graphite (a) top view of a single graphite sheet normal to the basal plane (b) parallel to the basal plane. Figure adapted from [1]

rigidity of the sigma bond is responsible for the robustness of the graphene lattice. The carbon-carbon bond distance is 1.42 Å making the lattice constant as 2.46 Å. The spacing between adjacent layers is 3.35 Å making the unit cell lattice constant in the c-direction as 6.7 Å.

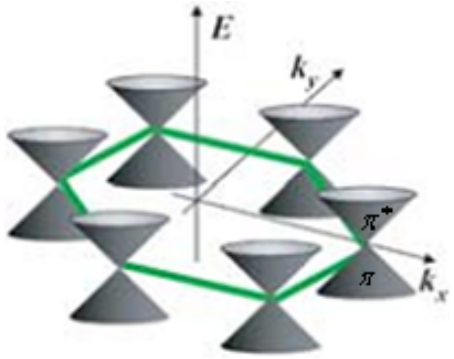

Figure 2.2: The lattice structure of graphene in k-space showing the bonding π and antibonding π^* orbitals which are the unhybrdized p_z orbitals responsible for the conductivity in graphene.

As shown in Fig 2.2, the unhybridized p_z orbitals form the bonding π and the antibonding π^* orbitals which are responsible for the conductivity in graphene. The Van der Walls force is responsible for the adhesion of adjacent graphene monolayers as a result of which the layers can be easily cleaved.

Graphene layers can be stacked in different sequences. The most commonly

occurring graphite are stacked in either Bernal (ABAB..) or Rhombohedral (ABCABC..) manner as shown in Fig 2.3. In a Bernal structure as shown in Fig

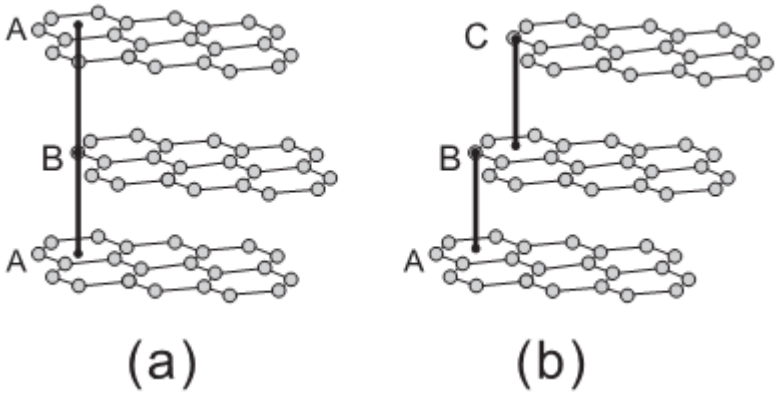

Figure 2.3: The stacking arrangement of graphite (a) Bernal (AB) (b) Rhombohedral (ABC). Figure adapted from [2]

2.3(a), the carbon atoms in the layer B are directly above the center of a carbon hexagon in the layer A. Whereas in a Rhombohedral structure as shown in Fig 2.3(b), the center of a carbon hexagon in the layer A is directly below a corner of a hexagon in the layer B, which in turn is directly below a nonequivalent corner of a hexagon in the layer C. Different stacking schemes result in subtle changes in the band structure of graphite.

As will be pointed out in the later chapters, the graphene films I grow by MBE on the insulating substrates will not have the well-ordered Bernal or Rhombohedral stacked graphene sheets. But, the graphene sheets will be stacked in a random sequence which will have interesting consequences to the Raman 2D bands as will be discussed in Chapters 6.

The following two sub-sections discuss in detail the lattice and electronic structure of single layer and bilayer graphene.

2.1.2 Single layer graphene

The basic graphene lattice is made up of two hexagonal carbon sublattices, labelled A (black spheres) and B (red spheres) forming a honeycomb pattern shown

in Fig 2.4(A).

The geometry of the lattice of the single layer graphene shown in Fig 2.4 is defined as follows:

The relevant vectors shown in Fig 2.4 are defined as :

$$\boldsymbol{a_1} = \frac{a}{2}\left(1, \sqrt{3}\right) \tag{2.1}$$

$$\boldsymbol{a_2} = \frac{a}{2}\left(-1, \sqrt{3}\right) \tag{2.2}$$

with $a = |\mathbf{a_1}| = |\mathbf{a_2}| = 2.46$ Å. Nearest neighbor carbon atoms are defined by vectors $\mathbf{R_j}$ with $j = 1, 2, 3$ with the distance between **A** and **B** atoms equal to 1.42 Å.

$$\boldsymbol{R_1} = \frac{a}{2}\left(1, \frac{\sqrt{3}}{3}\right) \tag{2.3}$$

$$\boldsymbol{R_2} = \frac{a}{2}\left(-1, \frac{\sqrt{3}}{3}\right) \tag{2.4}$$

$$\boldsymbol{R_3} = a\left(0, \frac{-\sqrt{3}}{3}\right) \tag{2.5}$$

The bonds between **A** and **B** carbon atoms have a strong interatomic coupling given by $\tau \sim -3.0eV$ [3] which is the reason for the strength and robustness of the in-plane sp^2 hybridized bonds. Since **A** and **B** atoms are identical, the graphene lattice has **sublattice symmetry**. The lattice structure in the reciprocal space shown in Fig 2.4(B) where vectors $\mathbf{b_1}$ and $\mathbf{b_2}$ are given as follows :

$$\boldsymbol{b_1} = \frac{2\pi}{a}\left(1, \frac{\sqrt{3}}{3}\right) \tag{2.6}$$

$$\boldsymbol{b_2} = \frac{2\pi}{a}\left(-1, \frac{\sqrt{3}}{3}\right) \tag{2.7}$$

Fig 2.4(B) also shows the first Brillouin Zone with the center labelled as Γ where $\mathbf{k} = 0$. The two inequivalent corners of the Brillouin Zone labelled as $\mathbf{K_i}$ where i

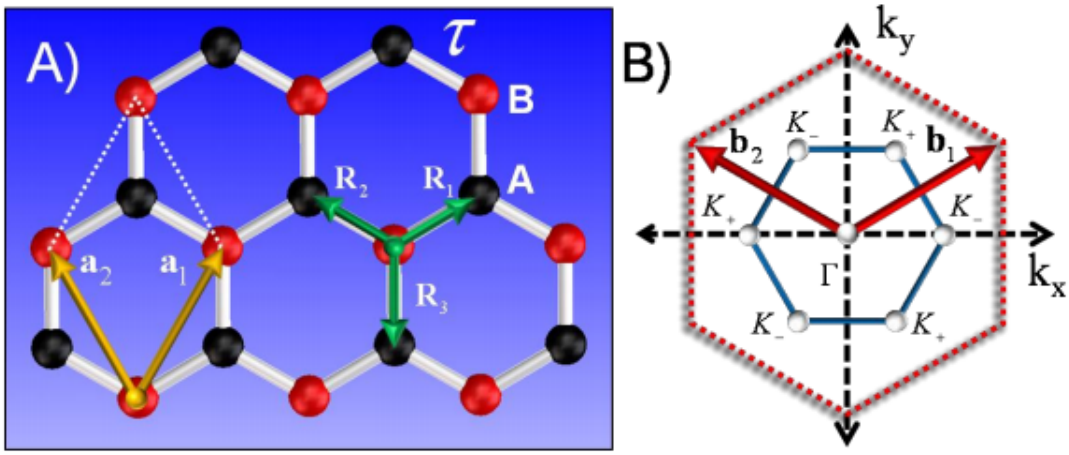

Figure 2.4: (A) Lattice structure of single layer graphene made up of two sublattices, **A** and **B**. The unit cell (white hexagon) is comprised of two hexagonal vectors, $\mathbf{a_1}$ and $\mathbf{a_2}$ with length 2.46 Å. Nearest neighbor atoms are defined by three translation vectors $\mathbf{R_j}$ with length 1.42 Å. (B) Reciprocal lattice of single layer graphene defined by $\mathbf{b_1}$ and $\mathbf{b_2}$. Blue hexagon outlines the first Brillouin zone of graphene with points of high symmetry labelled as $\mathbf{\Gamma}$, $\mathbf{K}_+$ and $\mathbf{K}_-$. Figure adapted from [3]

is + or - are defined as :

$$\boldsymbol{K}_+ = \frac{4\pi}{3a}(-1, 0) \tag{2.8}$$

$$\boldsymbol{K}_- = \frac{4\pi}{3a}(1, 0) \tag{2.9}$$

Electronic structure of single layer graphene

The electronic structure of graphene was first calculated by Wallace [36] using only the p_z orbitals contribution in order to simplify the complicated structure of graphite. The entire calculation here will be for an electronically isolated graphene sheet which is necessarily not the situation for epitaxial graphene on SiC where charge transfer due to the underlying substrate plays a major role. Lets start with the Schrodinger equation :

$$\boldsymbol{H\Psi} = E(\boldsymbol{k})\boldsymbol{\Psi} \tag{2.10}$$

where $\mathbf{\Psi}$ is a linear combination of Bloch functions $\mathbf{\Phi}$ given as :

$$\mathbf{\Phi} = \frac{1}{N}\sum_{R}^{N} e^{i\boldsymbol{k}.\boldsymbol{r}}\phi_j(\boldsymbol{r}-\boldsymbol{R}), (j = 1, ..., N) \tag{2.11}$$

where $\phi_j(\boldsymbol{r}-\boldsymbol{R})$ is the wavefunction, $\mathbf{R}$ is the atomic location, N is the number of unit cells, $\boldsymbol{k}$ is the momentum and $\boldsymbol{r}$ is the position . The eigen values E($\mathbf{k}$) are given by the secular equation :

$$det[\boldsymbol{H} - E(\boldsymbol{k})\boldsymbol{I}] = 0 \tag{2.12}$$

The Hamiltonian which is a Hermitian matrix is defined as :

$$\boldsymbol{H} = \begin{pmatrix} H_{AA} & H_{AB} \\ H_{BA} & H_{BB} \end{pmatrix} \tag{2.13}$$

where $H_{i,j} = \boldsymbol{\Psi_i H \Psi_j}$. H_{AA} and H_{BB} are the p_z orbital energy ϵ where $\epsilon = 0$ for reference. The off-diagonal term $H_{AB} = H^*_{BA} = \boldsymbol{\Psi_A H \Psi_B}$ is calculated using the Bloch wavefunctions Eq (2.11) [37] given as :

$$H_{AB} = \tau\left(e^{i\boldsymbol{k}.\boldsymbol{R_1}} + e^{i\boldsymbol{k}.\boldsymbol{R_2}} + e^{i\boldsymbol{k}.\boldsymbol{R_3}}\right) = \tau f(\boldsymbol{k}) \tag{2.14}$$

Plugging in the vectors $\boldsymbol{R_j}$ Eq (2.3, 2.4 and 2.5), $f(\boldsymbol{k})$ is given as :

$$f(\boldsymbol{k}) = e^{\frac{ik_y a}{\sqrt{3}}} + 2\cos\left(\frac{k_x a}{2}\right) e^{\frac{-ik_y a}{2\sqrt{3}}} \tag{2.15}$$

Now, Eq (2.13) becomes :

$$\boldsymbol{H} = \begin{pmatrix} 0 & \tau f(\boldsymbol{k}) \\ \tau f(\boldsymbol{k})^* & 0 \end{pmatrix} \tag{2.16}$$

Solving Eq (2.12) :

$$E(\boldsymbol{k}) = \pm\tau\sqrt{1 + 4\cos\left(\frac{\sqrt{3}k_y a}{2}\right)\cos\left(\frac{k_x a}{2}\right) + 4\cos^2\left(\frac{k_x a}{2}\right)} \tag{2.17}$$

where "+" and "-" denote the bonding and the anti-bonding states respectively. The band structure of graphene at low energies looks like a conical hourglass structure where the bonding and the anti-bonding cones meet at the charge neutrality point. This conical hourglass structure is repeated at each of the six corners of the hexagonal Brillouin zone which has the two inequivalent points $\boldsymbol{K}_+$ and $\boldsymbol{K}_-$ referred to as the valleys of graphene. This is shown in Fig 2.5

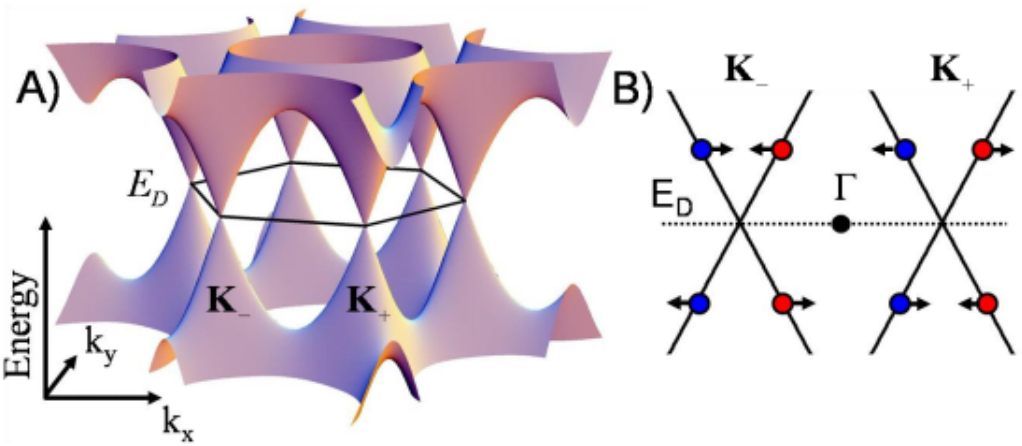

Figure 2.5: (A) Shows the conical nature of graphene's electronic bands close to the Dirac point; also shows the two inequivalent points $\boldsymbol{K}_+$ and $\boldsymbol{K}_-$. (B) The pseudospin (arrow) points either parallel or anti-parallel to the right moving (red circle) or left moving (blue circle) particles. The pseudospin depends on whether the particle is in the electron band (below E_D) or in the hole band (above E_D) and whether the particle is in the $\boldsymbol{K}_+$ or $\boldsymbol{K}_-$ valley. Figure adapted from [3]

Dirac Fermions

The thrust of interest in graphene started because some theorists claimed that this system is a perfect example where some aspects of high-energy physics can be studied in a condensed matter framework. Lets try to look for the Dirac physics which is embedded in the Hamiltonian described in Eq (2.16).

Expanding Eq (2.14) about one of the corners of the Brillouin zone ($\boldsymbol{K_+}$ and $\boldsymbol{K_-}$) by making the transformation $\mathbf{k} = \mathbf{K_+} + \boldsymbol{\kappa}$ where $\boldsymbol{\kappa}$ is small. From Fig 2.4A, we have $\mathbf{R_1} = \mathbf{R_3} + \mathbf{a_1}$, $\mathbf{R_2} = \mathbf{R_3} + \mathbf{a_2}$ and $\mathbf{R_3} = \mathbf{R_3}$. And we know that :

$$e^{i\boldsymbol{K_+}.\boldsymbol{a_1}} = e^{-i\frac{2\pi}{3}} \tag{2.18}$$

$$e^{i\boldsymbol{K_+}.\boldsymbol{a_2}} = e^{i\frac{2\pi}{3}} \tag{2.19}$$

$$e^{i\boldsymbol{K_+}.\boldsymbol{a_3}} = 1 \tag{2.20}$$

In this framework, Eq (2.14) can be simplified as :

$$H_{AB} = \tau e^{i\boldsymbol{\kappa}.\boldsymbol{R_3}} \left(1 + e^{-i\frac{2\pi}{3}} e^{i\boldsymbol{\kappa}.\boldsymbol{a_1}} + e^{i\frac{2\pi}{3}} e^{i\boldsymbol{\kappa}.\boldsymbol{a_2}}\right) \tag{2.21}$$

Using $e^x \sim 1 + x$, Eq (2.21) becomes :

$$H_{AB} \sim \tau \left(1 + i\boldsymbol{\kappa}.\boldsymbol{R_3}\right) \left(1 + e^{-i\frac{2\pi}{3}} \left(1 + i\boldsymbol{\kappa}.\boldsymbol{a_1}\right) + e^{i\frac{2\pi}{3}} \left(1 + i\boldsymbol{\kappa}.\boldsymbol{a_2}\right)\right) \tag{2.22}$$

Further simplifying and neglecting higher order terms, Eq (2.22) becomes :

$$H_{AB} \sim i\tau \left(e^{-i\frac{2\pi}{3}} \boldsymbol{\kappa}.\boldsymbol{a_1} + e^{i\frac{2\pi}{3}} \boldsymbol{\kappa}.\boldsymbol{a_2}\right) \tag{2.23}$$

By plugging in the values $\boldsymbol{a_1}$ and $\boldsymbol{a_2}$ from Eq (2.1) and Eq (2.2), Eq (2.23) becomes :

$$H_{AB} \sim \frac{\sqrt{3}\tau a}{2}(\kappa_x - i\kappa_y) \tag{2.24}$$

The Hamiltonian for a single layer graphene reduces to the Dirac form :

$$\boldsymbol{H} = \frac{\sqrt{3}\tau a}{2} \begin{pmatrix} 0 & \kappa_x - i\kappa_y \\ \kappa_x + i\kappa_y & 0 \end{pmatrix} \tag{2.25}$$

Involving the Pauli matrices in Eq (2.25), it can be written as a Dirac Hamiltonian:

$$\boldsymbol{H} = \hbar v_F(\kappa_x\sigma_x + \kappa_y\sigma_y) = \hbar v_F \boldsymbol{\kappa.\sigma} \tag{2.26}$$

where $v_F = \frac{\sqrt{3}\tau a}{2\hbar}$.

Eq (2.26) is the Dirac Hamiltonian described earlier with the speed of light replaced by $v_F \sim c/300 \sim 1\times10^6 m/s$. The mass of the carriers become irrelevant; hence the carriers in graphene are referred to as massless Dirac fermions.

Pseudospin

The projection of $\boldsymbol{\sigma}$ on the direction of motion $\boldsymbol{\kappa}$ in Eq (2.26) is known as chirality which can be either right-handed or left-handed. Dirac fermions in graphene have a similar sense of chirality called the pseudospin. Lets make the following transformation to Eq 2.25:

$$\kappa_x + i\kappa_y = \kappa e^{i\phi} \tag{2.27}$$

where $\tan(\phi) = \frac{\kappa_y}{\kappa_x}$. Now, Eq (2.25) becomes :

$$\boldsymbol{H} = \hbar v_F \begin{pmatrix} 0 & \kappa e^{-i\phi} \\ \kappa e^{i\phi} & 0 \end{pmatrix} \tag{2.28}$$

Solving for the eigen-energies :

$$E(k) = \pm\hbar v_F \kappa \tag{2.29}$$

Now, solving for the wavefunctions in the Bloch form after normalization yields :

$$\boldsymbol{\Psi}_{K_\pm} = \frac{1}{2A} e^{i\boldsymbol{\kappa.r}} \begin{pmatrix} s \\ e^{\pm i\phi} \end{pmatrix} \tag{2.30}$$

where $s = +1$ represents unfilled electron states, $s = -1$ represents filled electron states and A is the area of the system. The two component spinor associated

with the wavefunction is called the pseudospin. Fig 2.5B depicts the pseudospin component of the wavefunction where a vertical slice of the two Dirac cones is shown. In Fig 2.5B, right moving states are colored red and left moving states are colored blue. The chirality of electron states around $\boldsymbol{K}_+$ is right-handed where the pseudospin (arrow) is parallel to $\boldsymbol{\kappa}$. Likewise, the electron states around $\boldsymbol{K}_-$ are left-handed where the pseudospin is anti-parallel to $\boldsymbol{\kappa}$. For hole states, the sense of pseudospin is exactly opposite to that of the electrons. The pseudospin is responsible for the Berry's phase seen in graphene in an applied magnetic field [24]. The linear dispersion and the Berry's phase of π is responsible for the half-interger Quantum Hall Effect [24].

2.1.3 Bilayer graphene

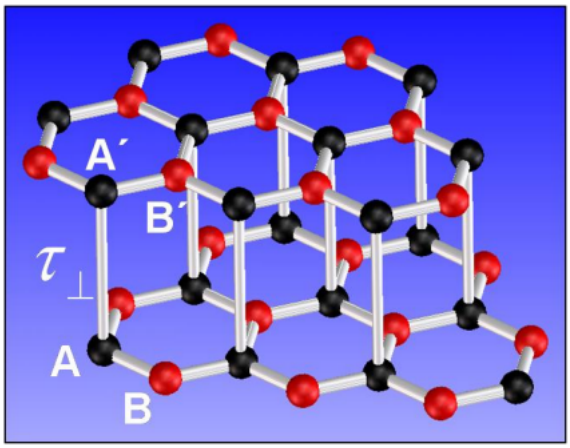

Figure 2.6: Lattice structure of Bernal stacked bilayer graphene. There is a weak interlayer coupling $\tau_\perp \sim 0.4eV$ in this configuration. Figure adapted from [3]

When a second graphene layer is added to a single layer graphene, the sublattice symmetry is broken resulting in variations of the electronic properties to that discussed in single layer case. Fig 2.6 shows a Bernal stacked bilayer graphene where the second plane of graphene is rotated 180 ° with respect to the first which aligns the $\boldsymbol{A}$ atoms of the bottom layer with the $\boldsymbol{A'}$ atoms of the top. The way the second graphene layer is stacked on top of the first layer, it induces a hybridization of the bonding orbitals of the $\boldsymbol{A}$ and $\boldsymbol{A'}$ atoms. This adds two more

energy bands (spin degenerate) in addition to the exisiting two low energy bands of the single-layer case.

Following the approach described in the PhD Thesis [3], the tight binding Hamiltonian is formulated by considering different electron coupling paths between the layers. An example of a coupling path can be $\boldsymbol{B} \rightarrow \boldsymbol{A} \rightarrow \boldsymbol{A}^{'} \rightarrow \boldsymbol{B}^{'}$ which goes directly through the bond between $\boldsymbol{A}$ and $\boldsymbol{A}^{'}$ atoms. The direct coupling $\boldsymbol{B} \rightarrow \boldsymbol{B}^{'}$ is neglected in this derivation. The aprroximate tight-binding Hamiltonian expanded around $\boldsymbol{K}_{\pm}$ is given as :

$$\boldsymbol{H} = \xi \begin{pmatrix} \frac{-\Delta}{2} & 0 & 0 & v_F\pi^* \\ 0 & \frac{\Delta}{2} & v_F\pi & 0 \\ 0 & v_F\pi^* & \frac{\Delta}{2} & \xi\tau_\perp \\ v_F\pi & 0 & \xi\tau_\perp & \frac{-\Delta}{2} \end{pmatrix} \tag{2.31}$$

where Δ is the induced asymmetry between the layers, v_F is the in-plane velocity, $\xi = \pm 1$ for $\boldsymbol{K}_{\pm}$, $\pi = \hbar(\kappa_x + i\kappa_y)$ and $\tau_\perp$ is the interlayer coupling strength. Solving the secular equation gives four energy bands for bilyaer graphene given as :

$$E_{\pm}^{\alpha}(k) = \pm \left(\frac{\tau_\perp^2}{2} + \frac{\Delta^2}{4} + (v\hbar\kappa)^2 + (-1)^{\alpha} \sqrt{\frac{\tau_\perp^4}{4} + (v\hbar\kappa)^2(\tau_\perp^2 + \Delta^2)} \right)^{1/2} \tag{2.32}$$

where $E_{\pm}^{\alpha}(k)$ where α is the band-index and $\pm$ for the unfilled and filled electron states respectively. Following Eq (2.32), the electronic structure of bilayer graphene is plotted in Fig (2.7). Fig (2.7A) shows the band structure of an isolated bilayer graphene ($\Delta = 0$). It can be seen that the bilayer bands are hyperbolic near the Fermi energy whereas the single-layer remains linear. The separation of the hyperbolic bands on either side of the Fermi energy is equal to the interlayer coupling strength ($\tau_\perp$). Fig (2.7B) shows the dispersion with asymmetry $\Delta = \tau_\perp$. This is generally observed in bilayer epitaxial graphene where charge transfer from the substrate underneath induces a potential difference between the layers. This makes bilayer graphene useful for potential device applications.

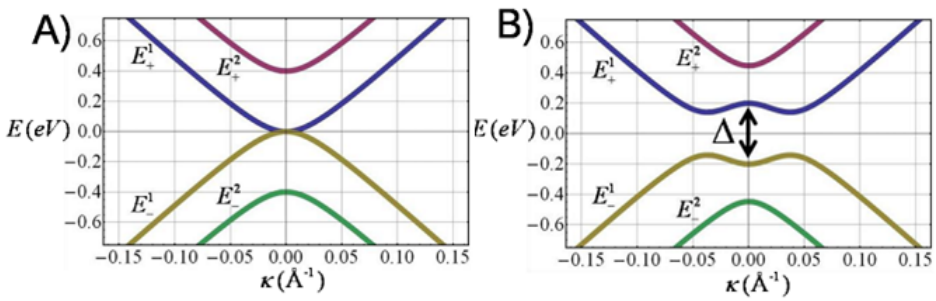

Figure 2.7: (A) Energy dispersion of Bernal stacked bilayer graphene with interlayer coupling $\tau_\perp \sim 0.4eV$. Bilayer bands are hyperbolic whereas the single layer bands are linear. (B) Energy dispersion of bilayer graphene when a potential difference $\Delta \sim 0.4eV$ is introduced. Figure adapted from [3]

2.2 Past methods to isolate and synthesize graphene

The first synthesis of graphene probably dates back to as early as 1962 when Boehm reported monolayer flakes of reduced graphene oxide [38] studied by transmission electron microscopy and X-ray diffraction. Around 1970s, graphene films were started to be grown by pyrolysis of hydrocarbon on heated Ni substrates [39]. The interest in epitaxial growth of graphene on metallic substrates was renewed 30 years later when Oshima and Nagashima tried growing epitaxial films of graphite on solid crystalline metallic surfaces [40]. The method to synthesize graphite by graphitization of SiC was first done by Badami [41] in 1962 almost 42 years before the Georgia Tech group led by Walt De Heer [42]. Hence, the study of graphene has been around for around 50 years now; but its interest came alive when the first paper by the Manchester group [43] was published in 2004. Geim and Novoselov used the famous "scotch tape" method to isolate graphene and then followed the plethora of ground breaking experiments. In this section the focus will be on the most prominent past techniques of graphene synthesis like mechanical exfoliation, chemical vapor deposition of graphene on metallic substrates and epitaxial growth of graphene by graphitization of SiC. These methods will be discussed in the light of their advantages and disadvantages.

2.2.1 Mechanical exfoliation

This method famously known as the "Scotch Tape" method was revolutionized by the Manchester group in 2004 [43]. Besides demonstrating high carrier mobility in the back-gated Hall bars, this also proved the existence and stability of two-dimensional films. The simplicity of the technique led to a research explosion and an entire new graphene community was created.

The process of mechanically exfoliating graphene occurs in a few steps. Step number one involves a piece of cellophane tape and placing its sticky side on the surface of a commercially available HOPG wafer. Step number two which needs some practice in peeling the cellophane tape from the HOPG wafer leaving small chunks of graphite stuck to it. A virgin section of a cellophane tape is used to further thin down the stuck-on pieces from the original HOPG wafer. This process is repeated until the small chunks are thinned down to only few flakes of graphite. Step number three requires the sticky side of the cellophane tape down onto a substrate, generally a 300nm thick SiO_2 on a degenerately doped Si substrate. One such successful isolation of a graphene flake is shown in Fig 2.8

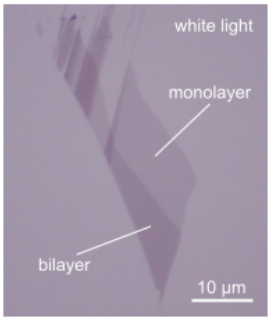

Figure 2.8: Optical image of an isolated graphene flake. Figure adapted from [4]

The thickness of the SiO_2 on Si is very important as this creates an optical contrast so that it can be seen under the optical microscope. Another thickness of SiO_2 close to 90 nm also creates a noticeable contrast in the visible range as displayed in Fig 2.9. Once the cellophane tape is stuck to the substrate, it is slightly rubbed in order to make sure that the first few layers of graphite is held to the substrate by Van der Walls forces; and then the tape is pulled off. It needs

some experience and a lot of luck to find a sample with a few random spots on the substrate with mono-layer to bi-layer graphene. Finally step number four is locating the needle in the haystack under the optical microscope. If one had a successful exfoliation, a single graphene flake sample of unknown size and geometry can be found. If the size and geometry is not appropriate for practical usage, it has to be discarded and a fresh sample needs to be made. Most importantly, without using the set oxide thickness this exfoliation technique would not have been successful at all since a single layer of graphene transmits almost 100 per cent of visible light used to locate the flakes.

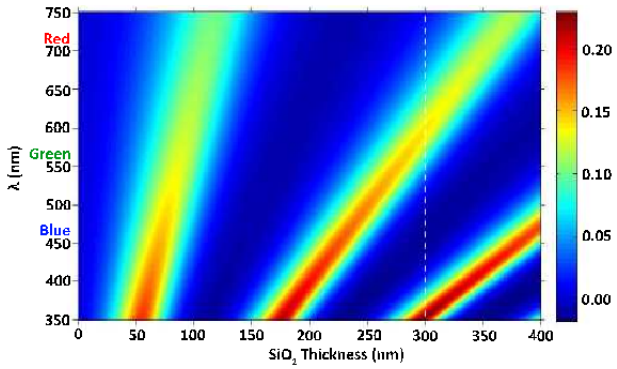

Figure 2.9: Map of the thin film interference enhanced optical contrast of a graphene flake on SiO_2 on Si system as a function of light wavelength, λ,and SiO_2 thickness. The most commonly used oxide thickness, 300 nm, is denoted with a thin dashed line which shows relatively strong contrast in the visible light range. Figure adapted from [1]

After a graphene flake is found, custom e-beam lithography masks have to be designed around the flake's geometry if devices are to be fabricated on it. Although this method is painstaking and time consuming, the irony is that the exfoliated graphene from a naturally available HOPG wafer still has the highest quality available so far. But, because of this probabilistic approach of getting a good graphene sample, it is far from having a commercial appeal in the near future.

2.2.2 Chemical Vapor Deposition of graphene on metallic substrates

After the success of mechanical exfoliation of graphene, the search for a method of getting a macro scale graphene sample continued. This renewed the interest in Chemical Vapor Deposition (CVD) of graphene on metallic substrates like Ni [44, 45], Cu [46], Pt [47, 48], Ir [49] and Ru [50] which are closely lattice matched to graphene.

The principle of the CVD process is straightforward. Hydrocarbon precursors like methane, ethylene or propane flows into the chamber containing the metallic substrate at elevated temperatures typically around 1000°C. The metal surface serves as a catalyst for the pyrolysis of the gaseous hydrocarbon and the C atoms remain on the surface of the metallic substrate whereas the H atoms desorb into the vapor stream. The C atoms then crystallize on the closely lattice matched substrate into a graphene lattice.

The CVD process can be of two kinds :

Surface Segregation

Some metals like Ni readily absorb the C atoms at elevated temperatures. Upon cooling, some of the C atoms segregate to the surface of the metal substrate and form sp^2 bonds to form graphene. This process of graphene formation is called surface segregation. But, the major drawback is that the cooling rate is really crucial which governs the formation of graphene. Fig 2.10 shows how different cooling rates lead to different segregation behaviors [45]. Extremely fast cooling rate results in a quench effect in which the C atoms lose their mobility before they can diffuse. With a medium cooling rate, a finite amount of C atoms can segregate at the surface which is the desired situation. The extremely slow cooling rate allows C atoms enough time to diffuse into the bulk, so there will not be enough C atoms segregating at the surface.

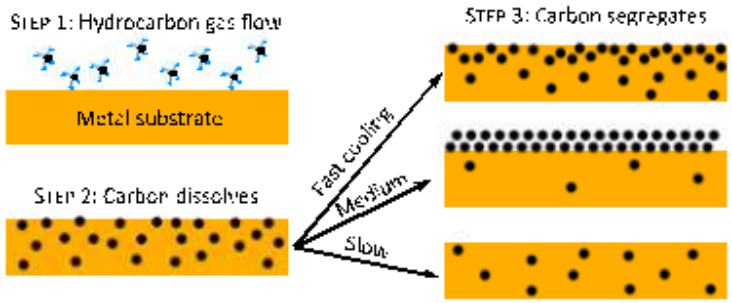

Figure 2.10: The three steps of the surface segregation growth technique is shown.First, a hydrocarbon gas flows over and cracks on a metal substrate. Second, the C atoms are dissolved into the metal. Third, the C segregates to the surface as the metal substrate is cooled. The cooling rate is critical to the success of graphene formation. Figure adapted from [1]

Surface Deposition

Some metals like Cu are not a great solvent for C. Hydrocarbon gases get pyrolyzed on the surface in a similar fashion as in the surface segregation method. However the C atoms do not dissolve into the bulk of the substrate, but remain on the surface of the metal to form graphene instead. That is the reason this process is called surface deposition method. Usage of Cu substrates for graphene growth is gaining popularity as the dependence on the rate of cooling is bypassed and the growth conditions become the sole important step.

Thus, graphene CVD on a metallic substrate has its own advantages. Firstly, the area of graphene is limited to the size of the metallic substrate (or foil). Recently, a roll-to-roll process [46] has been used to create rectangular graphene films that are over 0.75 m on the diagonal and could easily scale up to bigger sheets. Secondly, the metallic substrates are cheap which makes this method cost effective. But, the major issue is to transfer the grown graphene to an insulating substrate so that it can be put to device applications. This involves coating the graphene with a polymer like PMMA or PET and then wet-etching the metal leaving the graphene on the surface of the polymer. The graphene is then laid on top of an insulating substrate and the polymer is dissolved away. The involvement of wet-etching of the metal unintentionally doses the graphene which still remains the biggest disadvantage of this synthesis.

2.2.3 Epitaxial graphene formed due to thermal decomposition of SiC

As discussed earlier in this section, synthesis of graphene through graphitization of SiC has been around for more than forty years now. But, the interest in this technique was renewed in 2004 to circumvent the problem of synthesizing a wafer-size graphene sample on an insulator so that it can be put to device applications on a bigger scale. The Georgia Tech group led by Walt de Heer led the resurgence of using the SiC substrates as a practical method to form epitaxial graphene [42].

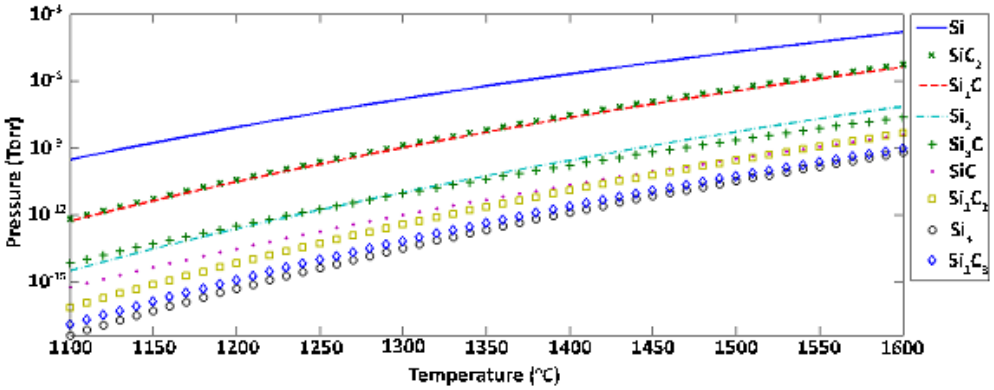

Figure 2.11: Partial pessure of sublimating species from a SiC substrate as a function of temperature. Figure adapted from [5]

The working principle of graphitization is quite simple. At elevated temperatues much below the melting point of SiC (approx 3100 K), it starts to sublimate and this preferential desorption of gaseous species is exploited in the formation of graphene on the surface. Looking at the partial pressure data of the sublimating species from SiC shown in Fig 2.11, the most common sublimating species is Si. Its partial pressure is nearly two orders of magnitude greater than the next two prevalent species, Si_2C and SiC_2 which have similar partial pressures. Adding the constituent atoms together of these two molecules, it gives an equal ratio of Si atoms to C atoms sublimating from the surface. Therefore, this mutual desorption does not alter the stoichiometry of the surface. The fourth most common gaseous species is Si_2 which has a vapor pressure almost two orders of magnitude below Si. Hence, taking all these four common sublimating species into account, there

is a disproportionate release of Si that leaves behind C atoms at the surface. These C atoms will rearrange themselves in order to minimize the free energy and preferentially form sp^2 bonds indicative of graphitic materials. The governing reaction that controls this process is as follows :

$$SiC(s) \rightarrow Si(g) + C(graphite) \tag{2.33}$$

The above reaction does not take into account the coefficient of thermal expansion (CTE), β mismatch of graphite and SiC as shown in Fig 2.12.

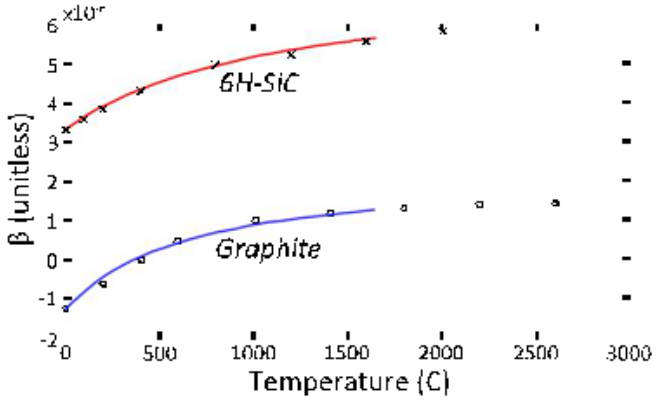

Figure 2.12: Temperature dependence of coefficients of thermal expansion, β taken for 6H-SiC and graphite taken from Refs [6] and [7] respectively.

Looking at Fig 2.12, β for graphite is negative below 400°C which means graphite will expand as it is cooled. β for SiC is larger than that of graphite in the entire temperature range of interest. This means that SiC substrate will shrink more than the graphene overlayer upon cooling. The SiC substrate will apply a compressive stress on the epitaxial graphene as it is cooled. Further below 400°C, although the epitaxial graphene expands, its not enough to offset the compression of the SiC substrate. This excessive compressive stress causes buckling and sometimes ruptures in the graphene film. And the evidence of the compressive stress is also seen in the Raman Spectroscopy data of the MBE grown films on 4H SiC $(000\bar{1})$ as will be discussed in Chapter 6.

One of the issues of the growth of graphene on SiC is the relatice lattice mis-

match. Graphene has a lattice constant of 0.246 nm while α-SiC (0001) has 0.308 nm. The misfit between the two is evaluated using the formula :

$$\epsilon_0 = 2\frac{a_f - a_s}{a_f + a_s} \tag{2.34}$$

where ϵ_0 is the misfit, a_s is the unstrained substrate lattice parameter and a_f is the unstrained film lattice parameter. For this particular system, the misfit is at 22 %. ϵ_0 being negative implies that the initial layers of graphene will be stretched in tension and the underlying substrate will be under compression. This further implies that the graphene lattice would have to stretch its bonds by this extra 22 % in order to fit the underlying substrate. This high levels of strain in the graphene film would create defects. If the compressive stress applied due to the CTE mismatch between graphene and SiC could balance the tensile stress due to lattice mismatch, this problem could have been solved. But, this is not to be.

The formation of graphene on the two faces of hexagonal SiC is described very briefly here :

Epitaxial Graphene on SiC(0001)

The Si face graphitizes in a relatively slow and in a self-limited fashion. The progression towards a completely graphitized surface follows as :

$$(1\times 1)_{SiC} \rightarrow (\sqrt{3}\times\sqrt{3})_{SiC} \rightarrow (6\sqrt{3}\times 6\sqrt{3})R30^{\circ}_{SiC} + (1\times 1)_g \rightarrow (1\times 1)_g \tag{2.35}$$

The first signs of the $(1\times 1)_g$ occur at around 1250 °C under ultra-high vacuum conditions. The progression through the SiC reconstructions to the first signs of graphene formation seems straightforward. The first reconstruction deals with the $(6\sqrt{3}\times 6\sqrt{3})R30^{\circ}$ which is C-rich with bond lengths between the C-C atoms identical to that of graphene. The crystallography is even the same as that of graphene. However, there is a lack of the graphitic π bonds; instead this first layer of C atoms is covalently bonded to the underlying SiC substrate. This makes the $(6\sqrt{3}\times 6\sqrt{3})R30^{\circ}$ reconstructed surface semi-conducting even though it has

the exact same structure as that of graphene. This layer serves as a transition between from bulk SiC to a graphene surface and is also an electrically isolating buffer between the SiC and the first layer of graphene. Hence, this is called the "buffer" layer.

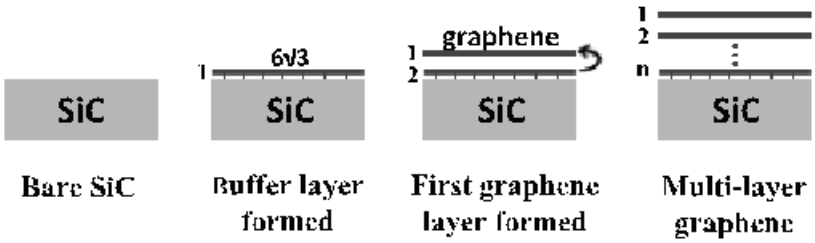

Figure 2.13: Graphene formation on the Si face begins with the formation of a buffer layer. The initial buffer layer becomes the first graphene layer once another buffer layer has formed under the previous one. Figure adapted from [1]

After the topmost $(6\sqrt{3}\times 6\sqrt{3})R30^\circ$ reconstructed layer is formed, another layer begins to form underneath it. This newly formed "buffer" layer will break the covalent bonds of the topmost layer to that of the underlying substrate, turning it into the first layer of graphene. In this manner, the first buffer layer to form becomes the topmost graphene layer as further buffer layers form below it as shown in Fig 2.13. It has been found by STM analysis [3] that the topmost layers have an **AB** or Bernal stacking structure. The unique graphene properties are lost when multiple layers of graphene form on the Si-face.

Epitaxial Graphene on SiC$(000\bar{1})$

The C face of SiC is known to graphitize much faster than the Si face and the graphitization starts as low as 1100 °C. Under identical conditions, the C-face will continue to grow unrestricted but the Si-face will not. The progression towards a completely graphitized surface follows through the following set of reconstructions:

$$(1\times 1)_{SiC} \rightarrow (3\times 3)_{SiC} \rightarrow (2\times 2)_{SiC} \rightarrow (1\times 1)_g \tag{2.36}$$

The C-face does not progress through a "buffer layer" as was the case with the Si-face. It can be seen in Eq 2.36, that there is no concurrently occupied surface

between the SiC and graphene. LEED studies [51] have proved that the C-face exhibits small domains with more rotational disorder about the (0001) direction which could be because the first layer is not covalently bonded to the underlying substrate. Hence, each nucleated domain finds its own rotation angle that minimizes its misfit strain.

Each individual graphene layer that forms is free to rotate relative to the others taking up any of the three energy minimizing rotations corresponding to the three-fold symmetry of the hexagonal crystal structure. This randomly stacked graphene layers is sometimes referred as "turbostatic" graphite. Raman spectroscopy [52] confirms that the 2D peak of a thermally decomposed C-face SiC can be fit to a single lorentzian with relatively small FWHM regardless of the number of graphene layers in contrast to what has been observed for the mechanically exfoliated graphene. It is reasoned that the individual graphene layers are electrically decoupled due to their random stacking order. A very similar nature of the 2D peak is seen in our MBE grown graphene on c-sapphire and 4H SiC $(000\bar{1})$)

Graphene synthesis on the C-face does not always form a uniform film. A better way to control the C-face thermal decomposition is needed. The most promising work towards this end is through exploring different growth environments and pressure [53].

Thus, we learn that synthesis of graphene on SiC by thermal decomposition depends on the graphitization temperature and the amount of time it is annealed. Getting a uniform monolayer coverage of graphene on a SiC substrate becomes difficult as significant Si sublimation starts at temperatures around 1000 °C which signals slow rate of graphitization. A lot of attention needs to be paid on the rate of increase of the substrate temperature and the amount of annealing time in order to get a uniform monolayer coverage which is always not easy.

CHAPTER 3

EPITAXIAL GROWTH OF GRAPHENE BY MOLECULAR BEAM EPITAXY (MBE)

In the previous chapter, the prominent techniques of graphene synthesis were discussed in the light of their advantages and disadvantages. This necessitates for the introduction of a new technique which will have the potential to address some of the problems in the existing graphene synthesis techniques. In this chapter, the basic motivation of this dissertation of growing graphene by MBE will be described followed by a very short literature survey of the past attempts to grow graphene by MBE. Any MBE growth requires the proper choice of substrates which should be lattice matched and should have a similar symmetry with the film being grown. This issue will be addressed next in the light of the lattice structure of graphene and the substrates explored (c-plane sapphire and 4H-SiC $(000\bar{1})$ in this dissertation). The last section of the chapter is dedicated for the epitaxial growth technique where the MBE growth chamber will be described followed by a description of the way the substrates are prepared and a detailed description of RHEED, the in-situ diagnostic tool used in the growth process.

3.1 Motivation of growing graphene by MBE

Mechanical exfoliation of graphite that requires a scotch tape and flakes of graphite helped the wide spread of graphene research. The excellent epitaxy of graphene with metallic substrates make the CVD approach an attractive candidate to grow graphene upon. Cu substrates and foils are predominantly in use to grow graphene upon since the growth is self-limited given the minimum solubility of C in Cu. But, the major drawback is that the metallic backlayer has to be etched and the

grown graphene film has to be transferred to insulating substrates to be put into device applications. Thus, in order to make the production of graphene commercially viable, it is imperative to synthesize high quality, large scale graphene films reproducibly and reliably directly on the surface of an insulator. We need a growth method which might be more easily integrated into a conventional device processing flow.

The present and very well researched method of synthesizing graphene by graphitization of SiC is directed towards achieving macro-scale graphene films for large scale device applications. But, this method relies on the rate of sublimation of Si from the hot substrate which is responsible for rearranging the remaining C atoms into a graphene lattice. It requires very precise control over growth parameters like substrate temperature, growth rate and chamber pressure. In the process of graphitization of SiC, these growth parameters are not actually independent of each other. In fact, the growth rate of graphene and the substrate temperature are very intimately linked to each other since the source of graphene is the substrate itself. It has been seen that varying the chamber pressure also results in variation of the Si sublimation rate and hence the graphene growth rate. This is the reason why some researchers have better control over the growth parameters when they carry out the decomposition of SiC in an induction furnace [54] compared to a UHV environment. It becomes really difficult to achieve uniform coverage of graphene over the wafer which requires immense control over all the inter-dependent growth parameters.

Hence, we need a true epitaxial growth process which would have huge benefits over simple decomposition. The epitaxial growth process should be able to perform direct deposition of carbon on an insulating substrate of interest which can eliminate the complex procedure of transferring the graphene to an insulating platform. The independent control over the substrate temperature and the atomic layer control over the thickness and composition should be achievable. Molecular Beam Epitaxy is a perfect candidate which has all these controls integrated in a single growth process. The MBE growth technique has been in use for a long

time in synthesizing semiconductor heterostructures; but only recently it has been used to grow graphene on an insulating substrate. The usage of this technique is definitely a promising first step towards circumventing the existing problems in graphene growth and making it more commercially viable.

With the success of growing graphene by MBE on an insulator where we can achieve sub-monolayer accuracy, it would accelerate the integration of graphene with other materials such as semiconductors, superconductors, ferromagnets and ferroelectrics in-situ in a very clean UHV environment. As a result, new functional devices based on these hybrid multilayers can be fabricated. Performing a growth in MBE environment, with so many other sources at our disposal, highly controlled doping of graphene can be achieved. With improved process control by varying the carbon flux on the substrate, innovative graphene based heterostructures such as BiSFET devices [55] which involves two graphene layers separated by a thin dielectric can be fabricated. Very clean graphene based Josephson Junctions can be fabricated where a very clean interface between graphene and the supercondutor can be achieved if one can perform the growth of graphene and the superconductor all in-situ in the MBE environment. With the usage of MBE technology in graphene, other heterostructures involving graphene can be designed which can better exploit the band-gap tunability of bilayer graphene [56] for opto-electronic applications.

With the prospect of such great applications of graphene based heterosctructures, MBE is the only possible way which can make this happen. Hence, more detailed study of the prospect of growing graphene on an insulator by MBE is required which is the essence of this dissertation.

3.2 A short literature survey of graphene growth by MBE

Although the growth of graphene by graphitization of SiC is well researched and is still being developed further, it has its own limitations as highlighted in the previous section. Usage of Molecular Beam Epitxay to grow graphene on an in-

sulator is a very recent effort in order to try to solve some of the problems like uniformity of coverage and thickness of graphene layers all over the wafer. This is a good first step towards the goal of synthesizing layer by layer growth of uniform graphene films in conjugation with oxide dielectrics directly on top of an insulator. MBE technique has been used for a long time to synthesize semiconductor heterostructures and this technique can certainly be used to develop better graphene based FETs where all the involved layers can be grown in-situ in a layer by layer fashion in clean MBE environment.

In this section, I will highlight the past studies on growing graphene by MBE. Although this technique is a well known process in the semiconductor growth, it has just been a couple of years where it has been used to grow graphene on an insulator. The insulating substrates researchers have considered range from Silicon Carbide (SiC) [9, 57, 8, 58], Si (111) [59, 60, 61], mica [62] and sapphire [10]. They have used both solid state [10, 59, 9, 57, 8, 60, 62] and gas source [58, 61] MBE to grow graphene.

Solid state MBE approach by sublimating very high purity graphite crystals [10, 59, 9, 8, 60, 62] or by heating a graphite filament [57] have shown to have a higher growth rate than the gas source MBE approach. The gas source MBE is mostly done by cracking of high purity ethanol [58, 61]. But, it is the growth temperature and proper choice of substrates that matter the most in growing highly crystalline graphene films where satisfying epitaxy with the substrate plays a crucial role.

Moreau et al [8] have shown that graphene can be grown by MBE on both C and Si terminated SiC substrates as shown in Fig 3.1. The AFM images show the grown film mimics the underlying substrate before the start of the growth. They perform the growth using sublimation of carbon from a heated graphite filament on n-type 6H-SiC wafers at $\sim$ 1030 °C. The substrate temperature is kept well below the graphitization temperature so as to prevent intrusive graphitization due to the sublimation of Si. But, the authors do not provide any sufficient evidence that intrusive graphitization of SiC does not happen. This will be addressed in

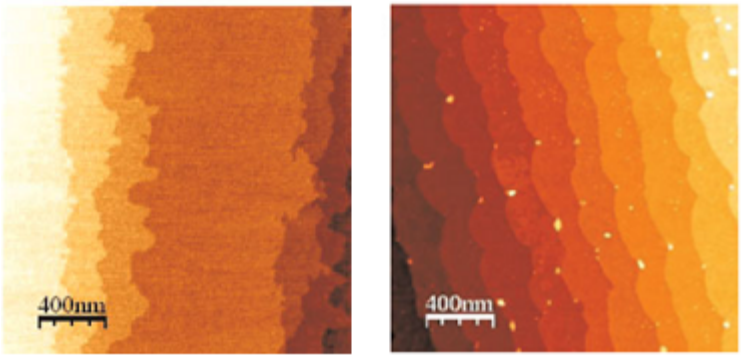

Figure 3.1: AFM images: Left: 2.1 ML graphene epitaxially grown on SiC $(000\bar{1})$ Right: 1.5 ML graphene epitaxially grown on SiC (0001). Courtesy: [8]

greater detail when our growth of graphene on 4H-SiC $(000\bar{1})$ will be discussed in Chapter 5.

Fig 3.2 shows another work of Moreau et al [9] where the growth is done on just C terminated n-type 6H-SiC substrates. The AFM image shows that MBE growth on a C terminated surface of SiC results in a smoother film than that of graphene film synthesized by graphitization of the substrate.

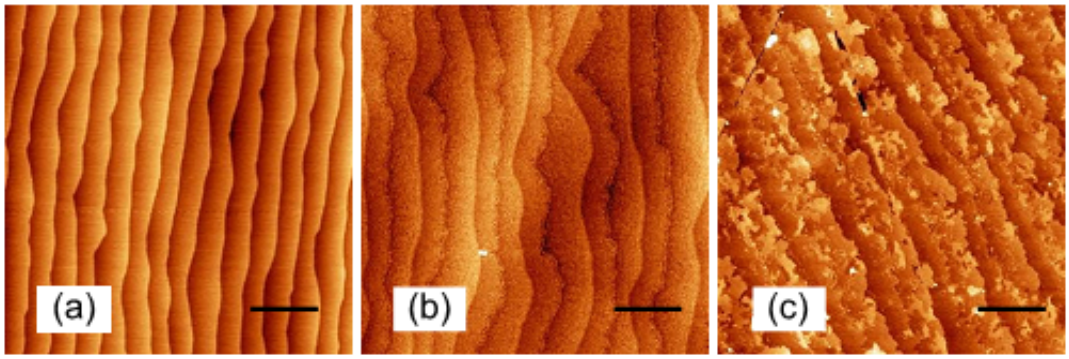

Figure 3.2: AFM topographic pictures of graphene grown on 6H-SiC $(000\bar{1})$ (a) After initial surface preparation (b) After MBE growth for 60 mins at 1040 °C (c) After graphitization for 10 mins at 1140 °C. Vertical scale: 2nm; Scale bar = $2\mu m$. Courtesy [9]

But, none of the authors above study in detail the growth dynamics and transport properties of the MBE grown graphene films which are highly dependent on the type of substrate used. In this dissertation, my focus would be to look at the MBE growth of graphene on two types of substrates with hexagonal symmetry:

C terminated SiC and c-plane sapphire. The consequence of lattice mismatch on the growth of epitaxial graphene and how it affects the electrical transport and the Raman spectroscopy have never been studied before. This would become the heart of this dissertation which I would describe in detail in Chapters 5, 6 and 7.

3.3 Issue of epitaxy of graphene with the substrates explored

In order to grow wafer-size graphene films on an insulator by MBE, one has to decide on the substrates which are decently lattice matched to graphene. But, unfortunately no insulating substrates which are available epi-ready (a flat terraced surface on which an epitaxial growth can take place) are exactly lattice matched to graphene except for the metallic substrates like Cu (111), Ni (111) etc which are known to be lattice matched to graphene. The only insulating substrate which is very closely lattice matched to graphene is Pyrolytic Boron Nitride (PBN); but unfortunately it is not available in the epi-ready form on which an MBE growth can be performed.

Here I will discuss two substrates, c-plane sapphire and C terminated SiC (4H-SiC $(000\bar{1})$) which have been used for the MBE growth of graphene in this dissertation. A discussion on the lattice structure of these substrates will be presented which will form the basis as to how the epitaxy with graphene can be satisfied even though the lattice mismatch persists.

3.3.1 C-plane sapphire

C-plane sapphire has been chosen because of its hexagonal symmetry and because of its high melting point($\sim 2000°C$) as the growth of graphene is supposed to be a high temperature process. This substrate is well used in the MBE growth processes and is available in the epi-ready form to be used for our growths. Fig 3.3 shows the different planes of a sapphire substrate and highlights the fact that

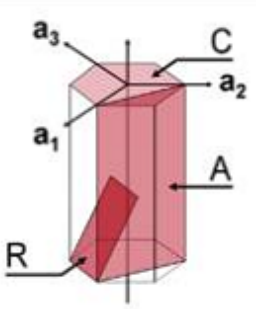

Figure 3.3: The figure shows C, R and A planes of the sapphire substrate

the c-plane has the hexagonal symmetry which would favor the growth of another hexagonal material : graphene.

Fig 3.4 highlights the lattice mismatch between graphene and the sapphire substrate. The in-plane C-C bond length in the hexagonal graphene lattice is 1.42 Å which makes the lattice constant of graphene as 2.46 Å. Whereas, in c-plane sapphire, the Al-Al bond length is 5.49 Å and the O-O bond length is 4.75 Å. The lattice constant of c-sapphire is reported as 4.75 Å[13]. So, it can be seen

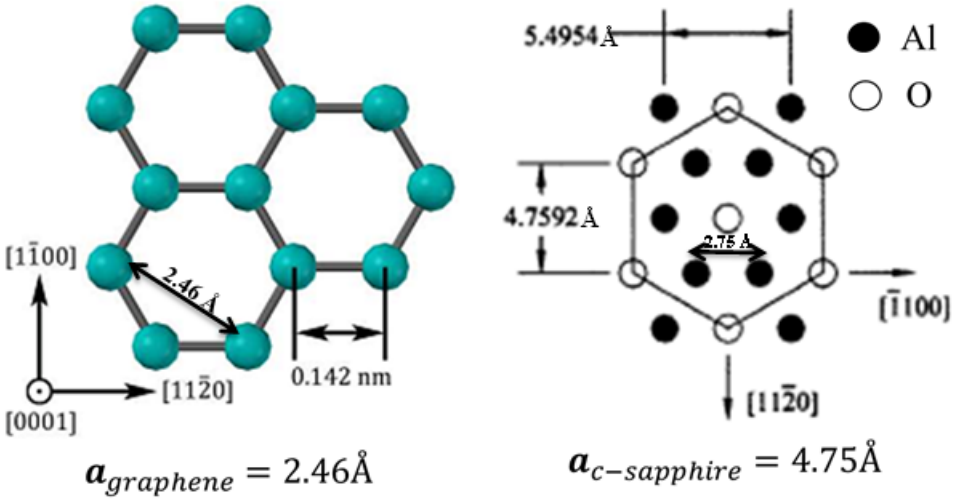

Figure 3.4: The figure shows the lattice constants of graphene and c-sapphire showing the important bond lengths. Left: shows the in-plane bonding structure of graphene. Right: shows the in-plane bonding structure of c-sapphire

that the lattice constant of c-plane sapphire is about twice the graphene lattice constant. But, the way the C atoms of the graphene lattice are aligned on the c-sapphire lattice is non-trivial. The relevant length on the c-sapphire lattice which

is close to the lattice constant of graphene is the length between the Al atoms in the inner hexagon given as 2.75 Å is shown in Fig 3.4. The graphene lattice would prefer to align itself on the inner hexagon of Al atoms shown in Fig 3.4 giving a mismatch $\sim$ 12 %. But, according to the calculations made by the authors of [10], the binding of carbon to oxygen atom on sapphire is more favorable in energy by 2.78 eV than that to Aluminium atom. Keeping this in mind, an alignment scheme of graphene on the c-sapphire lattice will be proposed in Chapter 5 when the graphene growth would be analyzed using RHEED which explains the growth mechanism.

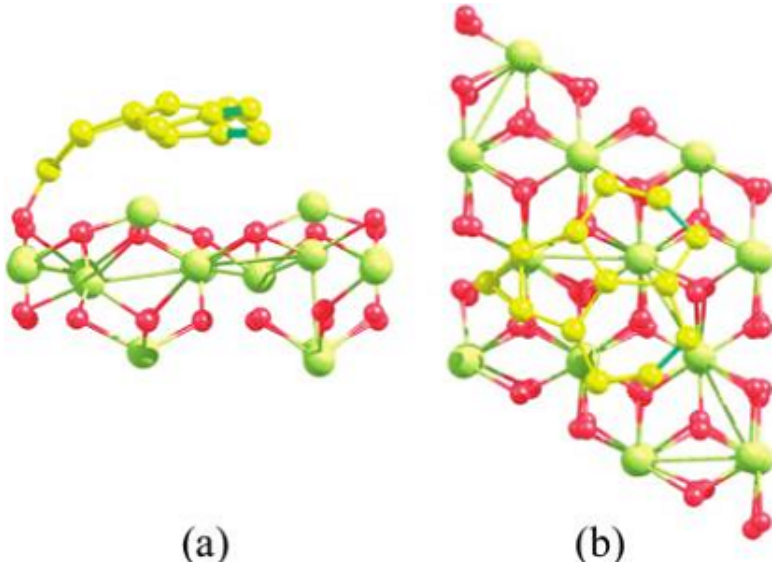

Figure 3.5: Optimized configuration of 13 carbon atoms adsorbed on c-plane sapphire. One carbon atom of a distorted graphene-like structure (yellow) binds to an oxygen atom (red), rather than to aluminium (green): (a) side view and (b) top view. Figure adapted from [10]

With the help of 13 carbon atoms adsorbed on c-plane sapphire, the authors of [10] show that the lowest energy configuration possible is as shown in Fig 3.5. The adsorption behavior of the lowest energy configuration shows the following : (i)the carbon atoms form a distorted honeycomb-like structure and (ii) one carbon atom of the entire carbon structure binds to atleast one oxygen atom of sapphire due to strong binding of carbon with oxygen atoms. Hence, they show that the sapphire surface unless covered by a perfect graphene sheet binds with carbon

structures by strong interaction between carbon and oxygen atoms. This leads to a segregation of the graphene lattice to a limited area rather than a perfect graphene formation which results in short correlation length studied with the help of Raman spectroscopy in Chapter 6.

In spite of the lattice mismatch, the growth of graphene starts in an epitaxial manner with macro-sized flat domains which will be discussed in Chapter 5. It will be shown that although the initial few MLs of graphene on c-plane sapphire are strained to the substrate, the strain relaxes with the progression of growth studied with the help of RHEED. The AFM images of the graphene grown on c-plane sapphire would show hexagonal faceting of the surface which are the dislocations associated with the relaxation of the graphene lattice with the progression of the growth.

3.3.2 Carbon terminated SiC(4H-SiC $(000\bar{1})$)

Graphitization of Silicon Carbide (SiC) has been well known since 1960s, but the focus of this dissertation is to use SiC as a substrate for graphene growth. So, we choose a growth temperature much lower than the graphitization temperature of the substrate so that we can be assured that the deposited carbon atoms by Molecular Beam Epitaxy is responsible for graphene growth rather than the graphitization of the substrate itself.

SiC is an indirect wide band gap semiconductor available in as many as 170 polytypes. Like c-plane sapphire, SiC is also a very high temperature material with a melting point at $\sim 2700°C$. The focus of the researchers has always been on the polytypes 4H- and 6H-SiC which are widely used to synthesize graphene by the graphitization of the substrate. This is because graphene itself being hexagonal is decently lattice matched with these two hexagonal polytypes. Lets look at the bonding structure of SiC more closely and look at the polytypes 4H and 6H SiC.

As shown in the inset of Fig 3.6, the element unit of SiC crystal structure is a covalently bonded tetrahedron with 4-fold symmetry. The distances between Si-C

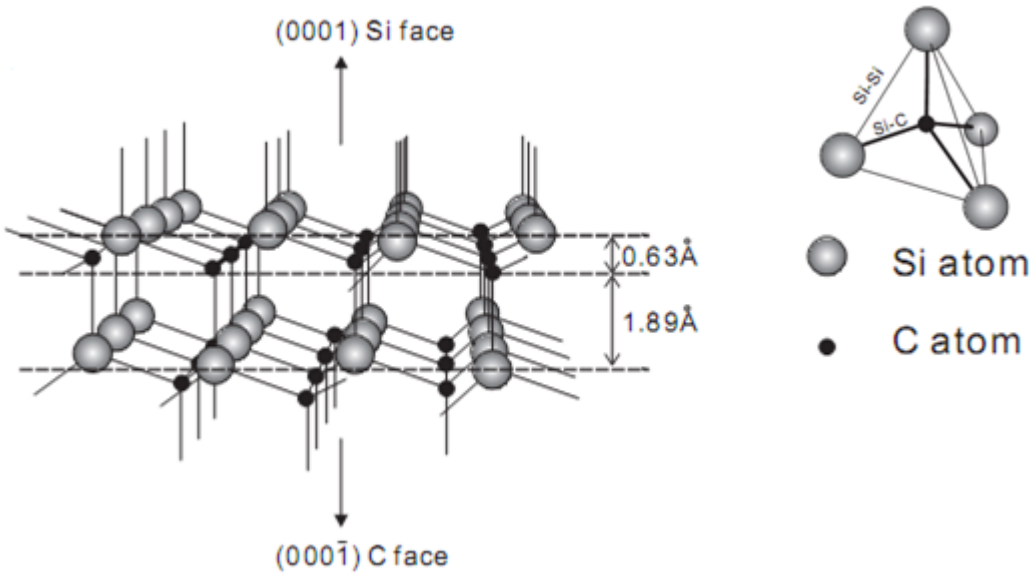

Figure 3.6: Crystal structure of SiC with Si-C bilayers along the C-axis. The inset shows the tetrahedral structure of the Si and C atoms in SiC. Figure adapted from [11]

bonds and Si-Si bonds are 1.89 Å and 3.08 Å respectively. With the c-axis being defined to be along one of the Si-C bonds, the crystal can be pictured as being composed of Si-C bilayers along the c-axis. As shown in Fig 3.6, a single Si-C bilayer is composed of a planar sheet of Si atoms coupled with a planar sheet of C atoms . The distance between two adjacent Si-C bilayers is $\sim$ 2.5 Å. Hence, cutting the SiC crystal perpendicular to the c-axis results in two polar faces: Si terminated face called as (0001) or Si-face and the C terminated face called as (000$\bar{1}$) or C-face.

Let us look at the two important polytypes : 4H and 6H SiC. In this number-letter notation, the number describes the number of layers in a complete unit cell along the c-axis and the letter describes the Bravais lattice type (Hexagonal (H), Cubic (C) or Rhombohedral (R)). Lets look at the 4H and 6H SiC, the hexagonal polytypes which are generally the focus of attention in any graphene related study on SiC substrates. In both the cases as shown in Fig 3.7, the cells are composed of Si-C bilayers with different stacking arrangements. The left part of Fig 3.7, shows 4H-SiC with the stacking arrangement as $ABCBA$.. and the right part of

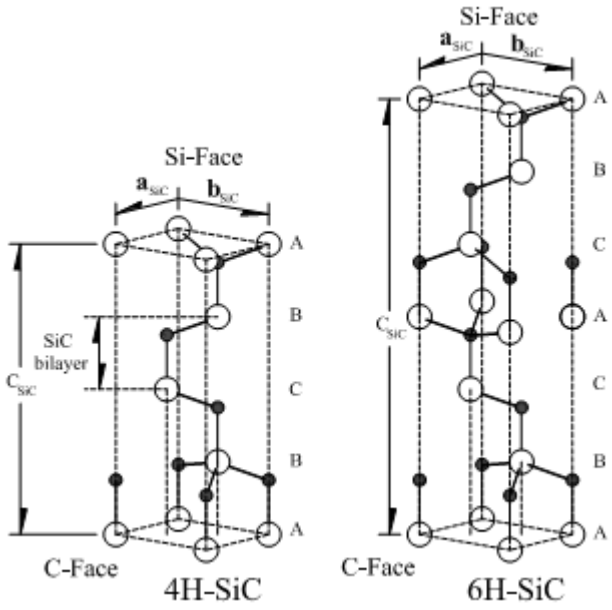

Figure 3.7: The unit cell structure of 4H- and 6H-SiC. Filled circles are carbon atoms and open circles are silicon atoms. Figure adapted from [12]

Fig 3.7 shows 6H-SiC with the stacking arrangement as $ABCACBA...$ As can be seen in the Fig 3.7, the Si terminated face SiC (0001) has one dangling Si bond per Si atom whereas the C terminated face SiC$(000\bar{1})$ has one C dangling bond per C atom. The C terminated face of 4H SiC is used as our substrate in our study of MBE growth of graphene.

Let us look at the lattice constants of both 4H and 6H SiC from the point of view of satisfying the epitaxy with graphene. Table 3.1, gives the in-plane and out-of-plane lattice constant values of both 4H, 6H SiC and graphene. Comparing

Table 3.1: Comparision of lattice constants of SiC and graphene

Material	a (Å)	c (Å)
4H-SiC	3.08	10.08
6H-SiC	3.08	15.12
Graphene	2.46	6.70

the in-plane lattice constants of hexagonal SiC with graphene, we conclude that there is a lattice mismatch of ~ 22 %. Although the lattice mismatch persists, but both 4H and 6H SiC would still be decent enough candidates for the MBE growth of graphene. But, we would concentrate our attention on the C terminated 4H-SiC

$(000\bar{1})$ with the motivation that the C terminated surface would act as a buffer layer when the first carbon monolayer would be deposited by MBE instead of a Si terminated surface. The highlight of my research is that the growth temperature would be much below the graphitization temperature so that we are assured that it is the deposited C atoms by MBE which crystallizes into a graphene lattice rather than the intrusive graphitization process. This would be discussed further in Chapter 5 where it will be shown with the help of RHEED that unlike in the case of graphene grown on c-plane sapphire, graphene grown on 4H-SiC $(000\bar{1})$ will be clamped to the substrate. This will be confirmed by a conformal morphology of the graphene films shown in the AFM images unlike a faceted surface seen in the graphene-sapphire system.

3.4 Epitaxial growth techniques

Monolayer to many-layered graphene films were grown by Molecular Beam Epitaxy (MBE) on two different types of insulating substrates with hexagonal symmetry: c-plane sapphire and 4H-SiC $(000\bar{1})$ with the goal of growing flatter graphene films on a wafer scale. In this section, I will describe the MBE system used for the growth of these films, the method of substrate preparation before the growth and the in-situ Reflection High Energy Electron Diffraction (RHEED) technique which is the integral part of any MBE growth.

3.4.1 Molecular beam epitaxy growth chamber

The MBE chamber dedicated for the growth of graphene is a part of four MBE chamber-network and includes an XPS chamber interconnected by UHV transfer tubes. The other MBE chambers were dedicated for their own specific applications. The graphene MBE chamber (System D) has a base pressure of 1×10^{-10} torr. The schematic of the chamber is shown in Figure 3.8.

For the purposes of MBE, controlled growth rate of Carbon is achieved by

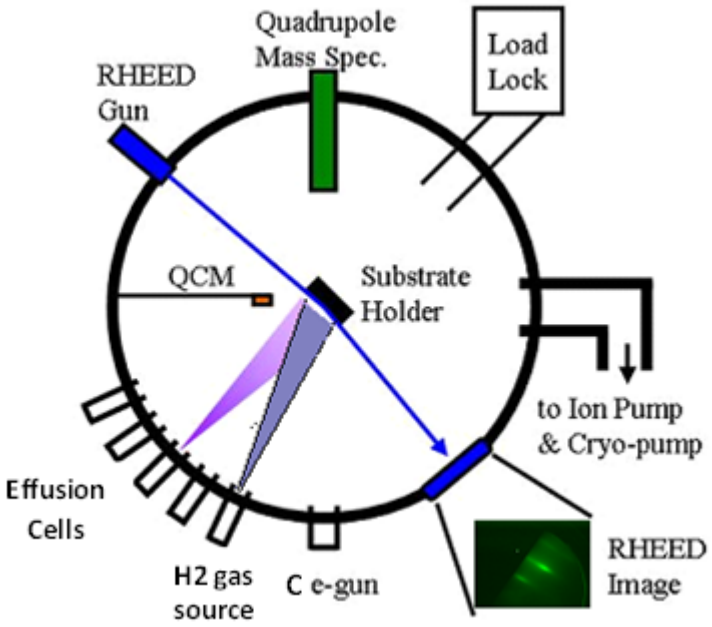

Figure 3.8: Schematic of the Carbon MBE Chamber, Figure adapted from [13]

electron gun evaporation of very high purity pellets of Highly Oriented Pyrolytic Graphite (HOPG). This is a single pocket e-gun in which 10 kV electrons are steered by electromagnets into the source material which sits in a water-cooled copper hearth. Since the melting point of graphite is beyond 3000°C, it is the perfect candidate to be an e-gun source material to be heated up by electron bombardment. The C flux is set by varying the filament current of the e-gun where a stable flux can be achieved for up to 2 hours, which becomes crucial for the growth of graphene thin films. Typically the pressure in the MBE chamber during an actual growth process when the electron gun is operational is 8×10^{-9} torr.

System D is also equipped with a gas injector for Hydrogen and Ethylene. Depending on the application, a specific gas source is introduced. An ultra-high purity lecture bottle is attached to a valve manifold mounted near the chamber. The manifold includes a series of on/off regulating valves that branched off in one direction to a turbo-molecular pump and, in the other direction, to a precision leak valve mounted on the chamber. The turbo-molecular pump is used to reduce

the gas pressure behind the leak valve. Inside the vacuum system, a long aspect-ratio tube (12 in $\times$ $\frac{3}{4}$ in) directed the gas flow towards the substrate. With the precision leak-valve, the chamber pressure can be controlled from 10^{-9} torr to 5×10^{-6} Torr.

The substrate heater is modified to take a filament current as high as 22.5 Amps yielding a temperature close to 1050°C which is typically the growth temperature we used for graphene films. In order to attain this high a growth temperature, the growth pucks have been machined to hold the substrate at an off-center position where the filament on the substrate heater is the hottest. This limits the use of RHEED (to be described in the later section) to just one azimuth; but it solves the purpose of attaining higher substrate temperature required for our growths. The substrates used for the growth are back sided coated with 5000 Å of Nb for optical pyrometry which is used to measure the temperature of these transparent substrates. The emissivity of 0.2 is used for the pyrometry studies in order to read the temperature at the center of the substrate which is radiatively heated. This value of emissivity is close to that of Nb which is used for back-side coating these transparent substrates.

System D is also equipped with doping effusion cells which can go as high as 1600°C for its own specific applications. Other features of the MBE chamber include a Quartz Crystal Monitor (QCM) to measure atomic fluxes and RHEED to monitor the film growth during deposition. It also has a Quadrupole mass spectrometer to measure residual gases and for leak checking. The system has liquid nitrogen cryo-panels which are cooled during a growth process.

3.4.2 Substrate preparation

The substrates used for this thesis work are c-plane sapphire procured from Crystal GMBH and 4H-SiC $(000\bar{1})$ procured from CREE Inc. c-plane sapphire is the standard single side polished substrate. Whereas, 4H-SiC $(000\bar{1})$ substrates used in the MBE growths are available in double side polished form with the C termi-

nated side being chemical mechanical polished (CMP) for epitaxial growth and the Si terminated side being optically polished. The CMP polished side is devoid of any subsurface damage and has significantly fewer morphological defects than the optically polished side (which is full of deep and shallow trenches). This is the reason the CMP polished side (C terminated side in our case) is chosen as the epi-ready surface where the MBE growth happens. The 2" and 4" wafers procured from CREE were diced into 10 mm squares by American Precision Dicing Inc. Since these are double side polished substrates, great care has been taken to identify the right face of the wafer to grow upon. A small scratch mark on the optically polished side with a diamond scribe was enough to identify the epi-ready side during the course of mounting the wafer and its material characterization. All the samples discussed in this dissertation were grown on the C terminated side.

The first step of substrate preparation is coating the back side (optically polished of 4H-SiC $(000\bar{1})$ substrate and the unpolished side of c-plane sapphire) with Nb which is necessary for radiative heating and optical pyrometry. This is done by sputter deposition of 5000 Å of Nb. The epi-ready side is then scrubbed with cotton swabs dipped in trichloroethylene (TCE) to remove any grease or dirt. Further cleaning was done by sonicating in baths of TCE, acetone and isopropyl alcohol (IPA) (in this order) for 10 minutes each. Finally the sample was mounted on an open-back puck (for radiative heating) and inserted into the load-lock.

The substrate is outgassed in the heater stage of the chamber overnight at about 300°C and is ready for growth the next morning. The substrate is slowly ramped up to about 1050°C and is annealed at this temperature for about 90 mins before the start of the growth. All the growth processes discussed in this thesis were performed at 1050°C.

3.4.3 Reflection High Energy Electron Diffraction (RHEED)

RHEED is a surface sensitive technique used to monitor the crystal structure of the surface of the film during the growth process. In this arrangement, high energy electrons (upto 30 kV in System D) are scattered at a grazing angle ($\sim 1°$). Because of the grazing incidence of the electron beam, the penetration depth of the incident electrons is limited to the surface layer and the diffraction pattern formed by the scattered electrons captured on the phosphor screen shows the surface structure. This is the reason why RHEED is such a powerful technique used for monitoring thin film growth in-situ and is an indispensable diagnostic technique of any MBE growth process.

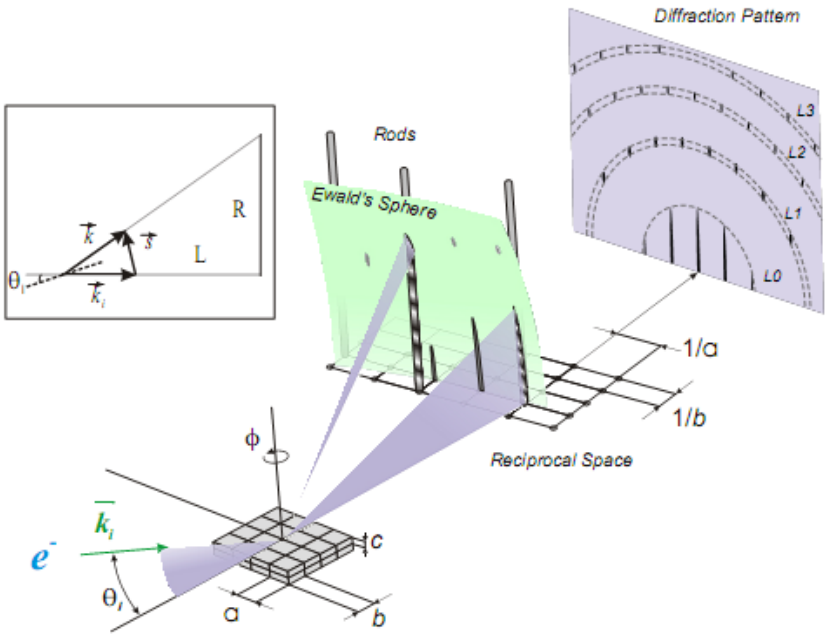

Figure 3.9: Schematic of the RHEED principle is shown; both the Ewald sphere and Laue zones (L0,L1,..) are shown. Inset: simplified kinematics of the electron scattering. Figure adapted from [14]

As depicted in Fig 3.9, the direction of the incident beam is defined with respect to a specific crystal orientation (zone axis), where ϕ is the angle between the projection of the electron beam on the sample surface and the zone axis. For a monolayer of atoms in two-dimension, the reciprocal space exhibits reciprocal lattice rods separated by the inverse lattice distances (a and b as shown in Fig

3.9). For these high energy electrons incident at such a grazing angle θ_i, the Ewald sphere is large. The RHEED diffraction pattern is a result of the intersection of the reciprocal lattice rods with the Ewald sphere. The diffraction pattern exhibits both streaks at low scattering angles and Bragg spots at higher angles in Laue zones. The fact that we have a small range of electron energies incident on the screen means that the Ewald sphere will have a finite thickness. The reciprocal lattice rods have a finite thickness as well dependent on the quality of the sample surface. Streaks appear in the place of perfect points when broadened rods intersect the Ewald sphere (which has a finite thickness). Diffraction conditions are fulfilled over the entire intersection of the rods with the sphere yielding elongated points or streaks along the vertical axis of the RHEED pattern. Streakiness in the RHEED pattern is a typical feature of single crystal epitaxial growth while the broadening of the streaks indicate small area of coherence on the surface. The brightness of the specular spot is a measure of the flatness of the film.

If the growth is completely polycrystalline, this implies the surface is an assembly of large number of randomly oriented crystallites. The effect of randomness signifies that the reciprocal lattice vectors lie on a sphere rather than a set of discrete points which is true for single crystals. The intersection of these reciprocal spheres with the Ewald sphere results in a diffraction pattern which is a series of concentric circles around the incident electron direction. These are called the Derby-Scherrer rings.

As will be discussed later in Chapter 5, the growth of graphene films on both c-plane sapphire and 4H-SiC $(000\bar{1})$ always starts in an epitaxial manner with streakiness in RHEED. When grown thicker, the epitaxy is lost and the rings start to develop. The typical diffraction pattern for a many layered graphene film is a superposition of rings and streaks which we term as "semi-epitaxial". If still grown thicker, the RHEED pattern is composed of rings with the complete absence of streaks which is defined as a pure polycrystalline phase.

The different analytical tools used to analyze the grown graphene films ex-situ will be described in the following chapter.

CHAPTER 4

ANALYTICAL METHODS FOR THE MBE GROWN FILMS

After the growth of graphene in the MBE chamber analyzed in-situ using Reflection High Energy Electron Diffraction (RHEED), the films are taken out for further material characterization ex-situ. Each of the different techniques employed for the systematic characterization of the grown samples will be described in detail here. These techniques include Atomic Force Microscopy (AFM) which is used to study the morphology of the grown films including Phase AFM which is employed to study the formation of two phases in graphene grown on 4H-SiC $(000\bar{1})$. X Ray Photoelectron Spectroscopy (XPS) is used to estimate the thickness of the grown films and to rule out the formation of graphitic domains in the annealed SiC substrates. Raman Spectroscopy, the fingerprint of graphene is used to estimate the crystallite domain size and to identify the defects in the film. Electrical transport measurements were done down to 4K using a He-4 cryostat in order to characterize the thin films and identify the transport behavior with the existing theoretical models. In this chapter, all these techniques used to characterize the samples will be described from the perspective of analyzing graphene thin films.

4.1 Atomic Force Microscopy (AFM)

AFM is a type of scanning probe microscopy that studies the topography of the grown graphene films. This employs a flexible cantilever with a sharp tip to scan the surface of the sample. The AFM relies on the deflection of the cantilever due to sample-tip interaction which is measured by reflecting a laser off the cantilever

through a photodiode array. The laser deflection signal is used as feedback to control the sample-tip relative position through a set of piezoelectric crystals. The positioning of the tip relative to the sample is then mapped to the surface topology. As the distance between the tip and the sample changes, a variation in the amplitude will occur which is corrected by a feedback loop in order to keep the amplitude of the tip constant. The schematic is shown in Fig 4.1. All the AFM scans involving the growths on 4H-SiC $(000\bar{1})$ and c-sapphire put forth in this dissertation have been acquired using the Asylum Research MFP-3D AFM.

An AFM can be operated in two basic modes; contact mode and tapping mode. In the contact mode, the tip is dragged across the sample surface and the photodiodes measure a static deflection. But, in the tapping mode, the cantilever is driven near resonance and the tip makes intermittent contact with the surface. In both the cases, the piezoelectric crystals control the tip to sample distance such that the static deflection (contact mode) or tip amplitude (tapping mode) is constant. The mode used for all the scans mentioned in this dissertation are in tapping mode.

4.1.1 Phase Imaging

The highlight of the tapping mode operation is that it can be used for phase imaging as well. As shown in Fig 4.1, as the oscillating cantilever tip encounters regions on a surface containing different physical properties, such as hardness and elasticity, a shift in phase will occur (lag in oscillation). By measuring the degree of the phase shift in unison with topography, it becomes possible to identify the variations in surface structure.

Variations in phase lag provide information necessary to detect variations in composition, adhesion, friction and visco-elasticity amongst others. Since phase imaging highlights variation in composition, it is unaffected by large scale topographic variations. Hence, this is an ideal extension of AFM providing information that would otherwise be obscured by rough topography.

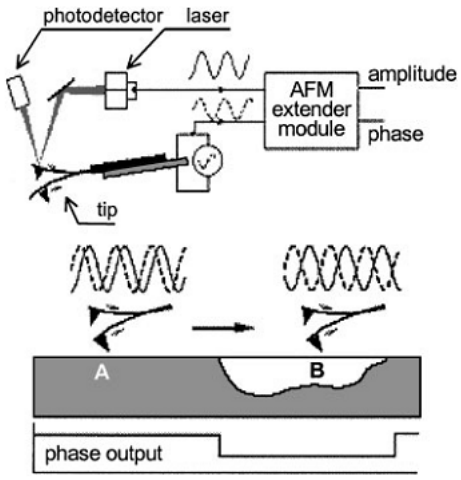

Figure 4.1: Diagrammatic representation of tapping mode with phase shift detection. A and B represent different component regions on a surface. Figure adapted from [15].

Phase imaging has been used a lot to study the bonding nature of the MBE grown graphene film with respect to the substrate. A lot of phase imaging has been particularly employed on the graphene films grown on 4H-SiC $(000\bar{1})$ as well as on the annealed 4H-SiC $(000\bar{1})$ substrates to study how the mechanical properties of the grown film differs from one half of the atomic terrace from the other. This will be discussed in detail in Chapter 5. Simple topographic scans could not have extracted this information which makes AFM phase imaging all the more powerful. All the phase scans discussed in this thesis have been done in single AC mode.

4.2 Raman Spectroscopy

Raman spectroscopy is one of the powerful and non-destructive optical technique based on inelastic scattering of photons. In the present context of this dissertation, this optical technique is widely used to probe properties of graphite, intercalated graphite, carbon nanotubes, fullerenes, carbon fibers etc. Raman spectroscopy has become such an important technique in the material analysis of graphene that it is indentified as a "fingerprint of graphene".

Raman analysis is widely used to study and identify different layers of graphene [17, 63] and to correctly estimate the number of layers in a sample. With the help of Raman Spectroscopy, one can identify the edge defects (armchair/zig-zag) in a graphite sample. This is advantageous in the study of the graphene nano-ribbons where the nature of the edge along with the width plays an important role in shaping the electronic properties [64, 65]. The effect of chemical doping and the effect of doping due to the substrate on the graphene electronic structure can be studied effectively with the help of Raman Spectroscopy [66, 67, 68]. Furthermore, since the epitaxial multi-layered graphene grown on 4H-SiC $(000\bar{1})$ exhibits linear dispersion (quasi-2D graphene) due to rotational stacking faults [52, 69], Raman spectroscopy could be a powerful tool to analyze the stacking disorder in this and other new graphene-based material systems.

As far as the basic working principle of Raman Spectroscopy goes, the impinging photons from the light source inelastically scatter due to interaction with phonons of the vibrations in the lattice. This results in the energy of the photons being red or blue shifted. This Raman shift provides us information about the different phonon modes in the lattice. As shown in Fig 4.2, in the red-shift mode, commonly known as the Stokes scattering, the photon loses its energy to the lattice after the inelastic scattering. On the other hand, in the blue-shift mode, the photon gains energy after the inelastic scattering commonly known as the Anti-Stokes scattering. When there is no Raman effect at all, it is called Rayleigh Scattering. All the Raman analysis described in this dissertation will be Stokes Raman Scattering.

Incident light interacts with the atom in the lattice and induces an oscillating dipole moment p in the atoms given by $p = \alpha E$ where α is the polarizability and E is the electric field of the incident light given as $E_i = E_0 cos(\omega_i t)$. The total polarizability α is given by the sum of the electronic (α_e), ionic (α_i) and dipolar (α_d) contribution given as $\alpha = \alpha_e + \alpha_i + \alpha_d$. Hence, the total induced dipole

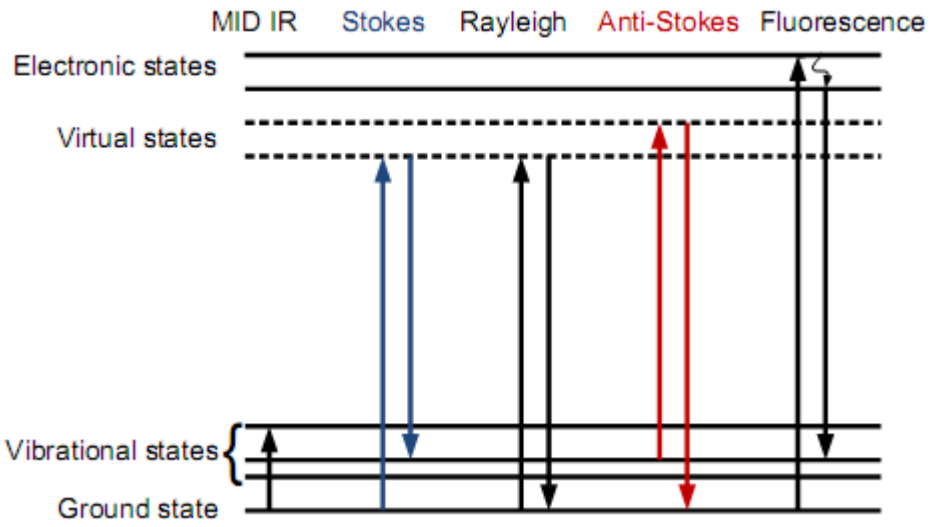

Figure 4.2: Illustration of different energy transition processes. Raman scattering can occur as Stokes or Anti-Stokes process. Figure adapted from [16]

moment from the electric field is given by the following :

$$p = \alpha E = \alpha E_0 cos(\omega_i t) \tag{4.1}$$

Molecular polarizability changes with bond length given as :

$$\alpha = \alpha_0 + (r - r_{eq})\frac{d\alpha}{dr} \tag{4.2}$$

And the bond length oscillates at vibrational frequency given as :

$$r - r_{eq} = r_{max} cos(\omega_{vib} t) \tag{4.3}$$

Combining Eq 4.2 and Eq 4.3, we see that polarizability oscillates at vibrational frequency given as :

$$\alpha = \alpha_0 + (\frac{d\alpha}{dr}) r_{max} cos(\omega_{vib} t) \tag{4.4}$$

Putting Eq 4.4 in Eq 4.7, we can clearly see the 3 contributions that can happen

due to the inelastic scattering of photon given as :

$$p = \alpha_0 E_0 cos(\omega_i t) + \frac{1}{2} E_0 r_{max} \frac{d\alpha}{dr} [cos((\omega_i + \omega_{vib})t) + cos((\omega_i - \omega_{vib})t)] \qquad (4.5)$$

where $cos(\omega_i t)$ is the Rayleigh contribution, $cos((\omega_i + \omega_{vib})t)$ is the Anti-Stokes contribution and $cos((\omega_i - \omega_{vib})t)$ is the Stokes contribution which are shown in Fig 4.2. All the Raman analysis done in this dissertation is in the Stokes mode.

4.2.1 Phonon modes in graphene

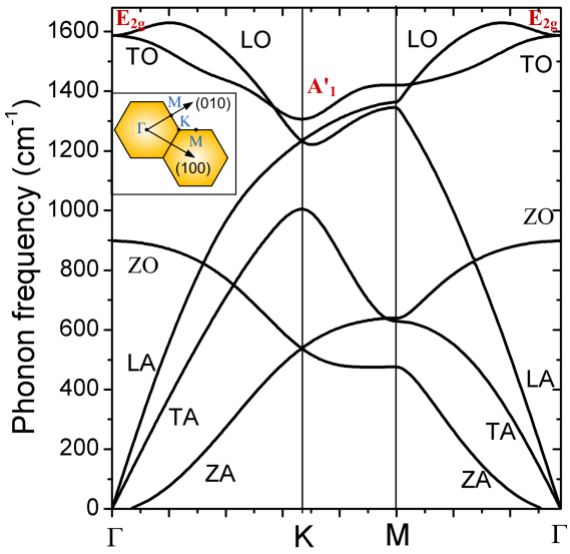

Figure 4.3: Calculated phonon dispersions along **ΓK**, **KM** and **MΓ** directions. Figure adapted from the PhD Thesis [16]

Phonon dispersions in graphene are responsible for some of its exotic properties. The 2D graphene lattice has two carbon atoms per unit cell which gives us six phonon dispersion branches. Three phonon modes are acoustic (A) and three are optical (O). In case of both acoustic and optical phonon modes, one is out-of-plane (Z) and the other two are in-plane, longitudinal (L) and transverse (T). Hence, the six phonon modes LO, TO, ZO, LA, TA and ZA are plotted along the high symmetry points **ΓK**, **KM** and **MΓ** as shown in Fig 4.3. The inset of Fig 4.3 shows the high symmetry points **Γ**, **K** and **M** in the 2D Brillouin zone.

At the **K** point, the LO (optical) and LA (acoustic) branches meet resulting in a doubly degenerate phonon with $\mathbf{E}^{'}$ symmetry. The phonon modes LO and TO are degenerate at **Γ** point and they are Raman active. The phonon mode ZO is infrared inactive. Along the **Γ**-**K** direction, LO and TO branches have $\mathbf{T_3}$ and $\mathbf{T_1}$ symmetries respectively.

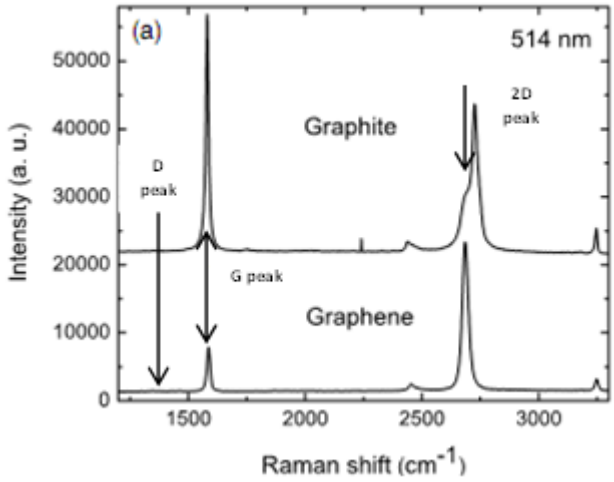

Figure 4.4: Raman Spectrum of exfoliated graphene on SiO_2 compared with bulk graphite. This figure does not show the D mode. Figure adapted from [17].

According to the Raman fundamental selection rule $\mathbf{q} \sim \mathbf{0}$ where $\mathbf{q}$ is the momentum of the inelastically scattered phonon, all unit cells must vibrate with the same phase. The second order modes are allowed as $\mathbf{q} + (-\mathbf{q}) = \mathbf{0}$. The three primary phonon modes that propagate in graphene are **G**, **D** and **2D** (or $\mathbf{G}^{'}$) shown in Fig 4.4 and described as follows :

G Mode: The G mode is typically observed at 1580 cm^{-1} and follows the selection rule ($\mathbf{q} \sim \mathbf{0}$). This is a typical mode of graphene and its derivatives and other carbon-based forms. This indicates the presence of an sp^2 network of carbon atoms. The occurence of the G peak is due to a one-phonon process involving **Γ** point optical phonons. As shown in Fig 4.3, the phonon modes LO and TO (E_{2g} symmetry) are doubly degenerate at the Brillouin zone center **Γ** and are Raman active for a graphene-like network. Fig 4.5(a) shows the bond stretching process in the sp^2 bonded carbon network responsible for the G peak. As explained by Basko

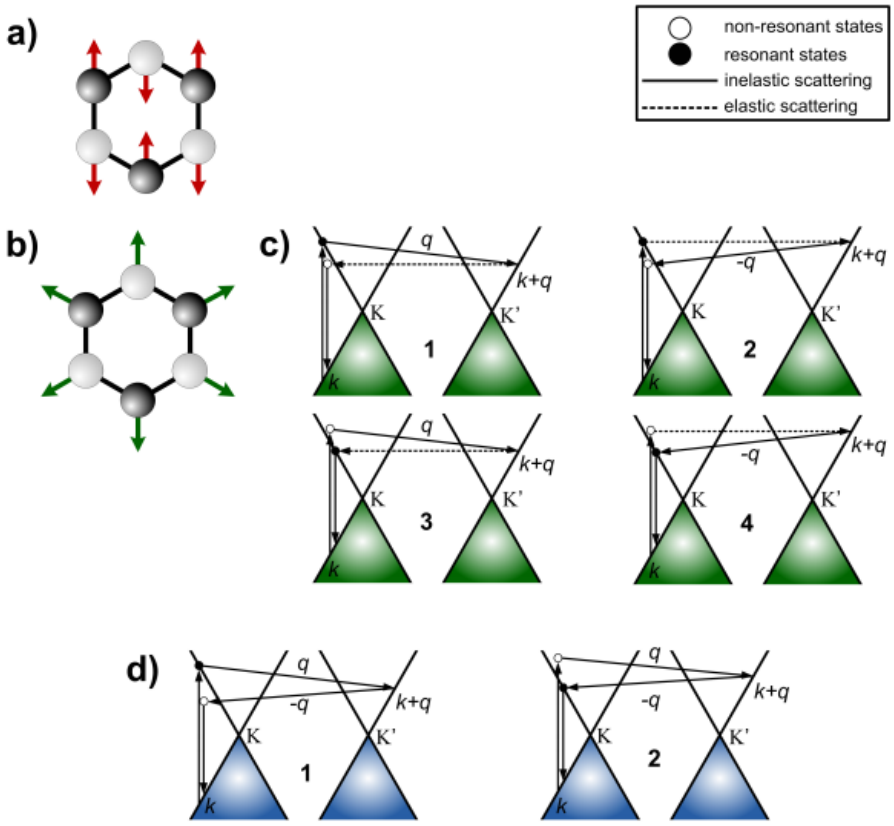

Figure 4.5: (a)Bond stretching process in Raman allowed G mode. (b) D mode breathing process which is a Raman disallowed mode and is seen only in samples with disorder and defects. (c) One phonon double-resonance intervalley process for D mode. (d) Two phonon double-resonance intervalley process for 2D mode

[70], if one approximates the electronic spectrum of graphene by Dirac cones, then the main contribution to the Raman amplitude for G mode comes from the regions of the electronic Brillouin zone far from the Dirac points. Thus the Raman process for G mode is completely off-resonant. As a result, the intensity of the peak is expected to be insensitive to most external parameters like polarization, electron concentration, degree of disorder, laser excitation energy etc.

D Mode: The D mode is a Raman disallowed mode in a defect-free graphene lattice. It occurs at 1355 cm^{-1} and is a breathing mode of A_{1g} symmetry involving phonons near the **K** zone boundary shown in Fig 4.5(b). The deviations from the ideal graphene lattice due to atomic scale defects, finite domains, nature of the edge, stacking faults etc are some of the reasons for the occurence of this mode.

The D mode is dispersive and it varies with the photon excitation energy. As explained by Ferrari [71], the intensity of the D mode is strictly connected to the presence of six-fold aromatic rings. The ratio of the intensity of the D peak to that of the G peak varies inversely with L_a and the size of the crystallite is given by [72]:

$$\frac{I(D)}{I(G)} = L_a(nm) = (2.4 \times 10^{-10})\lambda_l^4 \left(\frac{I(D)}{I(G)}\right)^{-1} \tag{4.6}$$

where λ_l is the laser wavelength in nm and L_a is the size of the crystal domain or in-plane correlation length.

Fig 4.5(c) illustrates the intervalley (between inequivalent $\mathbf{K}$ and $\mathbf{K}'$ points) double resonance process for D mode. In Fig 4.5(c1), an incident photon resonantly excites an electron in the valence band (π) to the conduction band (π^*). The electron then scatters inelastically by emitting a phonon of momentum ($\hbar\mathbf{q}$) to a conduction band state in $\mathbf{K}'$. The electron is further backscattered by a defect through a non-resonant elastic process. The electron then recombines with the hole by a non-resonant process. In the second process, Fig 4.5(c2), the inelastic backscattering from defect due to emission of phonon ($-\hbar\mathbf{q}$) occurs, after the elastic scattering from $\mathbf{K}$ and $\mathbf{K}'$. In process Fig 4.5(c3) and Fig 4.5(c4), π to π^* transition due to incident photon is non-resonant and the electron-hole recombination process is resonant. In the double resonant process, either the initial state or the final $\mathbf{k}$ state is a real state and $\mathbf{k}+\mathbf{q}$ is always a real electronic state. The two real electronic transitions, the vertical transition between the hole state and the electron state and the intervalley transition makes it a double resonant process but not a fully resonant process.

2D Mode: The 2D mode is a second order mode in the Raman spectrum and is an allowed mode ($\mathbf{q} + (-\mathbf{q}) = \mathbf{0}$). The 2D mode is very sensitive to the stacking order in graphite and its analysis can be extended to multi-layer graphene with rotational stacking faults. As explained by Ferrari [17], the shape of the 2D peak changes with the number of layers of graphene as shown in Fig 4.6. We can also see that this mode is highly dispersive with respect to the change in the laser

excitation energy.

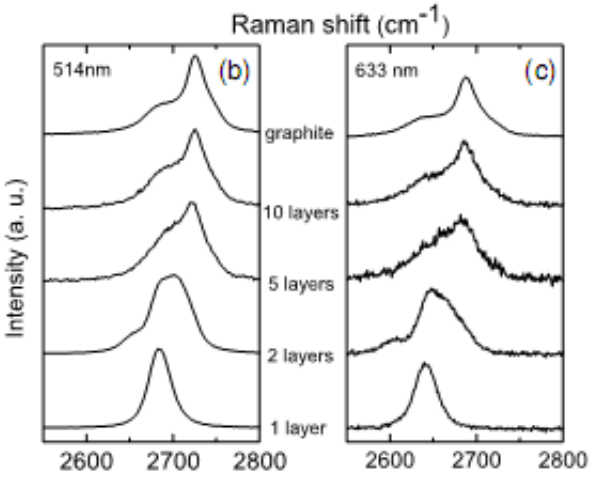

Figure 4.6: Evolution of the 2D mode with the number of layers shown for 2 different laser excitation energies. There is an upshift of the 2D peak with increase of laser excitation energies [17]

.

This mode originates from a double resonance process between the inquivalent $\mathbf{K}$ and $\mathbf{K}'$ points. Two phonons are involved in this process as shown in Fig 4.5(d). In the first process Fig 4.5(d1), the incident photon resonantly excites an electron from π to π^* band. The electron then scatters inelastically by emitting a phonon of momentum ($\hbar\mathbf{q}$) to a conduction band state in $\mathbf{K}'$. The electron backscatters inelastically by emitting a phonon ($-\hbar\mathbf{q}$). The electron then recombines with the hole in $\mathbf{K}$ by a non-resonant process and emits a scattered photon. In process Fig 4.5(d2), the π to π^* is non-resonant and the electron-hole recombination after the two-scattering process is resonant. Since both of these processes involve real intermediate states, this is a fully resonant process.

Ferrari [17] explains why the 2D peak shape changes with the number of layers of graphene by taking the example of bilayer graphene and comparing it with a single layer as shown in Fig 4.7. Within double resonance, Raman scattering is a fourth order process involving four virtual transitions as shown in Fig 4.7(a) and Fig 4.5(d). The fact that the shape of the 2D peak changes as we have many-layered graphene sample is explained by taking a bilayer graphene case in

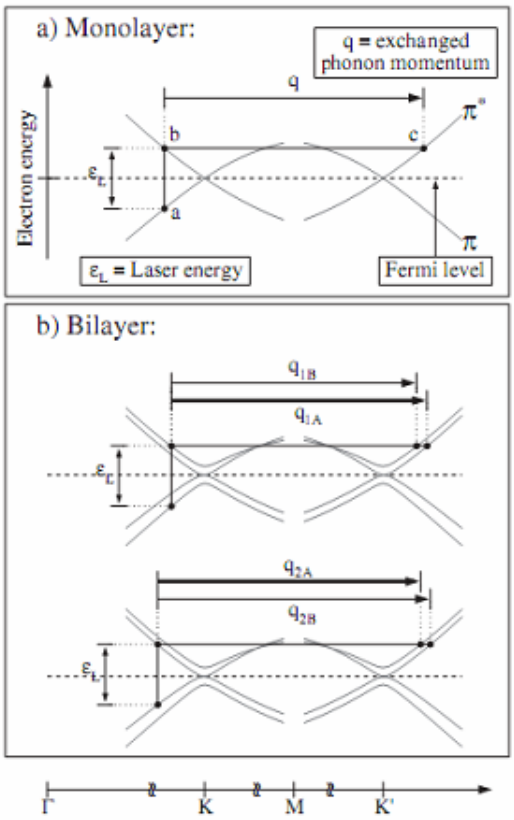

Figure 4.7: Double resonance for the 2D peak in a single and bilayer graphene [17]

.

Fig 4.7(b). In the bilayer case, the interaction of the graphene planes causes the π and π^* bands to divide in four bands, with a different splitting for electrons and holes as demonstrated in Fig 4.7(b). Ferrari [17] analyzes the resulting four processes involving phonons q_{1A}, q_{1B}, q_{2A} and q_{2B} which effectively contribute to the 2D peak; they produce four different peaks in the 2D band of bilayer graphene. Hence, the 2D peak of bilayer graphene is famously fit to four lorentzians. In stark contrast, a single layer graphene has effectively only one q phonon exchange; hence it is fit to a single lorentzian.

It will be seen later in Chapter 6 that the 2D peak shape of multilayered graphene films grown on c-plane sapphire and 4H-SiC $(000\bar{1})$ does not change with thickness because of the loss of **AB** stacking order. It will be discussed that the 2D peak position would disperse to higher wavenumbers with respect to

thickness in case of the graphene grown on c-plane sapphire. Whereas it will disperse to lower wavenumbers with respect to thickness in case of graphene grown on 4H-SiC $(000\bar{1})$. This is in contrast to the case of exfoliated graphene discussed above.

4.2.2 Raman spectrum of epitaxial graphene on SiC

In the Raman spectra of graphene grown on c-sapphire, the substrate related peaks are nowhere to be seen in the typical graphene wavenumber range. But, the Raman spectrum of epitaxial graphene grown on SiC has the typical peaks of graphene overlapping with the substrate induced peaks as shown in Fig 4.8. The D and G peaks lie exactly in the same region where there are several spectral features due to the SiC substrate itself. Only the 2D peak lies in a region devoid of any substrate spectral features. The situation is quite different from the exfoliated graphene on SiO_2 case as shown in Fig 4.4. Hence, this requires careful subtraction procedure in order to extract the D and G peaks and get a careful ratio of the intensities $\frac{I(D)}{I(G)}$ ratio in order to estimate the crystallite domain size . This will be discussed at length in Chapter 6.

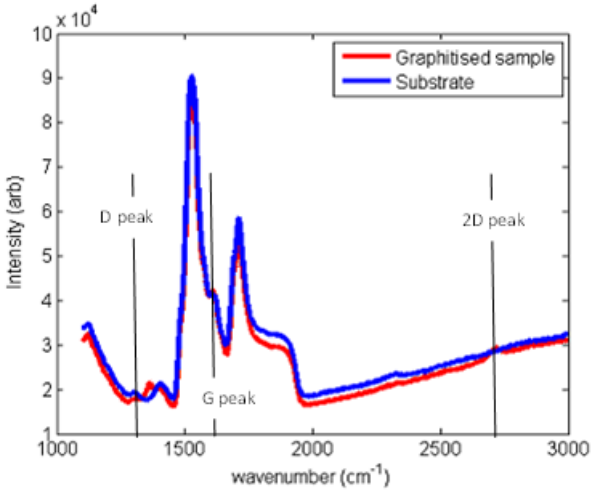

Figure 4.8: Raman Spectrum of a graphitized SiC sample compared to an un-graphitized SiC substrate. Figure adapted from PhD Thesis [18]

As in the case of exfoliated graphene on SiO_2, the analysis of counting the

number of graphene layers in epitaxial graphene on SiC is not that straightforward. As mentioned earlier, the 2D peak shape of exfoliated graphene changes as more number of layers are added on top of the other [17]. But, in the case of 4H-SiC $(000\bar{1})$ as well as c-plane sapphire (the substrates used for MBE growth of graphene discussed in this dissertation), the situation is entirely different. The 2D peak can be fit to a single Lorentzian as one does best for single layer exfoliated graphene [52, 69, 73, 74]. Hass [52] and Latil [69] have tried to explain why multilayer graphene on SiC (C terminated case in particular) behaves like a single sheet of graphene. Hass explains that a new stacking sequence in C-face grown films preserves the electronic symmetry of an isolated graphene sheet. Unlike in Si-face films, C-face epitaxial films do not grow as a simple **AB** stacked graphite film. Instead, graphene grows with a high density of rotational faults where adjacent sheets are rotated relative to each other from the SiC bulk direction. Because of this faulted stacking sequence, adjacent rotated planes become electronically decoupled preserving the Dirac dispersion at the K-point. For this misoriented stacking sequence of graphene layers also called as "turbostatic" graphite, Latil states that direct experimental evidence of Dirac fermion behavior cannot be considered as a discriminating property between single-layer and multilayer systems. Faugeras [73] tries to explain the difference between the "turbostatic" graphite and few layer graphene grown on the C-face of SiC; the 2D peaks are much wider in the former case accompanied by a D peak due to appreciable disorder and small size of graphitic granulates. Lee et al [74] transferred the epitaxial graphene grown on Si-face of SiC to SiO_2 and found that the 2D peak shape starts to develop an asymmetry with respect to the number of layers similar to the exfoliated graphene. They conclude that the stacking sequence of the graphene layers in epitaxial graphene is not solely responsible for the symmetric nature of the 2D peak as the stacking sequence does not change on transferring the layers to a SiO_2 substrate. They [74] also observed that the 2D peak position disperses with the number of layers of graphene consistent with the exfoliated graphene case. But, as will be seen in Chapter 6 in case of graphene grown on C terminated

4H SiC, the 2D peak position shifts to lower wavenumbers with increase of thickness in contrast to what is seen in the exfoliated graphene case. The 2D peak of graphene grown on c-plane sapphire also disperses with thickness similar to exfoliated graphene.

4.2.3 Description of the Raman setup used

Figure 4.9 depicts the home-built Raman setup used to measure all my MBE grown graphene samples. This setup is housed in a big black box to get rid of stray light rays in Prof David Cahill's lab in the fourth floor of Materials Research Lab.

As depicted by arrows in Fig 4.9, a monochromatic light beam of wavelength 488 nm is used, the power of which is controlled by an attenuator (not shown in Fig 4.9). The maximum laser power is 20 mW; but the laser power used for all the Raman measurements is $\sim 0.3\ mW$ with the spot size being 10 μm. The laser beam is directed towards the dichroic mirror (d) and is focussed normally onto the sample through the objective lens (c) of focal length 10 mm. The sample is mounted on a motorized sample stage (a) and is illuminated by a lamp (b). After scattering off the sample, the elastic and the inelastic scattering is collected at the dichroic mirror which reflects the elastic component (the laser light) and transmits the inelastic component through a notch filter (f) to be focussed (lens (g)) onto the slit (h). The inelastic Raman component of the light then enters the commercialized Insight system which houses the grating and the monochromator. The signal is finally collected via a CCD camera which is a part of the Insight system. The spectral resolution of the system is governed by the slit width and is a product of slit width and the dispersion. The grating used for all my measurements is 1200 grooves/mm with a resolution of 0.12 nm (5 cm^{-1}). In order to function correctly, the Spectrograph needs 10 minutes for the CCD detector to cool down to its operating temperature (- 60 °C).

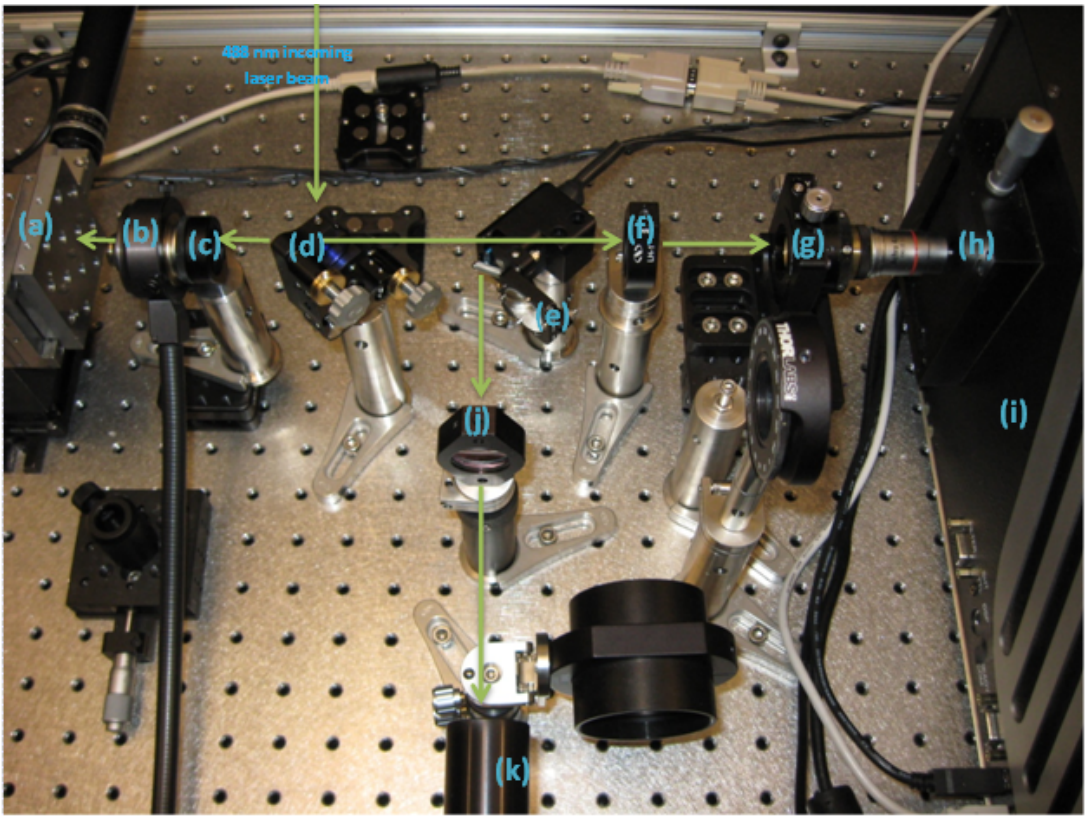

Figure 4.9: Raman Setup which consists of (a) Motorized Stage where the sample is mounted, (b) Light source to illuminate the sample surface, (c) Objective Lens, (d) Dichroic Mirror, (e) Flippant mirror when "up" diverts the light towards the camera, (f) Notch filter, (g) Focussing Lens,(h) Slit, (i) The Insight System from Princeton Instruments which houses the grating, monochromator and the CCD camera, (j) Focussing Lens, (k) Camera to record the image of the sample surface

4.3 X ray Photoelectron Spectroscopy (XPS)

XPS alternatively known as Electron Spectroscopy for Chemical Analysis (ESCA) is one of the most powerful surface analytical technique widely used for the investigation of solid surface chemistry. XPS spectra are obtained by irradiating a material with a beam of X-rays while simultaneously measuring the kinetic energy and the number of electrons that are emitted from the top few layers of the material being analyzed. X-ray lines typically used for XPS are Mg-Kα (1253.6 eV) and Al-Kα (1486.6 eV). The emitted electrons are of two kinds-photoelectrons

and Auger electrons. The schematic of the process is shown in Fig 4.10.

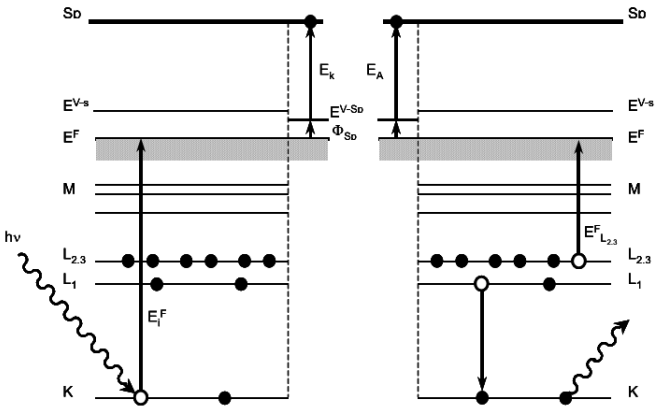

Figure 4.10: Left: Photoionization; Right: Auger processes. Adapted from [19]

The kinetic energy, KE of the photoelectron can be related to its binding energy (BE) by the following relation BE = $h\nu$ -KE -Φ_s; where $h\nu$ is the photon energy and Φ_s is the spectrometer work function. The X-ray photons have a penetration depth of the order of a micron, whereas the photo-electrons have a mean free path of the order of 10 Å. The photoelectrons from the depth of the material lose all of its kinetic energy to the inelastic scattering events in the bulk whereas the photoelectrons emitted from the first few tens of angstroms escape without any energy loss. The other photoelectrons that lose energy due to inelastic scattering but are still emitted simply contribute to the background of the spectrum. Hence, this technique is very surface sensitive.

On the other hand, the Auger Electron Spectroscopy (AES) as depicted in the right half of Fig 4.10 is emitted due to a secondary process. The excess energy of a relaxing outer electron is given to a neighboring electron; this additional energy can be enough to eject the electron from the atom. The Auger electron is insensitive to the energy of the incident photon. Hence, AES uses incident electrons instead of X-rays as a much higher incident flux can be achieved with electrons. Because of the secondary nature, the Auger electrons are often neglected in the XPS analysis.

4.3.1 Angle Resolved XPS (ARXPS)

In Angle Resolved X Ray Photoelectron Spectroscopy (ARXPS), by changing the angle of the electron energy analyzer with respect to the sample surface, one can vary the effective scanning depth. This angle is called the take-off angle. This is achieved by rotating the sample stage. The angle made by the electron energy analyzer (detector) with respect to the surface normal of the sample is called the emission angle (90-θ). As shown in Fig 4.11, the escape depth (z), the take-off angle (θ) and the attenuation length of the photoelectron emitted (λ) are related by the following equation :

$$z = 3\lambda \sin\theta \tag{4.7}$$

where the factor of 3 takes care that 95 % of the signal is emanated from a depth $< 3\lambda$.

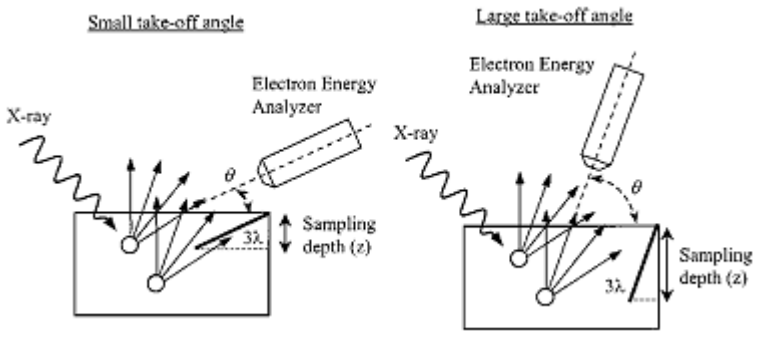

Figure 4.11: Schematic diagram showing the setup of angle resolved XPS

The smaller take-off angles have an effective smaller sampling depth than the larger take-off angles. Hence, the smaller take-off angles are much more surface sensitive. One way to vary the take-off angle is by tilting the sample stage as is done in all our XPS experiments discussed in this dissertation. The tilt of the sample stage for the ARXPS experiments is shown in Fig 4.12. Here the angle made by the X-rays with the detector is kept constant.

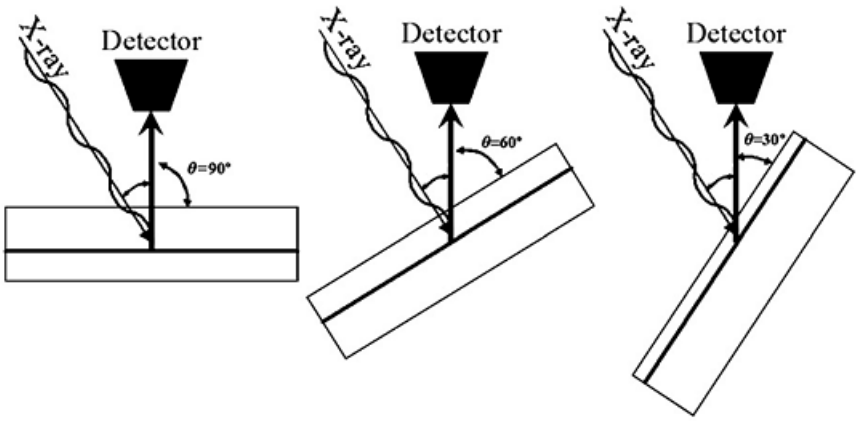

Figure 4.12: Tilting the sample stage, the sampling depth decreases.

4.3.2 Typical XPS spectrum of epitaxial graphene grown on SiC

XPS can be used to measure the thickness of graphene grown on SiC by measuring the film thickness by ARXPS. This technique is popular since it is self-calibrating as the graphitic C-C peak becomes intense at the cost of the attenuating C-Si peak shown in Fig 4.13. Fig 4.13 shows a typical C 1s core-level spectrum obtained from

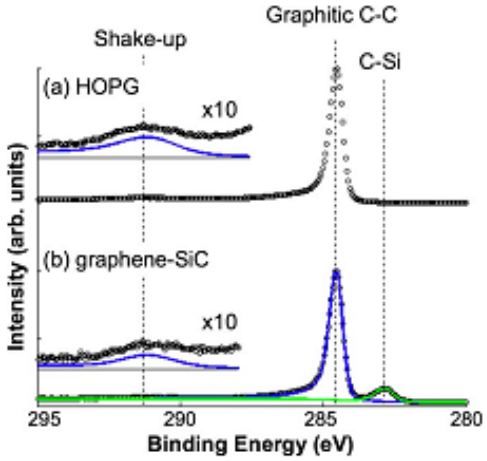

Figure 4.13: C1s XPS spectrum collected at $\theta = 90°$ (a) shows a reference HOPG substrate and (b) few layer graphene sample grown at 1500 ° C by thermal decomposition of SiC. Figure adapted from [20]

a few layer graphene (FLG) grown at 1500 ° C by thermal decomposition of SiC in ultra high vacuum; the spectrum from a reference Highly Oriented Pyrolytic Graphite (HOPG) sample is shown for comparison. As shown in [20], the spectra

from both HOPG and the 1500 ° C FLG sample show a main peak at 284.5 eV, indicating the presence of sp^2 hybridized C-C bonds. This peak at 284.5 eV is a signature of graphitic carbon. The small peak at 283 eV in the XPS spectrum in the graphene-SiC sample is due to carbon bound to silicon. Another signature of graphitic carbon is a weak peak at $\sim$ 291 eV which is identified as a shake-up satellite of the peak at 284.5 eV. Shake-up is a two electron phenomenon; the emitted photo-electrons with energy 284.5 eV can excite a π to π^* transition resulting in an additional peak at higher binding energies [75]. In order to estimate the thickness of the graphite grown on SiC, the approach proposed by Fadley [76] is used. The thickness is estimated from the ratio of the intensities of the graphitic C1s peak at 284.5 eV and the C-Si peak of SiC at 283 eV. This model will be discussed in greater detail in Chapter 5.

All the graphene samples grown on 4H-SiC $(000\bar{1})$ as well as on c-sapphire discussed in this dissertation have been scanned ex-situ using the Kratos Axis Ultra XPS system in the Center for Microanalysis and Materials (CMM), UIUC. We use XPS to confirm the graphitic nature of our samples and to find the thickness of the graphene films grown on both c-sapphire and 4H-SiC $(000\bar{1})$ as will be discussed in Chapter 5. The ARXPS measurements are done to find accurately the thickness of MBE grown graphene on 4H-SiC $(000\bar{1})$. XPS is also instrumental in detecting the evolution of the metallic nature of the annealed surface of 4H-SiC $(000\bar{1})$ which is the precursor to graphitization of this substrate to be addressed in the next chapter.

4.4 Electrical Transport

Electrical transport is the last step of the material characterization for a typical sample as this involves putting Ti/Au contact pads in order to reduce the contact resistance with the grown graphene film. The electrical measurements were done with a 4.2 K dipper probe. The probe allowed for four terminal resistance vs temperature measurements following the Van Der Pauw geometry. From these

measurements, we are able to deduce the kind of electrical transport that dominates the grown graphene film. The kind of electrical transport is very much dependent on the thickness of the grown film which will be described in greater detail in Chapter 7. The contact pads were deposited using a shadow mask made of Al which was especially designed so that there is enough clearance between the mask and the film. The design of the mask takes care that the surface of the film is not in contact with the mask at any point of time during the deposition of the contact pads. Typically, the contact pads of all the grown films have 30 nm of Ti which serves as a sticking layer followed by 100 nm of Au deposited in the e-beam deposition systems of the CMM.

CHAPTER 5

GROWTH AND MORPHOLOGY OF MBE GROWN GRAPHENE FILMS

In this chapter, the growth and morphology of the MBE grown graphene on the two hexagonal substrates: c-plane sapphire and 4H SiC (000$\bar{1}$) will be described in detail. The growth will be studied with the help of in-situ RHEED and the morphology of the grown graphene films will be studied with the help of ex-situ AFM where both height and phase topography will be employed. Phase topography is used to describe the morphology of the graphene films grown on 4H SiC (000$\bar{1}$). The thickness of the graphene films is estimated with the help of XPS.

It has been shown in Chapter 3 that although the lattice constant of c-plane sapphire is almost double to that of graphene, the way the graphene lattice aligns itself on the c-plane sapphire lattice, brings down the lattice mismatch to 12%. It will be shown with the help of RHEED that the growth starts in an epitaxial mode, progresses to being semi-epitaxial (where the epitaxy with the substrate starts to be lost) and if still grown thicker becomes polycrystalline. With the help of RHEED, an alignment scheme of the graphene lattice on the c-plane sapphire lattice will be proposed. AFM studies show that very thin grown graphene layers although locally flat are so strained to the substrate that they rupture into hexagonal shaped pits.

The growth of graphene on hexagonal SiC will be performed on the C terminated face of 4H-SiC (4H SiC (000$\bar{1}$)). In this chapter, it will be first established mainly by XPS that the 4H SiC (000$\bar{1}$) substrate annealed at 1050 °C (which is our growth temperature) does not form graphitic domains although Si desorption does take place. Although the lattice mismatch of graphene with 4H SiC (000$\bar{1}$) is

$\sim$22 % (already reported in Chapter 3), RHEED studies show that the graphene lattice does not relax with the progression of growth unlike what is seen in the c-plane sapphire case. RHEED studies further show that the graphene growth starts in an epitaxial manner and continues to become polycrystalline via a semi-epitaxial phase with increase of thickness. The thickness of the grown graphene layer is estimated by XPS where an angle resolved study is employed for a careful determination of thickness for very thin films. AFM studies via phase imaging show the formation of 2 phases in the grown graphene overlayer. It will be shown that each terrace in a grown film has 2 phases which is a consequence of how the C overlayer bonds to a Si desorbed portion of a terrace compared to a Si undesorbed portion.

5.1 Epitaxial graphene growth on c-plane sapphire

The single side polished c-plane sapphire substrates are back-side coated by sputter deposition with 5000 Å of Nb so that optical pyrometry can be used to measure the temperature of these transparent substrates. The epi-ready side is scrubbed with q-tips dipped in TCE followed by 10 minute sonication in baths of TCE, Acetone and Isopropyl Alcohol (in this order). The substrate is mounted on an off-axis puck and is immediately loaded into the load-lock of System D. While the off-axis open back puck limits the use of RHEED to just one azimuth, it does ensure that the substrate is radiatively heated by the hottest part of the filament of the substrate heater of the MBE chamber thereby giving us the highest substrate temperature for a given filament current. The substrate is degased at 300 °C overnight in order to remove the water vapor. The next morning, the substrate is slowly ramped up to 1050 °C and is ready to be grown upon. The growth rate of C is set at 0.1 Å/s confirmed by XPS and QCM measurements. The growth pressure in the MBE chamber is in the upper 10^{-9} range during the electron gun deposition of carbon with Liquid Nitrogen cooling the cryo shrouds.

5.1.1 Growth mechanism

The c-plane sapphire substrate is annealed at 1050 °C for 90 minutes which forms a flat surface with sharp terraces (Fig 5.6 LEFT) and a (1 × 1) RHEED pattern in Fig 5.1 (A) with Kikuchi lines. After this pre-growth anneal, the substrate is ready for electron gun deposition of carbon at this temperature.

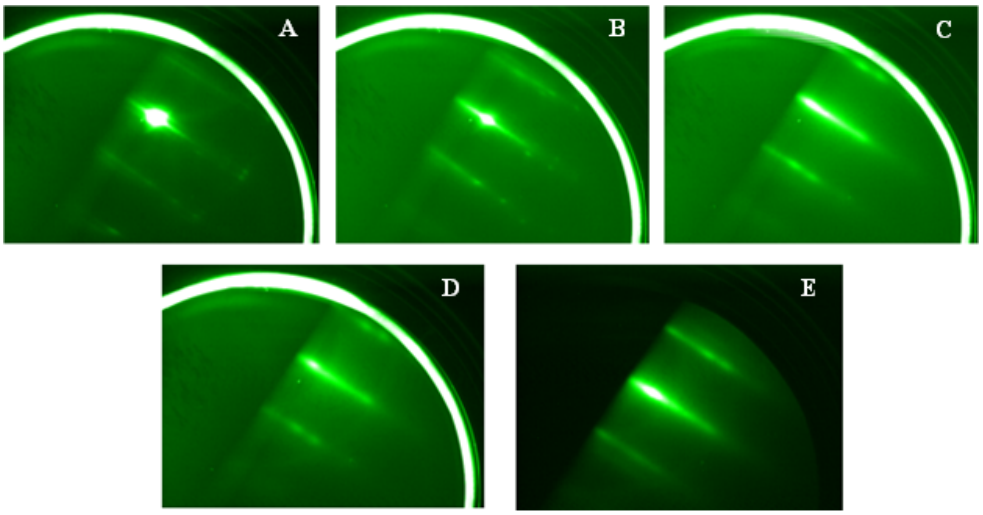

Figure 5.1: RHEED sequence showing the growth of graphene on c-plane sapphire. (A) c-plane sapphire substrate annealed for 90 minutes at 1050 °C before the start of the growth (B) after deposition of 1st ML of graphene (C) after 2nd ML (D) after 3rd ML (E) taken at room temperature.

It can be seen that with the deposition of the 1st ML of C shown in Fig 5.1 (B), the specular spot becomes slightly weaker than the starting surface shown in Fig 5.1 (A) and the ± 1 order streaks become more prominent. With the deposition of the 2nd ML of C shown in Fig 5.1 (C), the specular spot has elongated with the ±1 order streaks still intact showing that the growth occurs in an epitaxial manner. There is a subtle but important change in the RHEED when the 3rd ML of C shown in Fig 5.1 (D) is deposited. Finally, Fig 5.1 (E) shows a 3ML epitaxial graphene grown on c-plane sapphire after being cooled down to room temperature. The epitaxy is maintained up to the 5th ML which looks similar to the 3rd ML (not shown in Fig 5.1). But, beyond the 5th ML, polycrystalline rings emerge superposed with the streaks indicative of the progressive loss of epitaxy which we

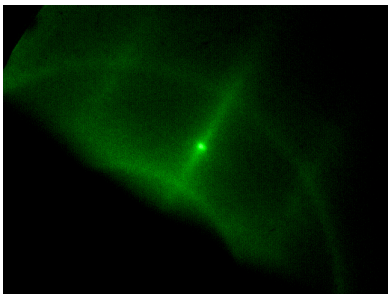

Figure 5.2: Typical "semi-epitaxial" RHEED of 6 ML graphene grown on c-plane sapphire showing superposition of both streaks and rings.

term as "semi-epitaxial" as shown in Fig 5.2. If still grown thicker than 7MLs, the streaks disappear completely and only rings can be seen; the growth becomes completely polycrystalline. Thus, in spite of the lattice mismatch, the first 3-4 MLs of C grows in an epitaxial manner following exactly the lattice structure of the underlying substrate described as a pseudomorphic growth process.

Relaxation of graphene lattice with progression of growth

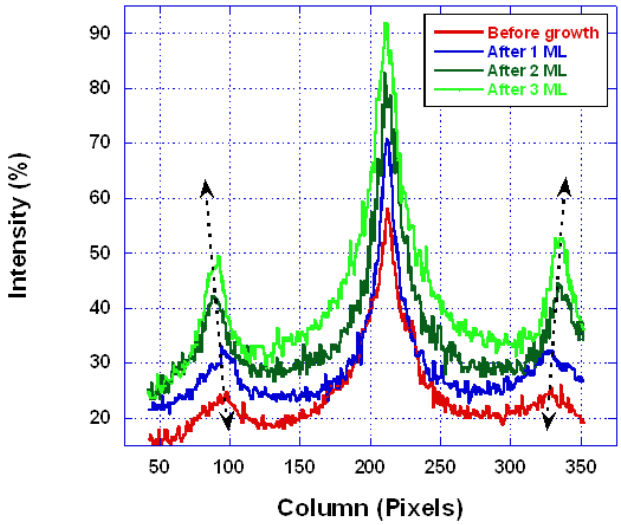

Figure 5.3: Intensity profile showing the evolution of the distance between ± 1 order streaks with the deposition of 3 MLs of graphene on c-plane sapphire. It shows the way the graphene lattice relaxes as the growth progresses.

Fig 5.3 shows the evolution of the RHEED intensity profile of 3 ML graphene (after growth) versus the annealed c-plane sapphire substrate (before growth).

It shows that the spacing between the ± 1 order streaks (the inverse of which is proportional to the lattice constant in the real space) increases as the growth progresses. With the deposition of the 1st ML graphene, the ±1 order streak spacing is exactly the same as that of the bare c-plane sapphire substrate which implies that the 1st grown graphene layer is clamped to the substrate signalling the presence of tensile stress in the film. But, as the 2nd ML is deposited, the graphene lattice tends to relax itself indicated by the increase in the spacing of the ±1 order streaks. With the deposition of the 3rd ML, the ±1 order streak spacing increases even further, thus releasing the tensile stress in the grown overlayer. The

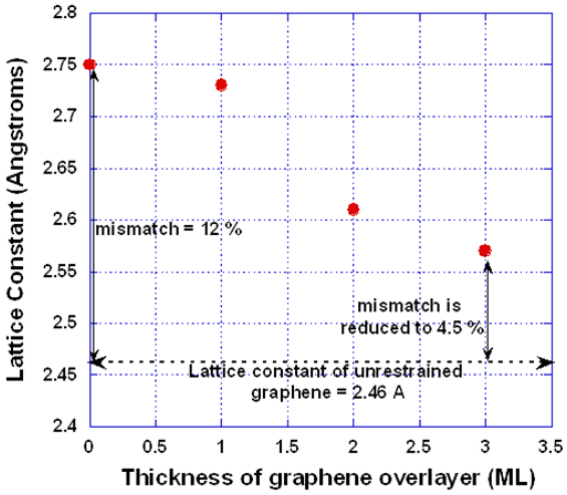

Figure 5.4: The lattice constant of every ML of graphene deposited decreases and approaches the unrestrained graphene lattice constant given by 2.46 Å. The lattice mismatch reduces from 12 % to 4.5 % with the deposition of 3rd ML.

±1 streak spacing does not change any further until the 5th ML beyond which polycrystalline rings emerge in the RHEED superposed with the streaks indicative of the progressive loss of epitaxy. The ±1 order streak spacing of the 3 ML graphene (after growth) is about 6 % higher than that of c-plane sapphire (before growth). Since the lattice constant of graphene is smaller than that of c-plane sapphire, the graphene lattice tends to relax to its original lattice constant devoid of any lattice strain as shown in Fig 5.4. This prompts us to find out how exactly the graphene lattice is aligned to the c-plane sapphire substrate. Following Fig 3.4, the lattice constant of c-plane sapphire is almost double of that of graphene.

According to the calculations made by the authors in [10], one carbon atom of an adsorbed carbon structure tends to bond to at least one oxygen atom of the sapphire lattice due to strong binding of carbon with oxygen atoms.

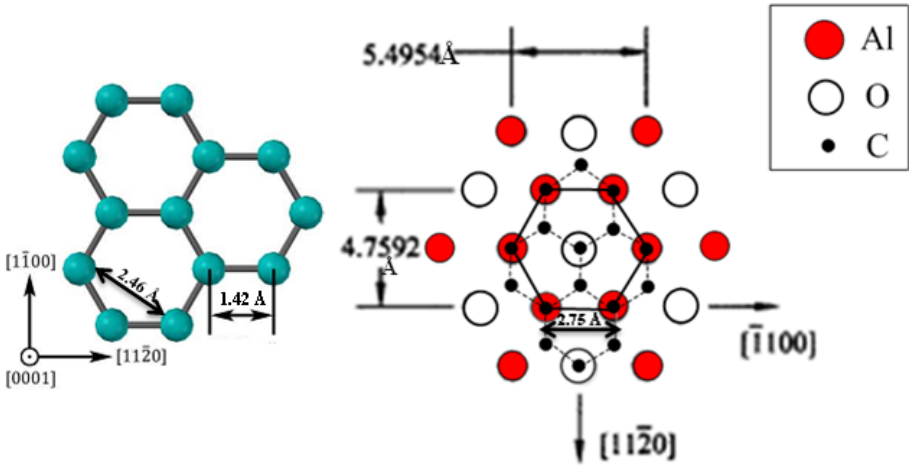

Figure 5.5: LEFT : shows the graphene lattice with lattice constant 2.46 Å. RIGHT : shows an alignment scheme of the graphene lattice on c-plane sapphire. C atoms in the graphene lattice separated by the lattice constant 2.46 Å can only align itself onto the inner hexagon of Al atoms separated by 2.75 Å.

Keeping in mind the lattice structure of the graphene and c-plane sapphire and the affinity of carbon atom to bond with oxygen atom [10], we propose an alignment scheme of the graphene lattice on the c-plane sapphire lattice shown in Fig 5.5. Fig 5.5 suggests that two C atoms separated by the lattice constant of graphene (2.46 Å) can align itself onto the inner hexagon of Al atoms in the sapphire lattice which are separated by 2.75 Å. This alignment scheme automatically takes care of the fact that at least one of the C atoms of the graphene lattice is seated on the oxygen atom as is required to lower its energy since C tends to bond with O with a binding energy of 2.78 eV lower than that of Al [10]. Following this alignment scheme, the bond between the C atoms in the graphene lattice will be stretched by $\sim$ 10 % thus confirming a pseudomorphic growth mode. This proposed alignment scheme of graphene lattice on the c-plane sapphire lattice yields a difference in the lattice constants of $\sim$ 12%. This is close to the value of the difference in the $\pm$ 1 order streaks seen in the RHEED intensity profile

shown in Fig 5.3 which is $\sim$ 6 %. Since the graphene lattice relaxes itself as the growth progresses, dislocations due to lattice mismatch occur as would be shown by hexagonal facets formed on the surface of the grown graphene overlayer studied by AFM.

5.1.2 Morphology of the graphene films grown

In this section, the morphology of the graphene films is studied with the help of AFM from thin epitaxial limit to completely polycrystalline limit. All the samples that will be discussed in this section have been grown at 1050 °C via electron gun deposition carbon at 0.1 Å/s. In spite of the lattice mismatch of graphene with the underlying c-plane sapphire substrate, the growth starts in an epitaxial manner resulting in smooth terraced films.

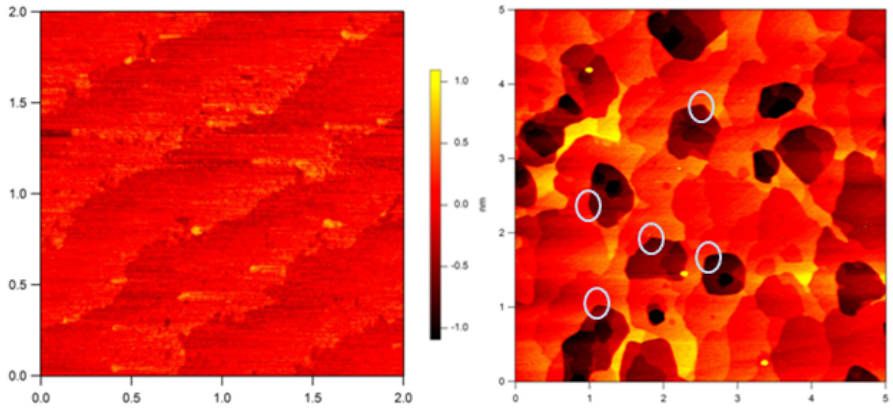

Figure 5.6: LEFT : 2 μm scan of a c-plane sapphire substrate annealed for 90 minutes at 1050 °C just before the growth. RIGHT: 5μm scan of a 3 ML graphene film grown on the annealed substrate. 120° facets are circled.

Fig 5.6 (LEFT) shows the height AFM scan of a typical 90 minutes annealed c-plane sapphire substrate. All the samples that will be discussed here have been subjected to this pre-growth annealing. This results in a flat surface with sharp atomic terraces favorable for epitaxial growth. A 3ML graphene film is deposited on such a pre-annealed surface via electron gun deposition shown in Fig 5.6 (RIGHT). It can be seen that the surface of the film is locally smooth with

hexagonal faceting which is the result of the misfit dislocations since the graphene lattice tends to relax itself as shown by RHEED. The first few monolayers are strained to the substrate as confirmed by RHEED. A Three Dimensional image of Fig 5.6 (RIGHT) is shown in Fig 5.7 where a hexagonal facet is identified. A section graph shows that the hexagonal facets are actually pits.

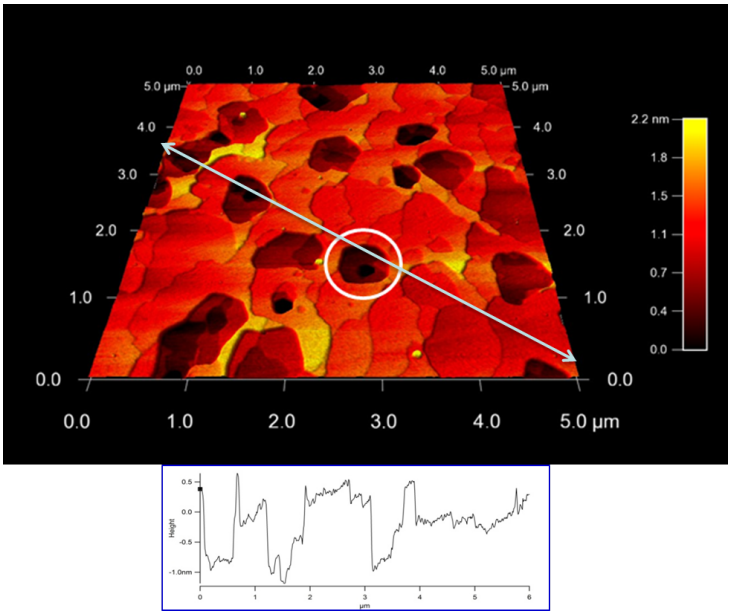

Figure 5.7: 3D AFM image of the 3ML graphene. A hexagonal facet is circled.

The facets grow in number as the next monolayer of graphene is deposited. An AFM image of a 4ML sample is shown in Fig 5.8 (LEFT). The film is still smooth with unfaceted regions of dimension of at least 250 nm. The film is in the epitaxial regime although the substrate terraces have now been buried by the graphene overlayer. If observed closely, 120 ° angled facets can be clearly seen as indicated in Fig 5.8 (RIGHT). The fact that the film is under a lot of tensile stress is the main reason of the rupturing of the film as confirmed from the RHEED intensity analysis. With the deposition of 5 MLs of graphene on the substrate shown in Fig 5.8 (RIGHT), the tensile strain in the film is released as the facets have shrunk in number. The 120 ° angled facets although less in number can still be observed. The film is still flat and smooth and is of epitaxial nature. But, looking at the RIGHT image closely, one can observe the slight emergence

of granular regions shown by the yellow patches as shown in Fig 5.8 (RIGHT). This indicates that if grown thicker than 5 ML, the polycrystalline order will set in and epitaxy will be lost.

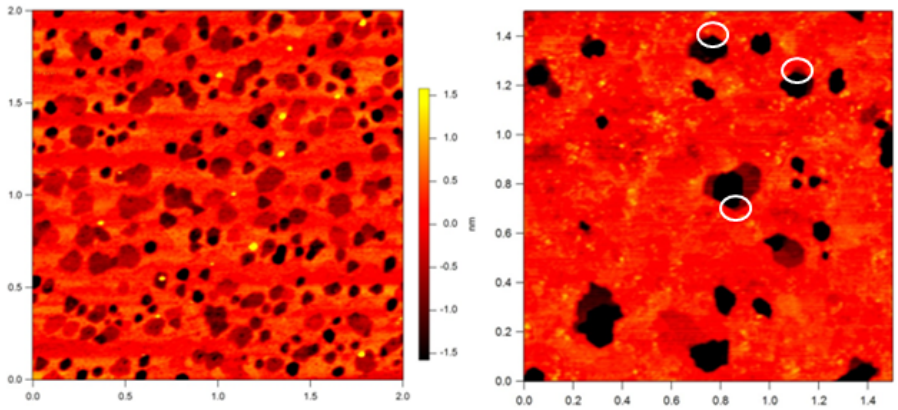

Figure 5.8: LEFT: 2 μm AFM scan of a 4ML graphene grown. It can be seen that although the facets have grown in number, the film is still flat and smooth. RIGHT: 1.5 μm AFM scan of a 5ML graphene film grown. Most of the facets previously seen have been buried. The presence of yellow patches in the flat regions show the emergence of granularity. The 120° facets are circled.

Fig 5.9 shows a 8ML graphene film grown on c-plane sapphire. As can be seen, the film has granular morphology confirmed by polycrystalline RHEED. When tensile strain starts to release after the growth of 5 epitaxial MLs of graphene (from RHEED analysis), loss of epitaxy sets in resulting in a polycrystalline film.

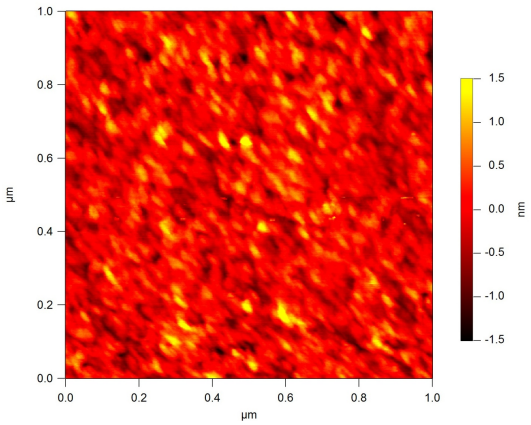

Figure 5.9: The AFM image shows a 1 μm scan of a $\sim$ 8 ML polycrystalline graphene where epitaxy with substrate is completely lost and it looks granular.

Thus, the graphene films grown on c-plane sapphire show a faceted surface where the hexagonal shaped facets are the dislocations that occur as the lattice strain relaxes with the progression of the growth. With increase of thickness, as polycrystalline order sets in, the facets are completely buried resulting in a completely granular surface.

5.1.3 Estimation of thickness from XPS studies

The thickness of graphene grown on c-plane sapphire is estimated by X-Ray Photoelectron spectroscopy. The angle of the detector with respect to the surface normal is always fixed at $\theta = 0°$. The thickness of graphene grown is given by the formula described in Eqn 5.1 [20]. The detailed derivation is done in the next section where the thickness of graphene grown on SiC will be described.

$$\ln\left(\frac{N_G(\theta)}{N_{Al_2O_3}(\theta)}\frac{\rho_{Al_2O_3}}{\rho_G}\frac{\Lambda_e^{Al_2O_3}(E_{C1s})}{\Lambda_e^{G}(E_{C1s})}+1\right)=\frac{t}{\Lambda_e^{G}(E_{C1s})}\frac{1}{\cos\theta} \tag{5.1}$$

$\frac{N_G(\theta)}{N_{Al_2O_3}(\theta)}$ is the ratio of intensity of C1s of graphite and Al2p of Al_2O_3 found out after curve fitting. Molar density of ρ_G and $\rho_{Al_2O_3}$ are given by 0.292 and 0.078 respectively. The values of attenuation lengths $\Lambda_e^{Al_2O_3}$ and Λ_e^{G} are 3.079 and 3.278 respectively.

Fig 5.10 shows a typical curve fitting performed on the C1s spectrum of graphite and the Al2p of Al_2O_3. Since only graphite is grown on sapphire, the relative ratio of the intensities $\frac{N_G(\theta)}{N_{Al_2O_3}(\theta)}$ is the most legitimate way to estimate the thickness of graphite grown. The C 1s region of graphene is fit to an asymmetric line shape described by Doniach and Sunjic [77] and the background is fit according to Shirley [78]. The C1s peak position matches exactly to that of graphite. The asymmetric line shape is a typical feature of all metals and this proves that the graphene grown is metallic. The Al 2p is fit to a symmetric Gaussian-Lorentzian line shape. The ratio $\frac{N_G(\theta)}{N_{Al_2O_3}(\theta)}$ extracted after curve-fitting is fed into Eq 5.1 along with $\theta = 0°$ in order to yield the thickness given as 2.3 Å.

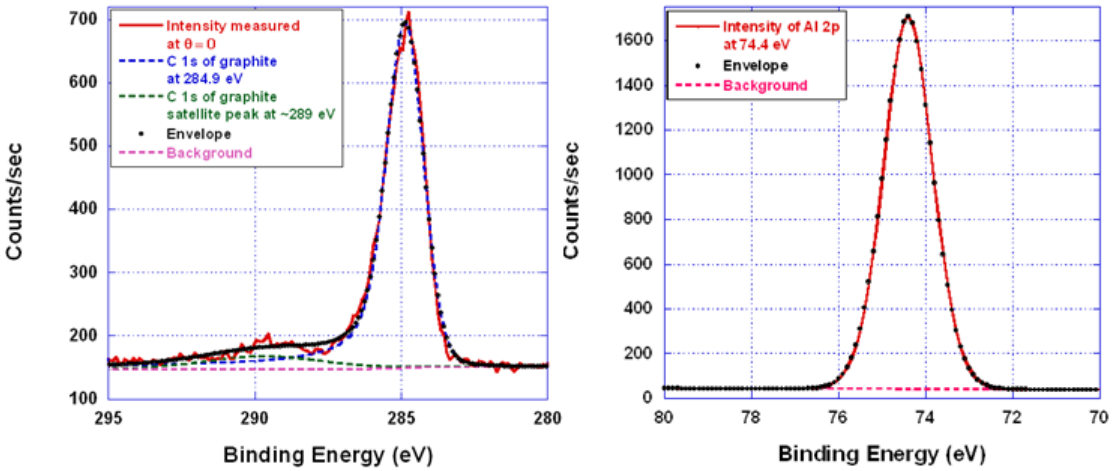

Figure 5.10: LEFT: C1s peak intensity of graphene at 284.9 eV is fit to an asymmetric line shape given by Doniach and Sunjic. A small satellite peak typical of graphitic samples is shown at 289 eV. RIGHT: Al 2p peak at 74.4 eV is fit to a symmteric Gaussian-Lorentzian line shape. The peak intensity ratio C1s/Al2p is used to calculate the thickness of graphene grown as 2.3 Å.

Fig 5.11 shows 2 samples of different thicknesses of graphene. The thickness is evaluated using the same scheme described earlier. Looking at the figure, it can be seen that with increase of thickness of graphene overlayer, the C1s intensity increases and the Al2p intensity drops. Hence, estimating thickness of graphene using $\frac{N_G(\theta)}{N_{Al_2O_3}(\theta)}$ is a legitimate procedure.

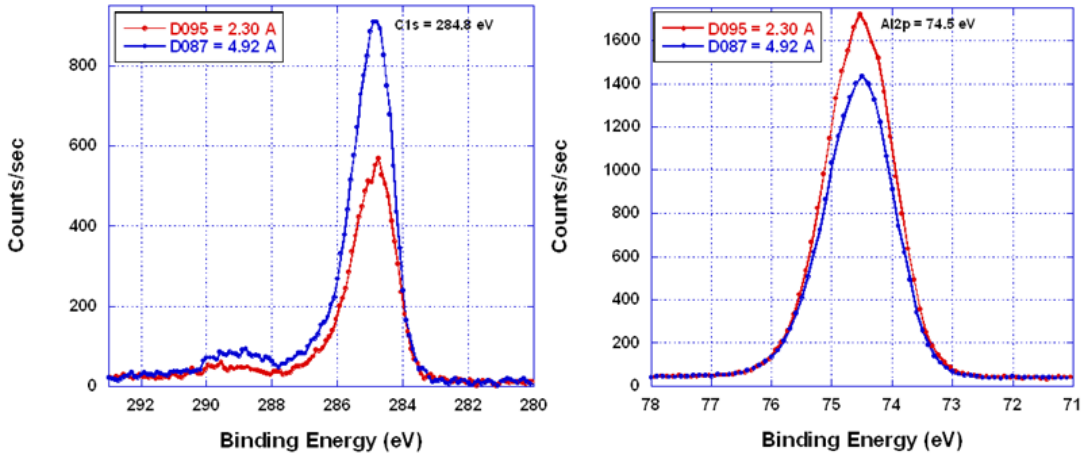

Figure 5.11: LEFT: C1s peak intensity increases with increase of film thickness. RIGHT: Al 2p peak is attenuated with increase of film thickness of graphene.

By varying the thickness of the graphene film grown by MBE on c-plane sap-

phire, a systematic increase in intensity of the C1s signal is seen as shown in Fig 5.12. The estimation of thickness shown in the figure is calculated using the same scheme described above.

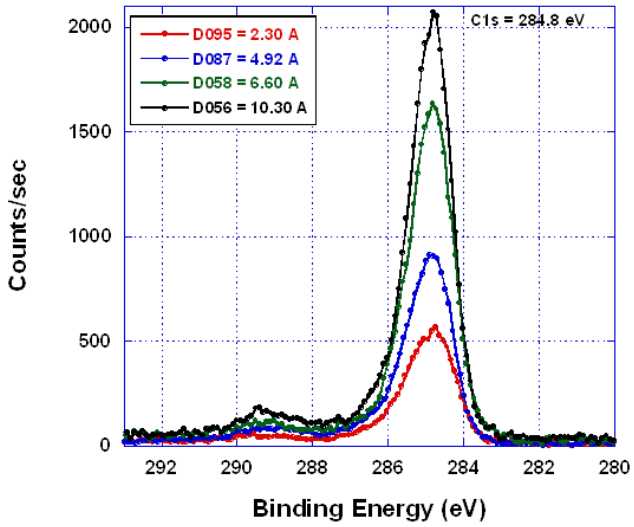

Figure 5.12: Variation of graphitic C1s binding energy peak with thickness. A weak peak at $\sim$ 289 eV is a shake-up satellite peak of the graphitic peak C1s at 284.8 eV.

5.2 Epitaxial graphene growth on 4H SiC (000$\bar{1}$)

Silicon Carbide (SiC) substrates are known to graphitize at temperatures as low as 1150 °C due to sublimation of Si and re-arranging of the the C atoms into a graphene lattice. Since the MBE growths are performed at 1050 °C, it becomes very important to make sure that there is no intrusive graphitization that is happening because of annealing of the substrate before the actual growth is described. Or else, it will be very difficult to understand whether the growth of graphene is due to the deposition of C atoms from the MBE growth or it is intrinsically due to the substrate.

5.2.1 Intrusive Graphitization of 4H SiC (000$\bar{1}$)

In order to verify that no intrusive graphitization takes place, a small experiment is performed where 4H SiC (000$\bar{1}$) substrates used for MBE growths are annealed for different time periods ranging from 3 mins to 360 mins at 1050 °C in the MBE chamber. The sample mounting procedure is described in detail in the next section. Considering the typical growth time to be 90 mins, if it can be shown that no graphitization takes place even for the substrate annealed for 360 minutes (4 times my growth time period), then we can be assured that the graphene growth happens only due to the MBE deposition of C. This will be further confirmed with the help of AFM, XPS and Raman studies. XPS studies show that due to the high temperature used for the growth, the C-C binding energy does decrease indicating that the nature of the C-C bonds change from the sp^3 type to sp^2 type. Hence, through this study, it will be shown that the potential competitive graphitization process does not actually happen and the growth of graphene occurs only due to the MBE growth.

Development of the surface with annealing times from AFM studies

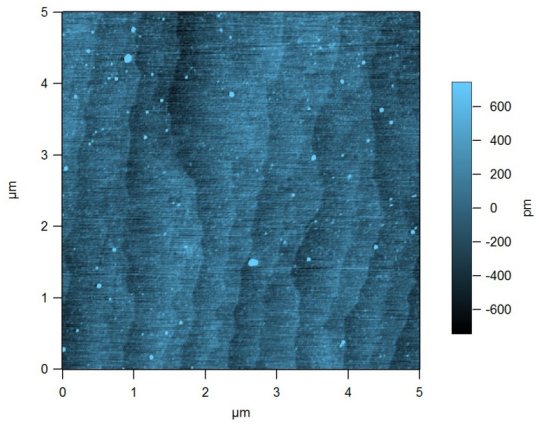

Figure 5.13: Un-annealed 4H-SiC (000$\bar{1}$) substrate after solvent cleaning

Fig 5.13 shows the AFM image of an as-received substrate after solvent cleaning (to be described in the next section). This is the reference AFM scan before the

substrate is annealed at 1050 °C for this study.

Fig 5.14 shows the AFM images of four different samples where the substrate is annealed in the MBE chamber at 1050 °C for 3 mins Fig 5.14 (A), 90 mins Fig 5.14 (B), 180 mins Fig 5.14 (C) and 360 mins Fig 5.14 (D). In comparison to

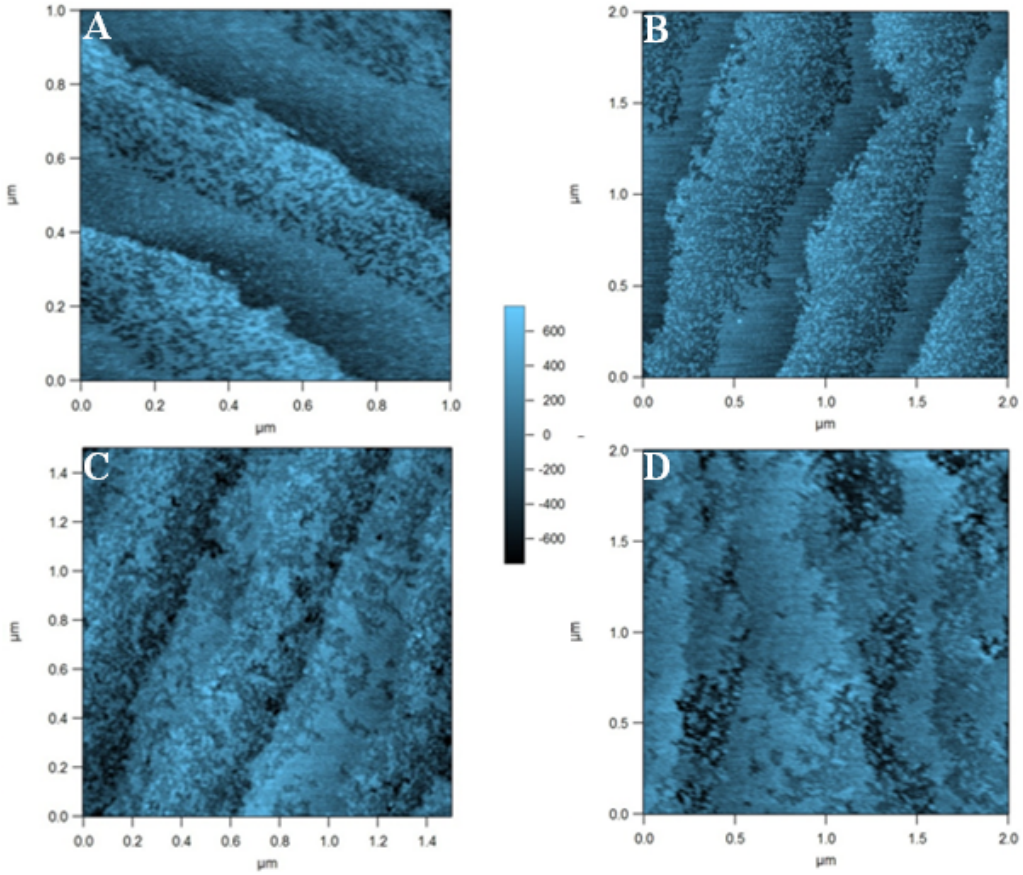

Figure 5.14: AFM images of 4H-SiC $(000\bar{1})$ annealed for different times. (A) for 3 mins, (B) for 90 mins, (C) for 180 mins and (D) for 360 mins

the un-annealed substrate shown in Fig 5.13, just 3 minutes annealing at 1050 °C (Fig 5.14 (A)) results in splitting of each terrace into two parts; rougher part and the smoother part. It should be noted that the rougher part is always towards the edge of the terrace. When annealed longer for 90 minutes (Fig 5.14 (B)), the surface morphology does not change much except that the rougher portion of the terrace has advanced further away from the terrace edge. With annealing the substrate for 180 minutes (Fig 5.14 (C)), the rougher patches have proliferated further and the previously smoother portion of the terrace seen in the 90 minutes

annealed case has a lot of rougher patches. A clear cut demarcation between the smooth and the rough portion of a terrace which could be distinctly seen in the 90 minutes annealed case is no longer distinctly visible in the 180 minutes annealed case. Now, annealing further for 360 mins (Fig 5.14 (D)), we see that the entire width of the terrace looks the same with pits formed mostly towards the edge of each terrace. Thus, the rougher patches in the terrace have grown into pits when annealed for 360 mins.

The researchers who study the growth of graphene via graphitization, also see a similar development of the surface when the surface begins to graphitize. As has been pointed out earlier, sublimation of Si atoms precedes the graphitization of the surface. Since the substrates are annealed at a temperature (1050 °C) high enough for the Si atoms to sublimate, this is definitely a big reason why the roughening of the surface is seen. The fact that we see that one half of the terrace smoother than the other half is explained by the fact that the Si atoms are preferntially desorbed from the terrace closer to the edge. Robinson et al [79] argue that graphene begins to nucleate from the step edges and expands further into the terrace width as the step edges have a higher density of dangling bonds compared to the terraces. Since Si sublimation is responsible for graphitization, the desorption of Si preferentially starts from the step edges compared to the terraces as we see in our case. In our case, we identify the rough patches in the shorter annealed samples as the Si desorbed sites which develop into pits for the 360 minutes annealed case. It can be observed that these pits are mostly pinned at the terrace edge.

Let us concentrate on the 90 minutes annealed case as most of the MBE growths are preceded with a 90 minutes pre-growth annealing step for surface flattening. Fig 5.15 shows the height and phase AFM images of a 90 minute annealed substrate. The height topography shows the clear difference between the Si desorbed portion (closer to the step edge) and the Si undesorbed portion (away from the step edge) of a terrace. This information is also conveyed by the phase topography image where a fairly distinct phase contrast can be seen in every terrace. This

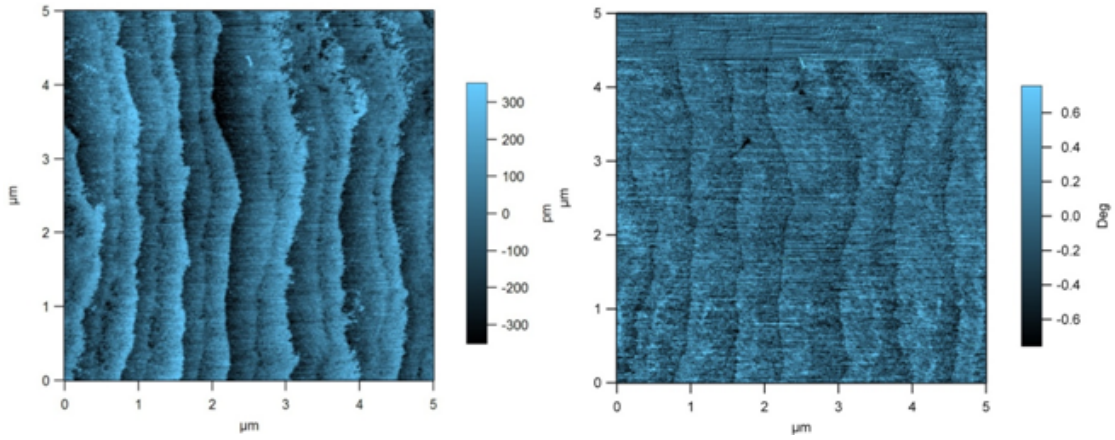

Figure 5.15: 90 minutes annealed 4H SiC $(000\bar{1})$ at 1050 °C. Left: Shows the height topography, Right: Shows the phase topography

implies that 2 different phases have definitely formed on every terrace. Partially graphitized Si terminated SiC [80] and C terminated SiC [21] surfaces also show the presence of two different phases in the phase atomic microscopy scans. But, this faint phase contrast in the right image of Fig 5.15 is seen at almost $\sim$ 200 °C lower than what is claimed by the authors [80, 21]. It will be confirmed with the XPS study later in this section that none of the phases that have formed is of graphitic nature. Hence, the phase contrast that is seen is mostly due to the difference in the chemical composition in each terrace where Si has preferentially desorbed from the portion closer to the step edge. It will be interesting to study the phase AFM when C will be deposited by MBE to grow graphene on such a surface which will be described in detail later in this chapter.

Ferrer et al [21] have developed a model shown in Fig 5.16 in order to explain the phase contrast seen in the AFM images. They analyze the two different phases in the partially graphitized C terminated SiC surface studied by phase AFM. They argue that atomic conservation implies that C atoms from $\sim$ 3 SiC bilayers are required to form one single graphene layer. These C atoms may either come from stacked SiC bilayers resulting in graphene at the bottom of the pits surrounded by SiC bare surface (Model 1 in Fig 5.16), or from one single SiC bilayer resulting in one-third of the surface being covered by graphene above the SiC substrate (Model

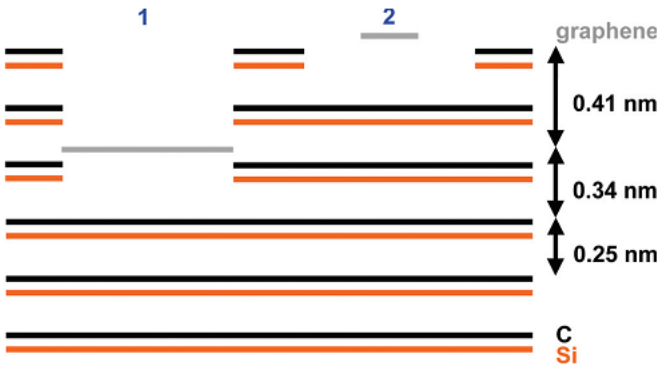

Figure 5.16: Stacking of SiC bilayers along the (0001) direction and graphitization topographical scheme, showing the deep pit with a graphene bottom model (1) and the partially graphitized surface model (2). The distance between 2 SiC bilayers is 0.25 nm and the distance between the graphene overlayer and the SiC surface is 0.09 nm. Courtesy [21]

2 in Fig 5.16). The topographic and phase images should be almost identical in the 1st model because of the full coverage of the pit with graphene. On the contrary, two different sets of materials are seen to be formed in the 2nd model which should show a difference in the phase and height topography. In our case, we believe that although the formation of graphene is ruled out (as will be confirmed by XPS next), the preferntial Si-desorbed regions near the step edge results in the emergence of a new phase which differ from the Si-undesorbed regions. This point will be explained further when we will study the phase AFM microscopy of the MBE grown graphene films on such a surface later in this chapter.

X-Ray Photoelectron Spectroscopy studies

XPS can find the C-C C 1s binding energy of the annealed 4H-SiC $(000\bar{1})$ substrates from which we can deduce how close it is to the C 1s binding energy of a typical graphite sample. We know that in a graphitized sample, C 1s binding energy is $\sim$ 284.8 eV and it is electrically conducting. Now, we need to find out how close is the C 1s binding energy for our 1050 °C annealed samples to graphite. If we can show that the C1s binding energy for the 360 minutes annealed substrate (which has the highest potential to be graphitized) is substantially higher than

284.8 eV, then we can prove that the domains we saw in the AFM images are not graphitic in nature. This would mean that annealing for shorter duration at 1050 °C would definitely not form graphitic domains. This would be a conclusive proof that the C atoms deposited by MBE is solely responsible for the growth of graphene rather than the potential graphitization that can happen at 1050 °C. Since most of our MBE growths involve the 90 minutes pre-growth annealing step at 1050 °C, this XPS study becomes all the more essential to eliminate the possibility of instrusive graphitization.

Fig 5.17 shows the variation in the C 1s binding energy with annealing time (ranging from 3 minutes to 360 minutes). It can be seen that the C-Si binding energy at 283.8 eV is unresponsive to the annealing times. The scans shown have an emission angle of 90 °. It can be seen that the C-C C1s binding energy shifts to

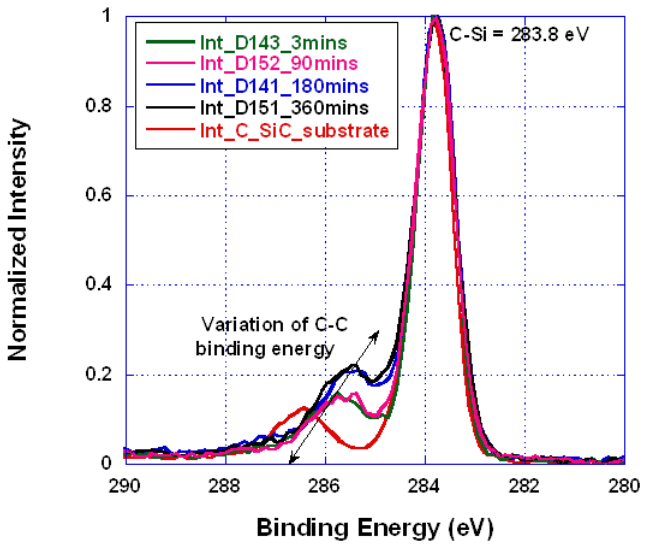

Figure 5.17: Variation of C-C binding energy with variation in annealing times

lower values when the samples are annealed longer at 1050 °C. Muehlhoff et al [81] also show that C 1s binding energy shifts to lower values as the SiC $(000\bar{1})$ surface is annealed with respect to increase in temperatures. But, Si 2p and Si 2s binding energies are independent with respect to increase in the annealing temperatures (not shown here). Muehlhoff et al [81] further claim that the chemical environment of Si remains constant during annealing whereas the chemical environment of C

changes due to the evolution of the bonding nature of the C-C bonds from sp^3 to sp^2 type.

Table 5.1 lists the C1s binding energy for different annealing times. It can be seen even for the 360 mins annealed sample, the C1s binding energy decreases to as low as 285.29 eV; whereas the C1s binding energy for a conducting graphitized sample is $\sim$ 284.8 eV. But, the C-C C1s binding energies reported in Table 5.1 lie somewhere in between being graphitic and being sp^3 hybridized. Hence, we believe that the bonding nature of the C atoms in the domains formed due to annealing are sp^2 hybridized in nature whose binding energy values are closer to what is seen in our case. This rules out the possibility that the formed domains are graphitic.

Table 5.1: Tabulation of the C-C binding energies of the C 1s peak for the corresponding annealing times for the data shown in Fig 5.17 using CASA.

Annealing Time (mins)	C 1s binding energy (eV)
0	286.48
3	285.55
90	285.46
180	285.31
360	285.29

Raman Spectroscopy studies

Raman spectroscopy being the fingerprint of graphene should provide us some insight about the nature of the domains that are formed due to the annealing of the substrates as seen in the AFM images earlier in this chapter. We will concentrate our attention only on the 2D region which is interesting. The D and G regions do not show any conceivable graphene related peaks in the annealed samples and will not be discussed here. This is yet another proof that the domains seen in the AFM images are definitely not graphitic in nature.

Fig 5.18 shows the development of a peak in the 2D region in the Raman scans of all the annealed samples. The peak position is at $\sim$ 2775 cm^{-1} which is almost

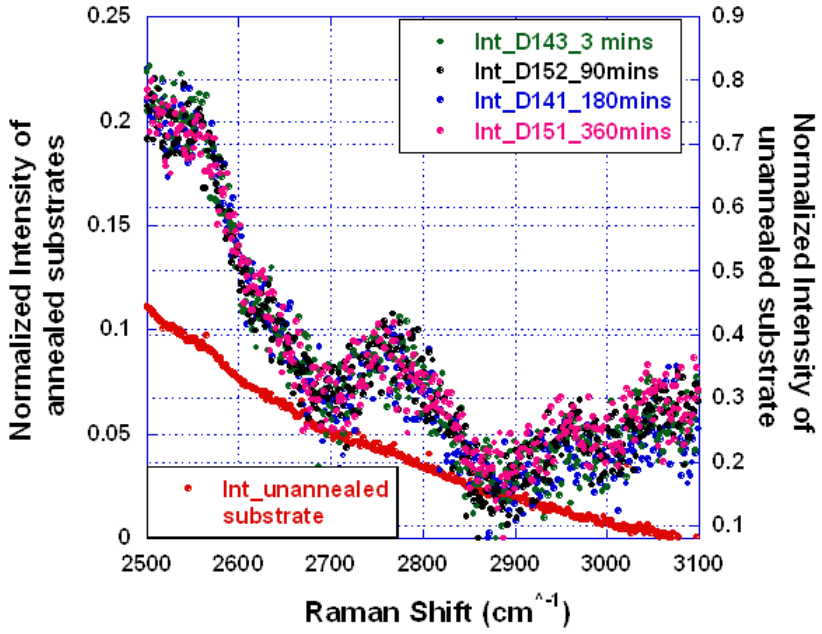

Figure 5.18: The peak in the 2D region that has developed due to annealing at 1050 °C does not change in shape or position for different annealing times.

30 cm^{-1} higher [82] than a typical one monolayer graphene 2D peak probed by 488 nm laser. As explained by the authors [82], the huge upshift of the 2D peak in graphene is an indication that the graphene is under a lot of compressive stress. Hence, we believe these formed domains are also under a lot of compressive stress resulting in this huge upshift of the "supposed" 2D peak. The upshift of the real 2D peak (in the grown films) due to compressive stress will be discussed later in this chapter when the Raman Spectroscopy of the MBE grown graphene films will be described. If these domains are at all graphitic in nature, they should grow in thickness when the samples are annealed longer. But, all the annealed samples starting from 3 minutes through 360 minutes do not show any kind of dispersion of the peak with thickness as is typical of a 2D peak of graphene. This dispersion of the 2D peak will be discussed later in this chapter when the MBE growth of graphene on these substrates will be discussed. But, this kind of a dispersion is is not seen here.

Fig 5.18 also shows the un-annealed as-received sample which does not have any kind of a conceivable peak in the 2D region. This suggests that the electronic

structure of the 4H-SiC $(000\bar{1})$ substrate has definitely changed with annealing. 3 minutes of annealing at 1050 °C is enough for the development of this peak which neither changes in shape or position with further annealing. XPS studies have already confirmed that these domains seen in the AFM scans have too high a C1s binding energy to be called graphitic. The domains formed are disconnected from each other as can be seen in the AFM images as a result of which these annealed samples are electrically insulating.

It should be pointed out here that the X-ray spot size in the XPS scans being $\sim$ 1 mm compared to 10 μm of the laser spot size in the Raman scans, the X-Ray spot size should be able to capture all the graphitic domains if there are any. Because the C1s binding energy (from XPS studies) of the longest (360 minutes) annealed sample is 285.29 eV (C1s of graphite being 284.8 eV), the domains seen in the AFM can be conclusively confirmed to be non-graphitic in nature. The actual growth of graphene by MBE is described next.

5.2.2 Mechanism of the MBE growth of graphene on 4H SiC $(000\bar{1})$

The double side polished 4H SiC $(000\bar{1})$ substrate procured from CREE was back side (on the optically polished side) coated with 5000 Å of Nb by sputter deposition for optical pyrometry. Great care is taken to identify the C terminated side of the double side polished substrate where the optically polished side is scratched by a diamond scribe when removed from the wafer box. The substrate cleaning procedure remains the same as that for the c-plane sapphire described in the previous chapter. The cleaning procedure is applied on the C-terminated side which is the epi-ready side and is identified as the non-scratched side of the wafer. The same kind of an off-axis puck as that for c-plane sapphire is used to mount the substrate which ensures that the highest temperature can be achieved (for a given filament current) on the surface of the substrate although it limits the use of RHEED to just one azimuth. After a 300 °C overnight degasing in order to

remove the water vapor, the substrate is slowly ramped up to 1050 °C the next morning ready to be grown upon.

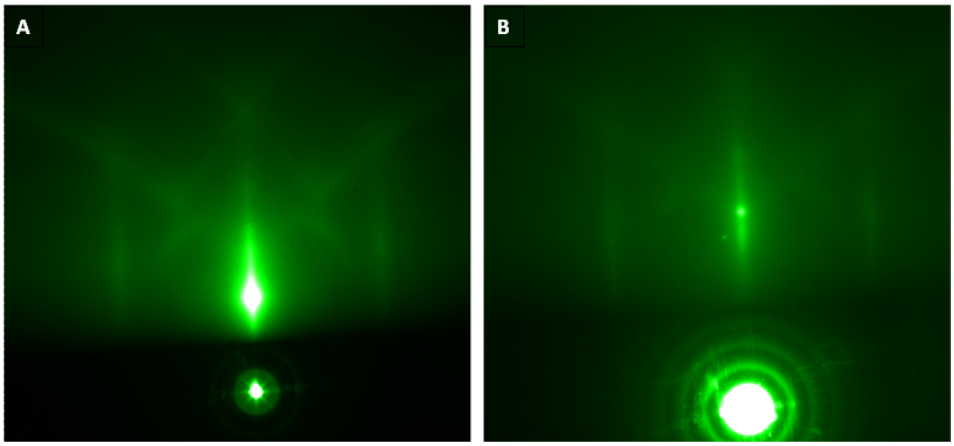

Figure 5.19: (1 × 1)RHEED pattern along the (1-100) azimuth at 1050 °C (A) 4H-SiC (000$\bar{1}$) substrate after 90 minutes of annealing at 1050 °C before the start of growth (B) (1 × 1) RHEED pattern after growing 3 MLs of graphene.

The substrate is annealed at 1050 °C for 90 minutes which is a pre-growth annealing step required for flattening the substrate before the MBE growth of graphene. This annealing step forms a (1 × 1) RHEED pattern along the (1-100) azimuth shown in Fig 5.19 (A) which is the starting surface before the electron gun deposition of Carbon. The annealing of the substrate for different time periods has been studied in detail in the previous section where it has been confirmed that 90 minutes of annealing at 1050 °C does not form graphitized domains on the surface due to Si desorption. However, AFM, Raman and XPS studies do indicate the transformation of the C terminated surface due to the annealing step where the bonding structure of C changes from sp^3 type to sp^2 type. The growths that will be described here last for a maximum of 60 minutes (for the thickest films grown) in addition to the 90 minutes annealing step. But, it has already been shown in the previous section that even a 360 minutes annealing step at 1050 °C does not form any graphitic domains on the surface. So, the C atoms deposited via electron gun deposition is the only source for the formation of graphene on the surface. XPS confirms the growth rate of graphene on SiC to be ∼0.2 Å/min. The growth rate of C is kept almost 10 times slower than that of the growth on

c-plane sapphire as it was difficult to maintain epitaxy at a rate faster than this. The growth pressure in the MBE chamber during the electron gun deposition of carbon is in the upper 10^{-9} range.

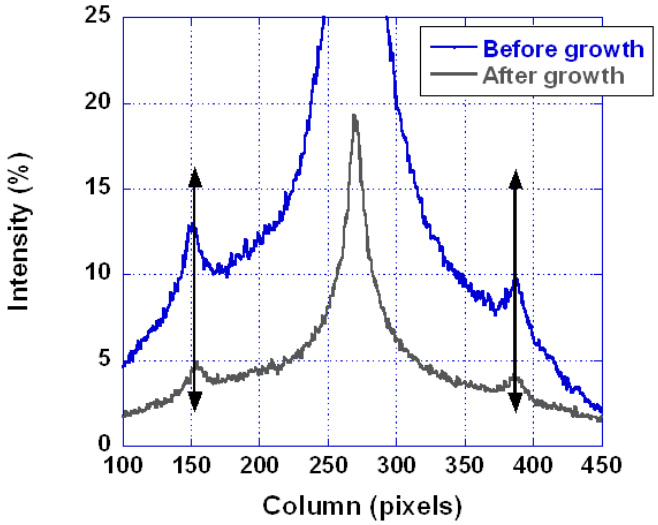

Figure 5.20: Intensity profile showing that the distance between ±1 order diffraction maxima does not change with the growth of 3 MLs of graphene. The intensity profile has been derived from the RHEED images of Fig 5.19. Blue curve shows the intensity profile of the 90 minutes annealed SiC substrate and the grey curve shows the profile after 3 MLs of graphene growth.

Fig 5.19 (B) shows that the (1 × 1) RHEED pattern is intact even after the growth of 3 MLs of graphene although the intensity of the specular spot has diminished. This proves that the growth of graphene just follows the lattice structure of the underlying substrate described by a pseudomorphic growth process. The RHEED intensity profile shown in Fig 5.20 confirms that the distance between the ±1 order maxima in the RHEED pattern does not change even after the growth of 3 MLs of graphene contrary to what is seen in the graphene grown on c-plane sapphire (Fig 5.3). This proves that in spite of the lattice mismatch with the underlying substrate described in Chapter 3, the grown graphene overlayer just confirms to the lattice of the underlying substrate. The growth is described to be pseudomorphic, but it starts in an epitaxial manner. This would mean that the graphene bonds are stretched by as much as the lattice misfit which is $\sim$ 22 %. This is in contrast to what was observed in the c-plane sapphire case in the

previous chapter, where the graphene lattice relaxes with the progression of the growth resulting in the formation of dislocations shown by faceting of the surface. As the growth progresses upto 6 MLs in this case, the epitaxy is lost and rings in the RHEED pattern emerge in addition to the streaks which we term as a "semi-epitaxial" growth and is similar to what is seen in the c-plane sapphire case shown in Fig 5.2. If still grown thicker, the growth becomes completely polycrystalline shown by just diffraction rings in the RHEED pattern.

Thus, contrary to the growth of graphene on c-plane sapphire, RHEED studies confirm that graphene growth on 4H SiC $(000\bar{1})$ starts with the grown overlayer clamped to the substrate and progresses in a layer by layer fashion until epitaxy is lost. No such faceting of the surface formed due to the relaxation of the lattice is seen in this case. Although the grown graphene films on 4H SiC $(000\bar{1})$ substrate will be under tensile stress due to the lattice-mismatch, it will be shown with the help of Raman studies (later in this chapter) that it is the compressive stress due to the mismatch in the coefficient of thermal expansion (CTE) which would play a dominant role over the tensile stress in the films.

5.2.3 Morphology of the graphene films grown

As has been described earlier, the 4H-SiC $(000\bar{1})$ substrate is pre-annealed for 90 minutes at 1050 °C before the MBE growth of graphene. The issue of intrusive graphitization has already been addressed where it has been confirmed that graphitic domains due to Si desorption do not form even when the substrate is annealed for 360 minutes at 1050 °C. A distinct phase contrast is seen in the Phase AFM scans of a 90 minutes annealed substrate as shown in Fig 5.15 (Right). As has been explained earlier, Si preferentially desorbs from the terrace edge compared to the middle portion of the terrace resulting in this phase contrast where the terrace-edge is at a lower phase compared to the rest of the terrace.

It will be interesting to observe how the C overlayer deposited by electron-gun deposition bonds to a Si-desorbed portion (terrace edge) compared to the Si-

undesorbed portion (middle of the terrace). Phase AFM is a very effective way to elucidate this detail. It will be seen that the bonding of the graphene overlayer is different to the Si-desrobed portion compared to the Si-undesorbed portion of the underlying substrate resulting in a very distinct phase contrast. All the samples that will be discussed here are grown on the 90 minutes pre-annealed substrates at 1050 °C with the C deposition rate fixed at ∼0.2 Å/min.

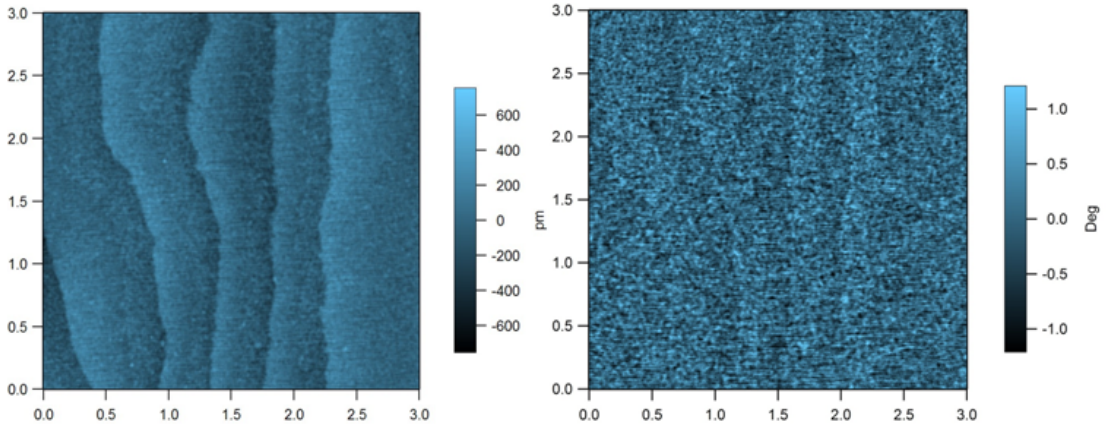

Figure 5.21: LEFT: 3μm Height AFM scan of a $\sim$ 2 ML graphene grown. The grown film is really smooth and completely epitaxial. RIGHT: 3μm Phase AFM scan of the grown graphene film showing a distinct phase contrast.

Fig 5.21 shows a $\sim$ 2 ML graphene film grown on the 90 minutes annealed substrate. The height topography shown in Fig 5.21 (LEFT) depicts a smooth, flat and epitaxial film described by a pseudomorphic growth mode earlier verified by RHEED. Contrary to the growths on c-sapphire, no such faceting of the grown film occurs in the growth on 4H-SiC (000$\bar{1}$) substrate. Fig 5.21 (RIGHT) shows the phase topography of the grown film. Looking carefully at a single terrace, it can be seen that the terrace edge is at a lower phase than that of the rest of the terrace. This Phase image is consistent with the 90 minutes annealed substrate phase image shown in Fig 5.15(Right). Hence, the distinct phase contrast seen in the grown film is a consequence of the starting surface being composed of 2 distinct phases. The phase contrast seen here is much more distinct than what has been seen in the 90 minutes annealed case (Fig 5.15(Right)). Hence, it can be concluded that graphene of two different phases alternate with each other all

over the wafer forming a "lateral superlattice" of these two phases.

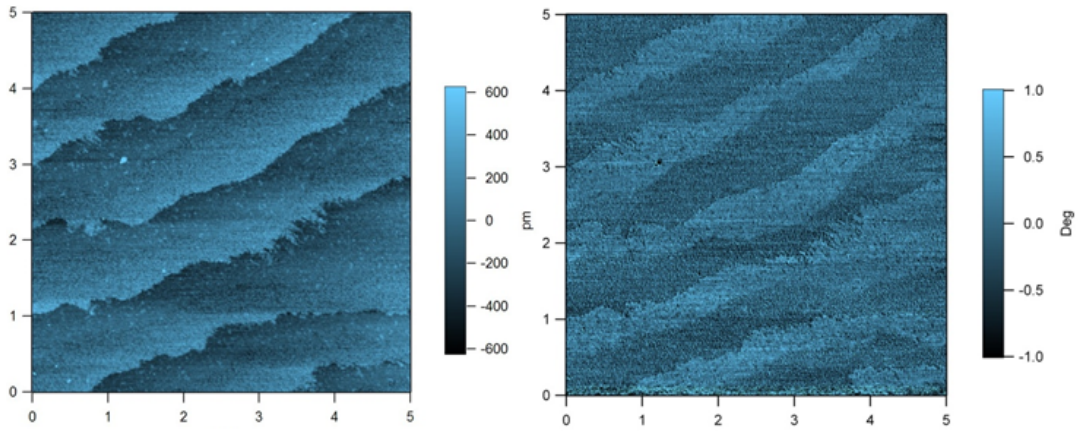

Figure 5.22: LEFT: 5μm Height AFM scan of a $\sim$ 3 ML graphene grown. The grown film is still considerably smooth and epitaxial. RIGHT: 5μm Phase AFM scan of the graphene film where the phase contrast is much more pronounced.

With the deposition of $\sim$ 3MLs of graphene on the 90 minutes pre-growth annealed substrate, the phase contrast shown in Fig 5.22 (RIGHT) has become much more pronounced. The height topography scan shown in Fig 5.22 (LEFT) shows a very smooth and flat surface with a very slight hint of granularity setting in. But, the growth is still epitaxial confirmed by nice streaky RHEED shown in Fig 5.19(B). Carefully looking at the phase AFM scan in Fig 5.22 (RIGHT), it can be seen that the terrace edge is at a phase lower than the rest of the terrace. This phase sequence is the same as that of $\sim$ 2 ML film shown in Fig 5.21 (RIGHT) and the 90 minutes annealed substrate shown in Fig 5.15 (Right). So, the phase sequence seen in $\sim$ 3 ML graphene grown confirms exactly to that of the annealed substrate.

When grown thicker upto $\sim$ 4 MLs, the phase contrast is still intact as shown in Fig 5.23(RIGHT). But, granularity has already emerged as seen in the Height AFM scan shown in Fig 5.23(LEFT). This is an example of a "semi-epitaxial" film composed of both granular and flatter domains. The RHEED image of such a film is a superposition of both streaks (confirming the epitaxial nature) and rings (confirming that polycrystallinity has started to set in) similar to what is shown in Fig 5.2. A closer look at the Phase AFM scan shown in Fig 5.23(RIGHT) depicts

that in a particular terrace, the terrace edge is at a higher phase compared to the rest of the terrace. This is in stark contrast to what has been seen in the 90 minutes annealed case shown in Fig 5.15 (Right), $\sim$ 2 ML case shown in Fig 5.21 (RIGHT) and $\sim$ 3 ML case shown in Fig 5.22 (RIGHT) where the terrace edge is at a higher phase compared to the rest of the terrace. This semi-epitaxial phase of the growth lasts for a couple more MLs (not shown here). But, if grown thicker than 6 MLs, the film becomes completely polycrystalline and the phase contrast is completely washed out (not shown here).

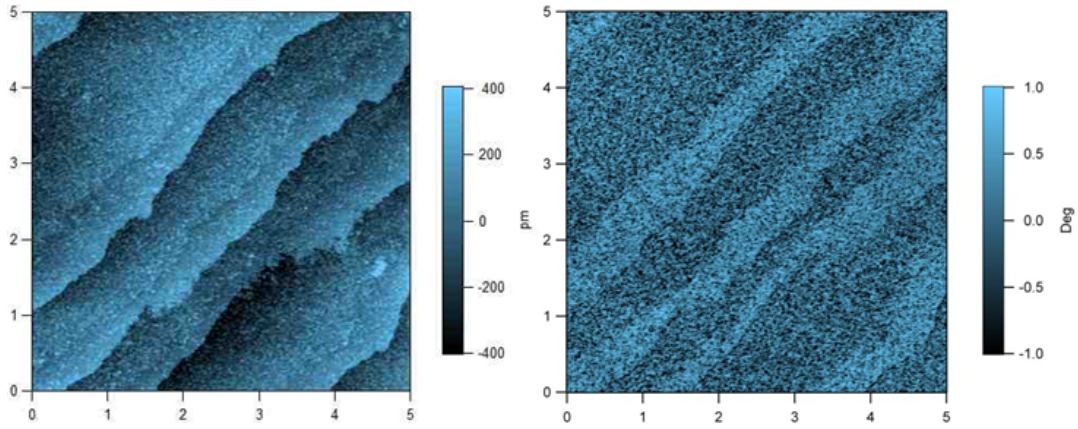

Figure 5.23: LEFT: 5μm Height AFM scan of a $\sim$ 4 ML graphene grown. The surface of the film looks granular although the terraces due to the substrate can be distinctly seen. The RHEED of this film shows a superposition of both rings and streaks. RIGHT: 5μm Phase AFM scan of the graphene film shows the distinct phase contrast. The phase contrast washes out for films $>$ 6 MLs.

Thus, contrary to the graphene films grown on c-plane sapphire, the graphene films grown on 4H-SiC (000$\bar{1}$) is very conformal to the underlying substrate. The phase-contrast which is due to the difference in the Si concentration of the substrate is seen in the graphene films grown and washes out with increase of thickness as the growth becomes completely polycrystalline.

5.2.4 Estimation of thickness from XPS studies

In order to find out the thickness of the MBE grown graphene, the approach used by Fadley [83] is used. The graphene-SiC sample can be modeled as a semi-infinite

SiC substrate with a uniform graphene overlayer of thickness t; where t can be calculated from the ratio between the C1s peak intensities of graphene and SiC. For the very thin film samples, Angle Resolved XPS (ARXPS) has been used in order to accurately estimate the thickness. The thickness of the rest of the samples have been estimated keeping the emission angle at $\theta = 90°$.

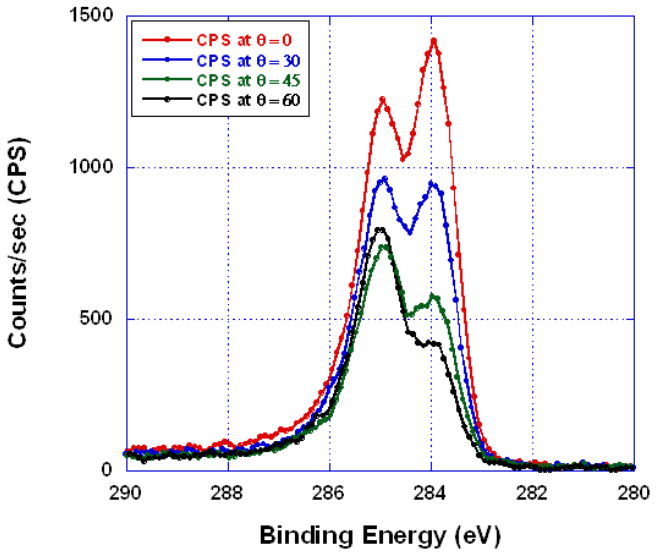

Figure 5.24: ARXPS study done on a 3 ML graphene sample. The angle measured is with respect to the surface normal. It can be seen the signal is maximum when the detector is directly above the sample at $\theta = 0°$

A typical angle resolved spectra where the angle of the detector is measured with respect to the surface normal of the sample (called as emission angle) is shown in Fig 5.24. ARXPS has been acquired for all very-thin film samples for the accurate determination of their thickness. It can be seen that the strength of the C1s signal decreases with increase of the emission angle thus implying that the photoelectrons are collected from the layers very close to the surface. Higher the emission angle, the more surface sensitive it is. This has been discussed under the XPS section of Chapter 4.

The total intensity of the C1s component of the SiC substrate ($\sim$ 283 eV), $N_{SiC}(\theta)$ with a graphene overlayer of thickness t can be written as :

$$N_{SiC}(\theta) = I_o F\left(E_{C1s}\right) \rho_{SiC} \frac{d\sigma_{C1s}}{d\Omega} \Lambda_e^{SiC}\left(E_{C1s}\right) \cos\theta exp\left(\frac{-t}{\Lambda_e^G(E_{C1s})\cos\theta}\right) \quad (5.2)$$

And the total intensity of C1s peak ($\sim$ 284.8 eV) from the graphene overlayer, $N_G(\theta)$ is given as follows :

$$N_G(\theta) = I_o F\left(E_{C1s}\right) \rho_G \frac{d\sigma_{C1s}}{d\Omega} \Lambda_e^G\left(E_{C1s}\right) \cos\theta \left[1 - exp\left(\frac{-t}{\Lambda_e^G(E_{C1s})\cos\theta}\right)\right] \quad (5.3)$$

In the equations Eqn 5.2 and Eqn 5.3, I_o is the X-ray flux and $F(E_{C1s})$ is the spectrometer and electron analyzer dependent parameter which depends on the kinetic energy of the photoelectrons E_{C1s} and includes the acceptance solid angle of the electron analyzer, the effective specimen area and the instrument detection efficiency. ρ_{SiC} and ρ_G are the molar densities of carbon atoms in SiC and graphene respectively. $\frac{d\sigma_{C1s}}{d\Omega}$ is the differential cross-section for the C1s subshell. Λ_e^{SiC} and Λ_e^G are the attenuation lengths for the C1s photoelectron with kinetic energy E_{C1s}.

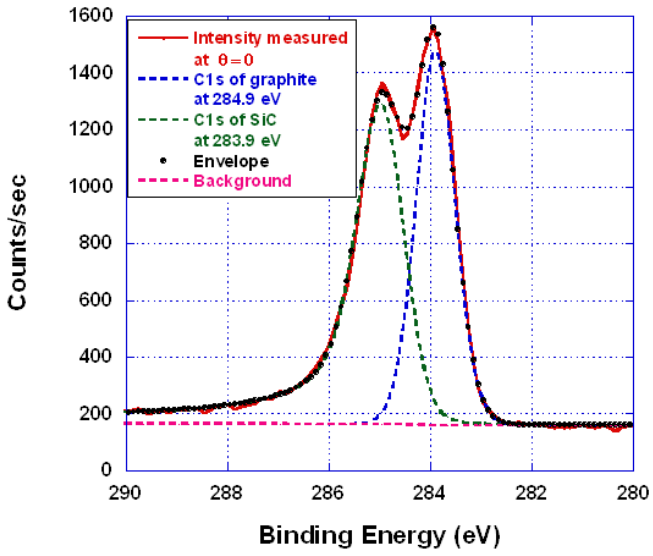

Figure 5.25: A typical curve fitting is done at $\theta = 0°$. The curve fitting results in two peaks located at 284.9 eV for the graphitic C1s and at 283.9 eV for the C1s of SiC. This same procedure is done on all the angle-resolved data.

The C1s spectra shown in Fig 5.25 is collected at $\theta = 0°$. The intensities of graphene and SiC peaks were determined by fitting the C1s using a Shirley [78] background. Following the fitting scheme described by Unarunotai et al [84], the contributions of $N_G(\theta)$ and $N_{SiC}(\theta)$ are found out after carefully fitting the SiC

contribution to a Gaussian-Lorentzian line shape and the graphene contribution to a Doniach-Sunjic line shape [77]. The Doniach-Sunjic line shape is asymmetric and is found out after fitting the C1s spectra of Highly Oriented Pyrolytic Graphite. A fit to an asymmetric line-shape is a clear proof that the grown graphene is metallic. Although the curve fitting is shown only for $\theta = 0°$, all the angle resolved spectra are fit in a similar fashion in order to extract the ratio $\frac{N_G(\theta)}{N_{SiC}(\theta)}$.

The analytical ratio $\frac{N_G(\theta)}{N_{SiC}(\theta)}$ where the spectrometer related parameters cancel is calculated by taking the ratio of Eqn 5.2 and Eqn 5.3.

$$\frac{N_G(\theta)}{N_{SiC}(\theta)} = \frac{\rho_G \Lambda_e^G\left(E_{C1s}\right)\left[1 - exp\left(\frac{-t}{\Lambda_e^G(E_{C1s})\cos\theta}\right)\right]}{\rho_{SiC}\Lambda_e^{SiC}\left(E_{C1s}\right) exp\left(\frac{-t}{\Lambda_e^G(E_{C1s})\cos\theta}\right)} \tag{5.4}$$

The attenuation lengths Λ_e^{SiC} and Λ_e^G are given as 2.59 nm and 3.079 nm respectively. They were calculated using the NIST SRD-82 [85]. The molar densities are given as $\rho_{SiC} = 0.08$ and $\rho_G = 0.292$.

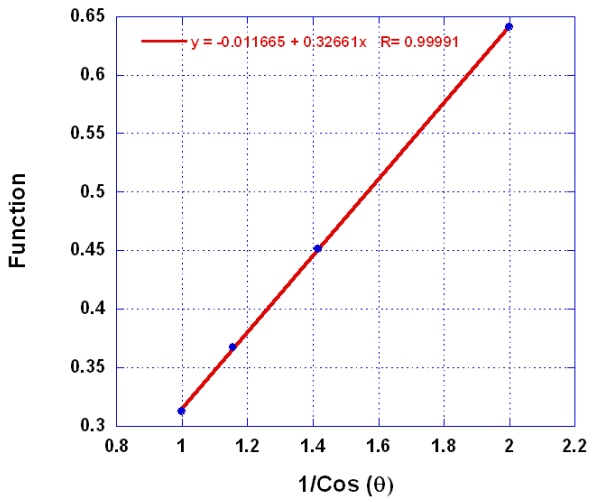

Figure 5.26: The function described in the text is plotted with respect to $\frac{1}{\cos\theta}$; the slope of which gives the thickness of the grown graphene film as 10.06 Å.

$\frac{N_G(\theta)}{N_{SiC}(\theta)}$ was measured (after curve fitting) for each of the 4 photoemission angles (in our case). Eq 5.4 can be rearranged as follows :

$$\ln\left(\frac{N_G(\theta)}{N_{SiC}(\theta)}\frac{\rho_{SiC}}{\rho_G}\frac{\Lambda_e^{SiC}\left(E_{C1s}\right)}{\Lambda_e^G\left(E_{C1s}\right)} + 1\right) = \frac{t}{\Lambda_e^G\left(E_{C1s}\right)}\frac{1}{\cos\theta} \tag{5.5}$$

The Function, $\ln\left(\frac{N_G(\theta)}{N_{SiC}(\theta)}\frac{\rho_{SiC}}{\rho_G}\frac{\Lambda_e^{SiC}(E_{C1s})}{\Lambda_e^G(E_{C1s})}+1\right)$ is shown to be plotted vs $\frac{1}{\cos\theta}$ in Fig 5.26. The slope of the linear fit of the curve multiplied by $\Lambda_e^G(E_{C1s})$ gives the thickness t.

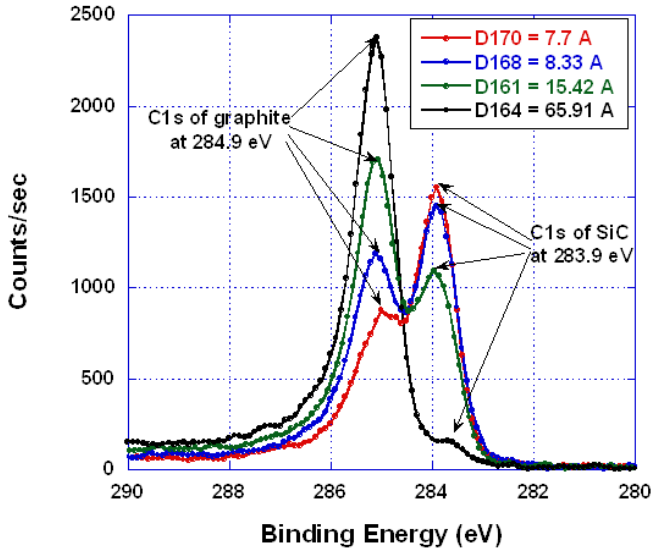

Figure 5.27: The figure shows the spectrum collected at $\theta = 0°$ where the intensity of C1s of graphite increases with increase of graphene film thickness whereas the intensity of C1s of SiC is attenuated.

As stated earlier, Angle Resolved XPS is used to estimate the thickness for the potential very thin samples. The emission angle, $\theta = 0°$ where the signal strength is the highest is used to calculate the thickness of all the other samples. The C1s spectra are fit according to the scheme described earlier in order to yield $\frac{N_G(\theta)}{N_{SiC}(\theta)}$ which is put in Eq 5.5 along with $\theta = 0°$ in order to estimate the thickness. Fig 5.27 shows the C1s spectra for grown graphene films of varying thickness. It can be seen that with increase of thickness, the C1s of graphene signal increases whereas C1s of SiC is attenuated. This is the reason why XPS is a self-calibrating technique used to accurately measure the thickness of graphene grown on SiC.

5.3 Conclusion

The major differences of growing graphene on the two hexagonal substrates: c-plane sapphire and 4H-SiC $(000\bar{1})$ are as follows :

- RHEED studies show a different registry of graphene on these two substrates. On c-plane sapphire, the graphene lattice relaxes with the progression of the growth whereas on 4H-SiC $(000\bar{1})$, the graphene lattice is clamped to the substrate as the growth progresses. The relaxation of the graphene lattice in the c-plane sapphire case causes dislocations studied by AFM.

- RHEED studies in both cases show that the growth starts in an epitaxial manner, progresses to become semi-epitaxial (both streaks and rings) and then ultimately becomes polycrystalline (only rings) when grown higher in thickness.

- AFM images show that the surface of the thin epitaxial graphene film ruptures into facets which are hexagonal in nature on c-plane sapphire. These are the form of dislocations that occur as the graphene lattice relaxes with the progression of the growth. Although the AFM study estimates an unfaceted graphene domain size as $\sim 1\mu m$, Raman studies (to be studied in the next chapter) would confirm that the actual graphene domain size is less than 10 nm. Whereas, the graphene films grown on 4H-SiC $(000\bar{1})$ do not show any faceting of the surface and is very conformal to the underlying substrate yielding higher graphene crystallite domain sizes (to be described in the next chapter with the help of Raman studies). This particular difference between the morphology of the graphene films on these two substrates also shows up in the low temperature transport to be studied in Chapter 7.

- XPS studies are done in order to estimate the thickness of the MBE grown graphene films. It further confirms that the grown graphene film on both the substrates are indeed graphitic in nature from the asymmetric shape of the C1s peak and its peak position. In addition to this, XPS study rules out the possibility that there is no graphene formation due to graphitization of the substrate at 1050 °C which is the growth temperature.

CHAPTER 6

RAMAN STUDIES OF THE GROWN GRAPHENE FILMS

Raman spectroscopy being the finger print of graphene is used to study the MBE grown films on c-plane sapphire and 4H SiC $(000\bar{1})$. The finer details of a typical graphene Raman spectrum have already been described in Chapter 4 where the details of the Raman setup used have also been discussed. As has already been discussed in the previous chapter, with increase of thickness epitaxy of the graphene film with the underlying substrate is progressively lost resulting in a polycrystalline growth. The in-plane coherence length of the graphene crystalline order is estimated in the MBE grown films from the intensity ratios of D and G peaks. The split G peak in the graphene Raman spectrum of the growths on c-plane sapphire implies tensile stress whereas the huge upshift of the 2D peak in the Raman spectrum of films grown on 4H SiC $(000\bar{1})$ implies compressive stress in the grown films. It will be shown further that the symmetric nature of the 2D peak in the Raman spectrum of the multi-layer graphene films grown on both the substrates implies loss of **AB** stacking order.

In this chapter, it will be shown that although the Raman spectrum of graphene grown on c-plane sapphire is devoid of any substrate peaks, the typical Raman peaks of graphene grown on 4H SiC $(000\bar{1})$ is embedded in the intense SiC substrate peaks. Hence, a very careful subtraction procedure will be presented which becomes crucial in the extraction of the typical graphene Raman peaks.

6.1 Graphene films grown on c-plane sapphire

The typical Raman spectrum of graphene grown on c-plane sapphire is devoid of any intense sapphire substrate peaks unlike in the case of graphene grown on 4H SiC $(000\bar{1})$. Although all the films grown on c-plane sapphire have a similar Raman spectrum, 3 representative samples grown exactly under the same conditions (growth temperature = 1050 °C and growth rate of C = 0.1 Å/s) but with varying thicknesses will be discussed here.

6.1.1 Raman studies of graphene films of varying thickness: Estimation of graphene crystallite domain size

The Raman spectrum of graphene films grown on c-plane sapphire varying with thickness will be discussed. Sample D171 is completely epitaxial with a flat morphology similar to what is seen in Fig 5.6(RIGHT). Sample D173 is in the semi-epitaxial regime (RHEED shows superposition of both streaks and rings) and has a surface consisting of both granular and flat domains. Sample D172 being the thickest is polycrystalline with a granular surface morphology.

Fig 6.1 shows the Raman spectrum with all the typical peaks of graphene present. The D peak at 1338 cm^{-1} associated with the defect peak of graphene is a non-resonant process which occurs due to the presence of zone boundary phonons near the K zone boundary shown in Fig 4.5(c). It can be seen that the position of D mode is insensitive to thickness. The D+G peak at 2925 cm^{-1} seen in Fig 6.1 is also the signature of presence of disorder in graphene. This peak is also non-dispersive with respect to thickness of the graphene overlayer and is also a characteristic feature of disordered graphene. The main reason for the presence of the disorder induced D and D+G peaks in the spectrum is the tensile stress due to the lattice mismatch of graphene with c-plane sapphire which results in faceting of the surface even for the thinnest flat epitaxial grown graphene. The evidence of this has already been discussed in the AFM study where the first 3

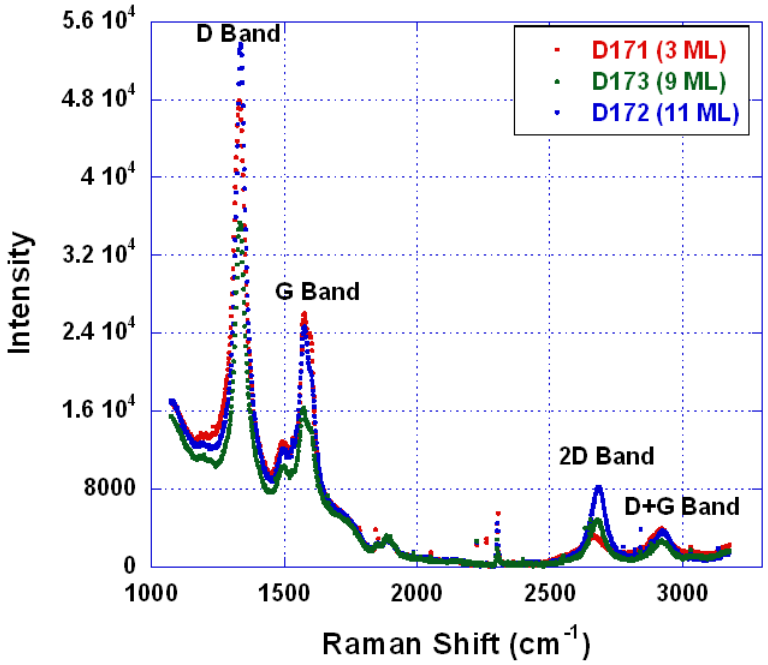

Figure 6.1: Raman spectrum of 3 different thicknesses of graphene film grown under the same conditions on c-plane sapphire. The spectrum has all the typical peaks of graphene.

MLs grown are so strained to the substrate that the films ruptures into hexagonal facets shown in Fig 5.7. This creates a lot of grain boundaries in an otherwise flat epitaxial graphene film grown. With increase of thickness, epitaxy is lost resulting in a granular morphology for thicker films. Hence, the grain boundaries responsible for the zone-boundary phonons of the D peak are always present in the graphene film irrespective of how flat the film is.

The G peak occurs at 1576 cm^{-1} with a shoulder like feature developed at 1603 cm^{-1} which is a disorder induced feature. As discussed in Chapter 4, the G mode which occurs due to an off-resonant process (far from the $\mathbf{K}$ and $\mathbf{K}'$ points) is the signature of any sp^2 C network and is a one phonon process involving $\mathbf{\Gamma}$ point optical phonon. The G mode is non-dispersive with respect to thickness. Looking closely at Fig 6.1, $\frac{I(D)}{I(G)}$ is found for each thickness of the graphene film grown. The size of the crystallite domains is obtained from Eq 6.1 [72]

$$L_a(nm) = (2.4 \times 10^{-10})\lambda_l^4 \left(\frac{I(D)}{I(G)}\right)^{-1} \tag{6.1}$$

where λ_l is the laser wavelength in nm and L_a is the size of the crystal domain or in-plane correlation length. Plugging in the value of $\frac{I(D)}{I(G)}$ in Eq 6.1, the crystallite domain size (the in-plane coherence length of the graphene crystalline order) is estimated. Table 6.1 lists the graphene crystallite domain sizes. Thus, it can be seen that with increase of thickness as the epitaxy of the graphene film with the underlying substrate is progressively lost, it results in increase of the grain boundaries as a result of which the crystallite domain size decreases. It can be seen that the crystallite domain size is less than 10 nm. It will be shown in the next section that graphene films grown on 4H SiC $(000\bar{1})$ have much bigger crystallite domain sizes. This particular difference in the in-plane coherence length of the two classes of graphene films grown shows up in the temperature dependent sheet resistance to be studied in the next chapter.

Table 6.1: Tabulation of the graphene crystallite domain size of the films shown in Fig 6.1.

Sample	ML	$\frac{I(D)}{I(G)}$	$L_a(nm)$
D171	3	2.04	6.7
D173	9	2.60	5.2
D172	11	2.71	5.0

6.1.2 Dispersion of 2D peak with thickness

The 2D band located at 2683 cm^{-1} is a second order Raman mode and occurs due to a fully resonant process between the inequivalent **K** and **K**$'$ points. This mode is dispersive with respect to thickness as shown in Fig 6.2. Ferrari et al [17] have shown that in case of exfoliated graphene the 2D peak not only disperses with increase of number of layers but also changes its shape. According to Ferrari, the shape of the 2D peak of a single layer exfoliated graphene can be fit to a single lorentzian whereas for a bilayer graphene can be fit to four lorentzians. As has already been described in detail in Chapter 4, the interaction of the graphene planes in the bilayer case causes the π and π^* bands to divide into four. The

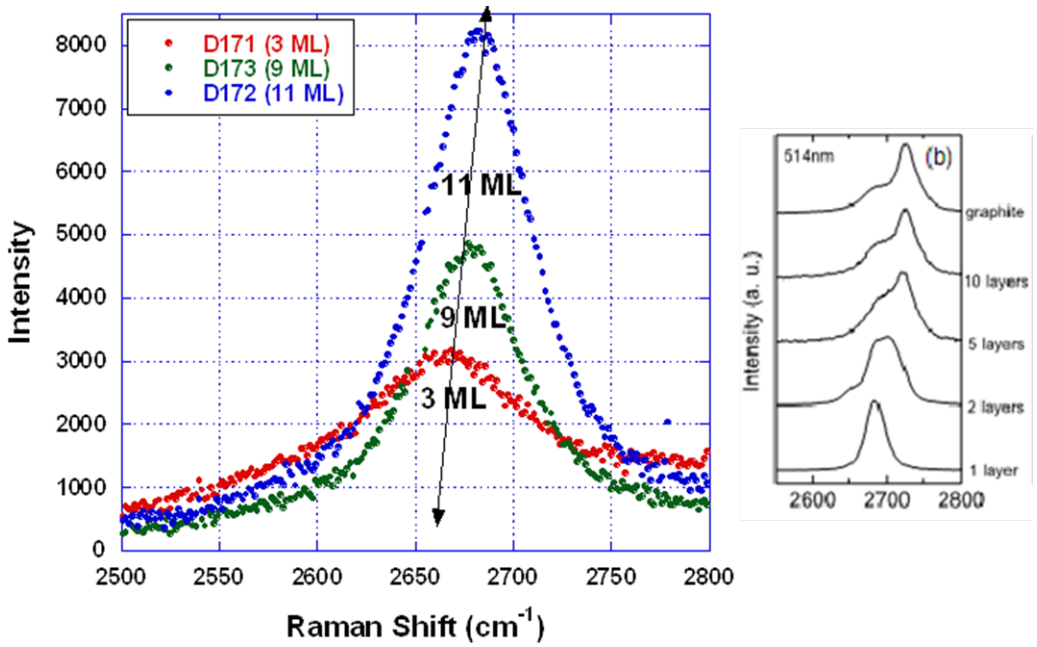

Figure 6.2: 2D peak of graphene disperses with increase of thickness of graphene overlayer grown. The Raman spectrum has been acquired with a 488 nm laser. The 2D peak shifts to higher wavenumbers with increase of thickness consistent with exfoliated graphene [17] shown in the right of the figure.

change of shape of the 2D peak is shown in the right half of Fig 6.2. But, in our case of MBE grown graphene, the shape of the 2D peak does not change from the single lorentzian shape with increase of layer number. This has also been seen in multi-layer graphene grown by graphitization of SiC on the C face [52, 69] where the **AB** stacking of graphene layers is not preserved. This is also a characteristic feature of turbostatic graphite. Since the stacking sequence becomes random departing from the **AB** stacking sequence, each layer is electronically decoupled from the layer beneath or above it. The data shown in Fig 6.2 shows the 2D peak whose shape does not change with increase of thickness of graphene grown and can be fit to a single lorentzian as in the case of monolayer graphene of the exfoliated case. Following the symmetric nature of the 2D peak irrespective of the thickness, we believe that the stacking sequence in our MBE grown graphene is also random as has been seen in the graphitized 4H-SiC $(000\bar{1})$ case. Hence, the monolayer character of graphene is preserved even in the multilayer case. Consistent with

the exfoliated graphene case, the 2D peak disperses to higher wavenumbers with increase of thickness of grown graphene overlayer.

Another important observation is the position of the 2D peak lying in the range: 2660 cm^{-1} to 2680 cm^{-1} for the initial few MLs of graphene grown. Contrary to this, the graphene grown on 4H SiC $(000\bar{1})$ (to be described next) has the 2D peak in the range: 2720 cm^{-1} to 2760 cm^{-1} for the first few MLs graphene grown. The high upshift in case of SiC is because of the presence of compressive stress in the initial few MLs grown due to the mismatch of co-efficient of thermal expansion (CTE) of graphene with SiC (CTE of graphene lesser than that of SiC). This issue will be analyzed in detail in Raman studies of graphene on 4H SiC $(000\bar{1})$ next. But, this CTE mismatch in case of sapphire (CTE of graphene is lesser than that of sapphire) is double to that of SiC. But, no such upshift of the 2D peak is observed in case of graphene grown on c-plane sapphire. This is because of the minimal interaction of graphene with the underlying sapphire substrate contrary to the case of graphene grown on 4H SiC $(000\bar{1})$. Since the graphene grown on c-plane sapphire is not as clamped to the underlying substrate as in the case of SiC, the CTE mismatch is not as big an issue here. The graphene films grown on c-plane sapphire are only under tensile stress due to the mismatch in the lattice constant with the underlying substrate as will be described next.

6.1.3 Evidence of tensile stress

The issue of epitaxy of graphene with c-plane sapphire has already been analyzed in detail Chapter 3. Following the RHEED analysis in the last chapter, we have seen that the alignment of the graphene lattice on c-plane sapphire is non-trivial resulting in a 12% lattice mismatch. In spite of this lattice mismatch, epitaxy is maintained for the initial few MLs of graphene grown as shown in the RHEED studies. But, the consequence of the lattice mismatch shows up in the AFM study where the 3 ML graphene film is seen to have developed into hexagonal facets. The faceting of the surface are due to the misfit dislocations occurring as the grown

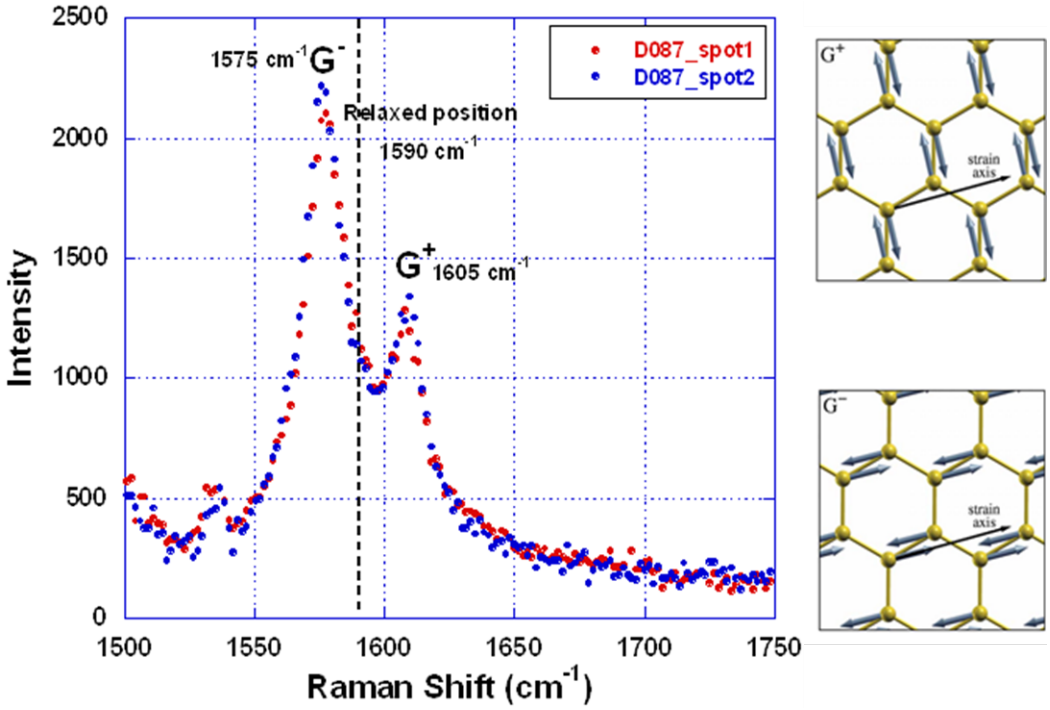

Figure 6.3: The G peak splits to G^+ and G^- which is the signature of the presence of tensile stress in the first few MLs of graphene grown. The vibration modes associated with G^+ and G^- are shown in the right half of the figure taken from [22]. The sample D087 shown is a 1.5 ML graphene grown on c-plane sapphire.

graphene layer relaxes with the progression of the growth. The presence of tensile stress at the beginning of the growth is further proved by Raman spectroscopy where a 1.5 ML graphene film shows a very prominent split in the G band into G^+ at 1605 cm^{-1} and G^- at 1575 cm^{-1} shown in Fig 6.3.

Mohiuddin et al [22] have also shown a similar splitting of G band by applying uniaxial strain on exfoliated graphene flakes deposited on flexible substrates in a two-point and four-point bending setups. As a result of the application of strain, the doubly degenerate G band splits into two modes : G^- polarized in the direction of strain axis and G^+ polarized in the direction perpendicular to the strain axis. But, in our case the splitting of the G band is due to the tensile strain induced by the lattice mismatch. Purposefully, a 1.5 ML graphene film (sample D087) which is electrically insulating is studied where the split is the most pronounced. With the increase of thickness, the film tends to relax from the strain and the distinct

split is no longer seen in thicker films (as shown in Fig 6.1). This split develops into a shoulder like feature in the G band as shown in Fig 6.1.

Thus Raman spectroscopy provides sufficient evidence that the first few MLs of graphene grown on c-plane sapphire are under tensile stress (due to the mismatch in the lattice constant of graphene with c-plane sapphire) rather than under compressive stress (due to the mismatch in the coefficient of thermal expansion (CTE) of graphene with c-plane sapphire). Raman studies conclusively proves that due to the minimal interaction of graphene with the underlying substrate, mismatch in the lattice-constant takes precedence over the CTE mismatch resulting in a dominance of tensile stress over compressive stress in the grown films.

6.2 Graphene films grown on 4H SiC (000$\bar{1}$)

As has already been discussed briefly in Chapter 4, performing Raman spectroscopy studies on graphene grown on SiC substrates is not very trivial. In the case of graphene grown on c-plane sapphire, we were never had to worry about subtracting the signal of the substrate to reproduce the signal from the graphene film. But, in the case of graphene grown on SiC, the substrate signal interferes with the typical graphene Raman peaks. A very careful subtraction procedure will be presented which elaborates how the typical graphene peaks are extracted. All the samples discussed in this section have been grown under the same conditions (C growth rate = 1 Å/min and the substrate temperature = 1050 °C).

6.2.1 Extraction of D and G peaks : Estimation of the graphene crystallite domain size

As is shown in Fig 6.4, except for the 2D peak, G and D peaks lie exactly in the position of the intense substrate peaks as shown in Fig 6.4. Hence, a very careful subtraction procedure has to be performed in order to extract the typical graphene peaks (D and G). Since the ratio of intensities of D and G peaks gives the information about the size of the graphitic domains in the grown films, the

extraction procedure followed by a meticulous curve fitting become all the more important.

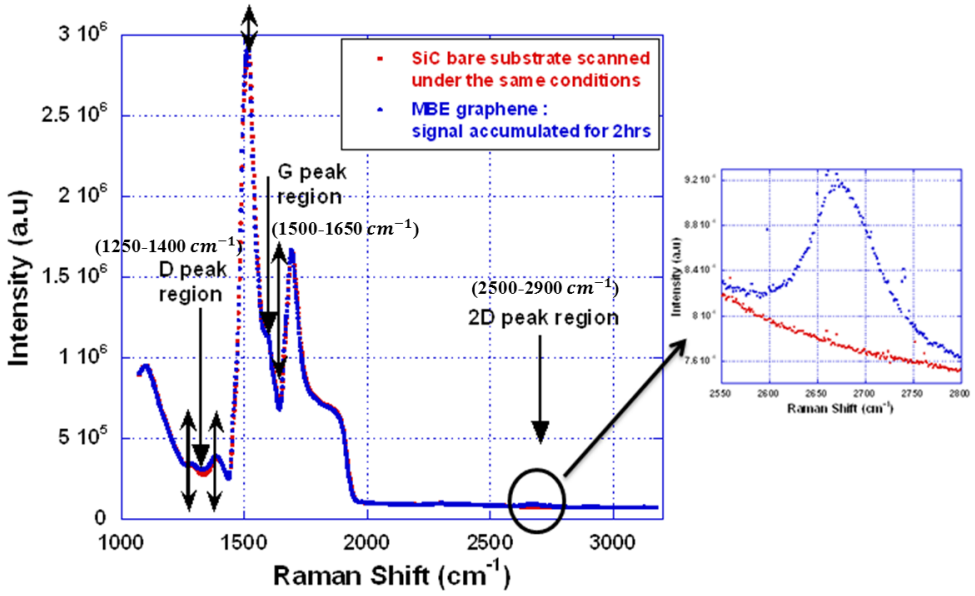

Figure 6.4: Shows the full Raman spectrum of a typical MBE grown graphene grown on 4H SiC $(000\bar{1})$ substrate. The film and the substrate lie exactly on top of each other. The specific regions where the subtraction procedure is followed are : D region (1250-1400 cm^{-1}) and G region (1500-1650 cm^{-1}). The 2D region is devoid of any substrate peaks which becomes easy to handle.

Subtraction Procedure

Fig 6.4 shows 2 important segments in the Raman spectrum: D peak region (1250-1400 cm^{-1}) and the G peak region (1500-1700 cm^{-1}). The subtraction procedure is done very carefully in these two segments by aligning the substrate peaks of the grown graphene sample with that of the bare substrate. But, a simple subtraction of the background due to the substrate is sufficient in the 2D peak region (2500-2900 cm^{-1}) which is devoid of any substrate peaks. The subtraction procedure is always done keeping the SiC substrate peaks in each segment as reference which are always present in the grown graphene samples. Because of the difference in the optical paths due to the grown graphene overlayer, the substrate peaks in the film is slightly shifted compared to the bare substrate. When the signal strength of the graphene peaks is very strong, this small lateral shift in the peaks can be neglected and a trivial subtraction would suffice. But, when

we are trying to extract signal from films which are just 2-3 MLs thick (where the signal due to graphene is really weak), this small lateral shift of the substrate peaks in the film compared to the bare substrate can not be neglected. When the substrate spectrum is simply subtracted from the film spectrum, it gives rise to a lot of artefact peaks in addition to the real peaks which is a result of the background due to subtraction. Hence, not only the substrate peaks in the bare sample are scaled in the intensity to match the substrate peaks of the film, they are shifted laterally so that the substrate peak positions in the film and the bare substrate exactly match. The exact shifting and scaling procedure is as follows :

- The D-peak region (1250-1400 cm^{-1}) or the G-peak region (1500-1700 cm^{-1}) is chosen.

- In the D-peak region, the bare SiC substrate induced peaks at 1280 cm^{-1} and 1390 cm^{-1} are scaled vertically such that they exactly match the SiC substrate peaks of the film in terms of their intensities.

- As has been mentioned above, the bare substrate peaks (1280 cm^{-1} and 1390 cm^{-1}) in the D-peak region have a very small lateral shift to the order of 10 cm^{-1}. The lateral shift is determined by carefully looking at the shift between the substrate peaks of the film and that of the bare substrate. Now, the vertically scaled substrate peaks in this D-peak region are fit to a cubic spline function and then they are extrapolated with respect to the substrate features of the grown film. This results in the substrate features of the film and the bare substrate match not only in terms of their intensity but also in terms of their position.

- The substrate peaks of the film and the bare substrate are exactly aligned such that the lateral shift is reduced to as low as $\sim$1 cm^{-1} and the substrate peak intensities in the film and the bare substrate match to the highest level of accuracy. Now the bare substrate signal is subtracted from the film signal in this D-peak region in order to extract the D peak.

- Even after the careful vertical-scaling and lateral-shifting, a background develops as a result of the subtraction in addition to the actual D peak. The position of the D peak is found from the Raman spectra of an exfoliated graphene flake and the graphene grown on c-plane sapphire. The resultant subtracted spectrum is fit to lorentzians in order to extract the exact peak position and intensity of the D peak. The rest of the artefact peaks due to the subtraction background which do not have a physical meaning are discarded. It will be shown that the intensity of the background is almost the same in all the extracted peaks. If the D peak is really strong, these artefact peaks become negligibly small and are easily discarded. But, when working with a very thin 2 ML sample, the intensity of the actual D peak is even weaker (as will be shown later) than the background; and then the Lorentzian curve fitting becomes all the more important for accurate estimation of the peak position and intensity.

- Similar procedure as steps 2, 3, 4 and 5 are followed (in this order) for the G-peak region (1500-1700 cm^{-1}) where the substrate peaks used as reference are 1515 cm^{-1} and 1690 cm^{-1}. The actual position of the G peak is found from the Raman spectra of an exfoliated graphene flake and the graphene grown on c-plane sapphire. It will be shown that the intensity of the background due to the subtraction is almost the same in all the extracted peaks.

- The intensity of the D peak and the G peak is found by integrating the positive spectral weight in the D and G peak regions after the reference substrate spectrum is subtracted.

Fig 6.5 shows the vertically and laterally aligned D-peak region (1250-1400 cm^{-1}) of 3 samples. It can be seen in the figure that with increase of thickness, the spectral weight due to the D peak distinctly increases. Sample D170 has absolutely no spectral weight at the D peak region whereas D169 has a very small spectral weight at the D peak region and D145 has the highest spectral weight.

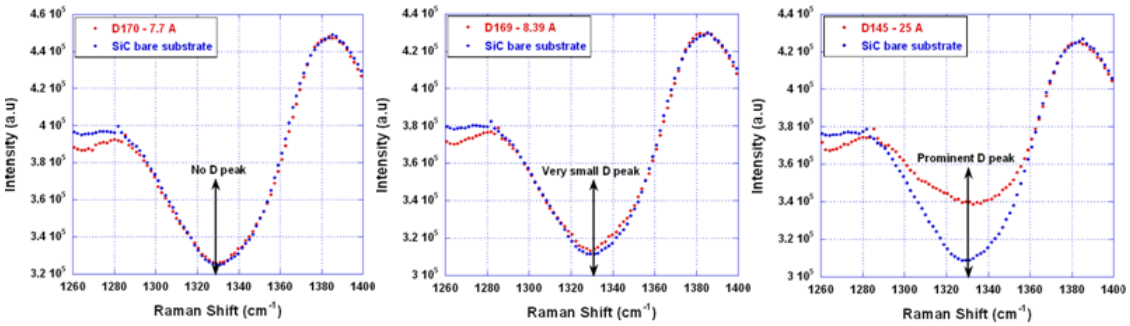

Figure 6.5: The figure shows the increase of spectral weight due to the D peak at 1322 cm^{-1} of grown graphene before the substrate spectra is subtracted. D169, the thinnest film has no spectral weight due to the D peak.

Fig 6.6 shows a typical vertically and laterally aligned G-peak region. It can be seen that there is a distinct spectral weight due to the G peak in both the samples. The thinnest sample D170 as well as the thickest sample D145 have a very similar spectral weight due to the G peak. It will be shown below that it is the ratio $\frac{I(D)}{I(G)}$ that increases with increase of thickness signifying increase of disorder.

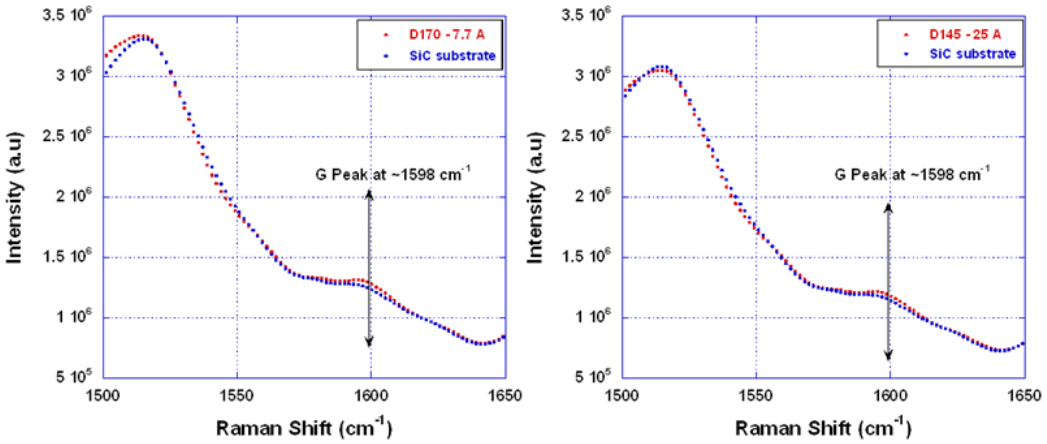

Figure 6.6: The figure shows the spectral weight due to the G peak at 1600 cm^{-1} before the substrate spectrum is subtracted. There is no appreciable change in the intensity of G peak with increase of thickness.

Extracted D and G peaks and the graphene crystallite domain size

After the spectra of the grown graphene sample and the bare substrate are well aligned in the D-peak and G-peak regions using the procedure stated above, the bare substrate spectra can be safely subtracted from the grown graphene

film spectra in order to extract the D and G peaks. The intensity ratio of D and G peaks, $\frac{I(D)}{I(G)}$ after the subtraction procedure is found out by integrating the positive spectral weight in each of the D and G peak regions. $\frac{I(D)}{I(G)}$ which is inversely proportional to the crystallite domain size gives insight about the quality of the MBE grown films. The intensity of the background due to the subtraction is almost the same in all the extracted peaks (both D and G)

As has already been discussed in the previous section, the domain size of the graphene films grown on 4H-SiC $(000\bar{1})$ is also estimated using Eq 6.2 [72].

$$L_a(nm) = (2.4 \times 10^{-10})\lambda_l^4 \left(\frac{I(D)}{I(G)}\right)^{-1} \tag{6.2}$$

where λ_l is the laser wavelength in nm and L_a is the size of the crystal domain or in-plane correlation length. It will be shown below that with increase of thickness of the grown graphene layer, the ratio $\frac{I(D)}{I(G)}$ increases (but is never > 1) and the crystallite domain size decreases. This is in stark contrast to the graphene grown on c-plane sapphire where $\frac{I(D)}{I(G)} > 2$ yielding a crystallite domain size lesser than 10 nm.

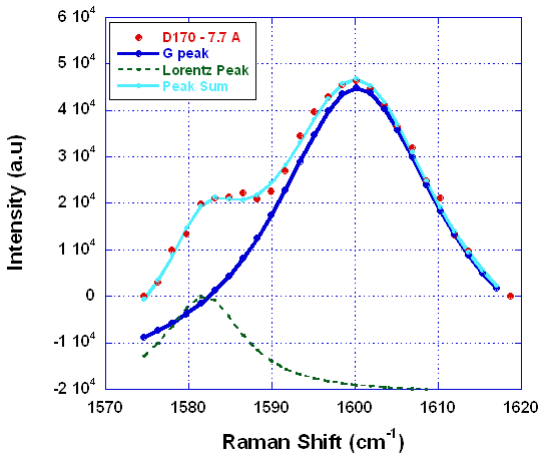

Figure 6.7: The figure shows the G peak at 1600 cm^{-1} of the thinnest (7.7 Å) obtained after subtracting the substrate spectra in the G region. The extra peak due to the subtraction is discarded after a Lorentz fit. The leftmost image of Fig 6.5 shows that it does not have a D peak.

Fig 6.7 shows the extracted G peak for a 2.3 ML (7.7 Å) graphene film grown

which has $\frac{I(D)}{I(G)} = 0$. This is the thinnest graphene sample that has been grown on 4H-SiC $(000\bar{1})$. The leftmost figure in Fig 6.5 shows that there is no conceivable spectral weight in the D-peak region. The AFM image (Fig 5.21) corroborates the Raman data which shows a very smooth morphology mimicking the underlying substrate. Although Eq 6.2 shows that the domain size should be infinite, but no long range four-probe electrical conductivity measurement could be performed on this sample. This shows that although the sample is defect free, the graphitic domains are not continuous over the size of the wafer (10 mm).

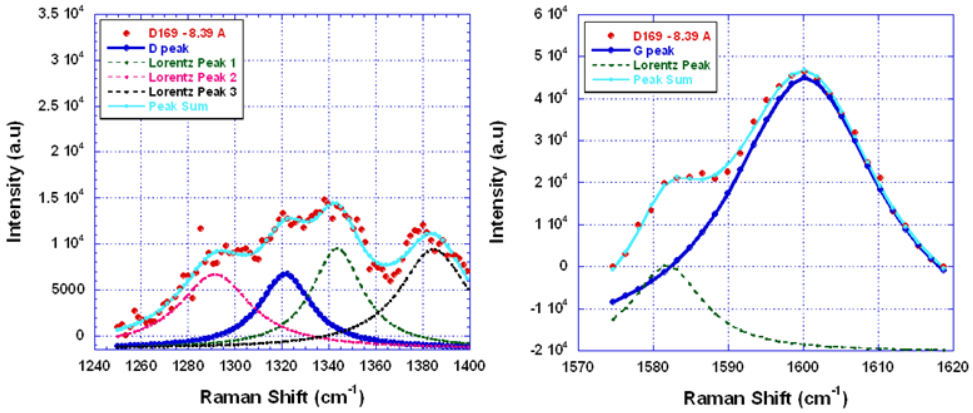

Figure 6.8: The D and G peak contribution of D169 of thickness 8.39 Å with a $\frac{I(D)}{I(G)} = 0.11$ is shown. The figure shows the G peak at 1600 cm^{-1} on the right and the D peak at 1322 cm^{-1} on the left. The artefact peaks developed in the D region due to subtraction are discarded after a Lorentz curve fitting.

Fig 6.8 shows the extracted D and G peaks for a 2.9 ML (9.62 Å) thick graphene film grown where the Lorentz curve fitting estimates the $\frac{I(D)}{I(G)} = 0.11$. The intensity of the D peak is smaller than the intensity developed due to the background due to the subtraction (which is almost the same in all the extracted peaks). Plugging in $\frac{I(D)}{I(G)} = 0.11$ in Eq 6.2, the crystallite domain size is found to be ~ 125 nm. The middle figure in Fig 6.5 shows a very small spectral weight in the D-peak region. Even after the careful vertical scaling and lateral shifting procedure adopted, many artefact peaks of the same intensity as that of the D peak still appear due to the subtraction procedure which do not have any physical significance and have been discarded after a Lorentz curve-fitting as shown in the left-half of Fig 6.8.

Although this is an epitaxial sample with streaky RHEED shown in Fig 5.19 and confirmed by AFM shown in Fig 5.22, the presence of defects from the Raman studies gives us a slight indication that the loss of epitaxy of the grown film with the substrate has already set in which could not be captured from the RHEED studies. Progressive loss of epitaxy results in the formation of granular domains. Hence, the zone-boundary phonons become active resulting in the formation of a finite D peak in the Raman spectrum.

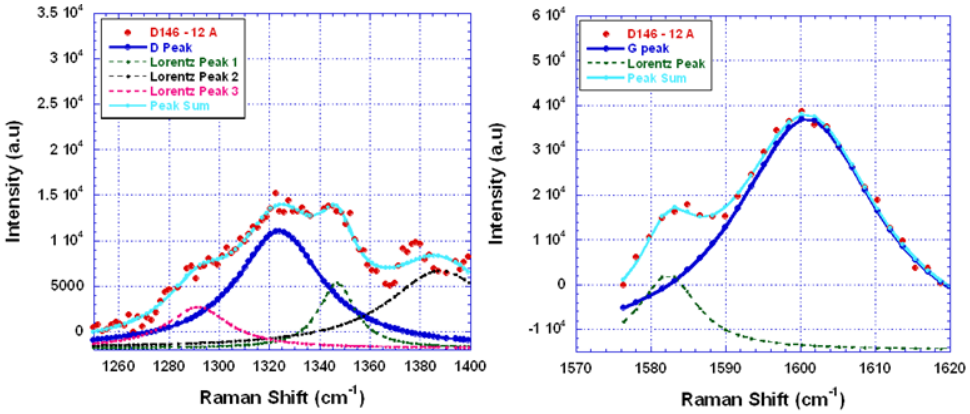

Figure 6.9: The D and G peak contribution of D146 of thickness 12.0 Å with a $\frac{I(D)}{I(G)} = 0.25$ is shown. The figure shows the G peak at 1600 cm^{-1} on the right and the D peak at 1322 cm^{-1} on the left. The artefact peaks after the subtraction procedure are discarded after a Lorentz curve fitting.

Fig 6.9 shows the extracted D and G peaks for a 3.6 ML (12 Å) thick graphene sample grown with $\frac{I(D)}{I(G)} = 0.25$. Compared to Fig 6.8, it can be seen that with increase of thickness the defect-related D peak has increased in intensity with respect to the G peak. The spectral weight due to the D peak is strong enough such that the actual D peak is stronger than the background due to the subtraction. The corresponding AFM image shown in Fig 5.23 shows the presence of granularity in addition to the terraces. This is a typical semi-epitaxial film confirmed from RHEED which shows the presence of both streaks and rings similar to what is seen in the case of c-plane sapphire (Fig 5.2). Plugging in $\frac{I(D)}{I(G)} = 0.25$ in Eq 6.2 gives the crystallite domain size as $\sim$ 55 nm. The D peak present is the dominant peak among the other artefact peaks obtained due to the subtraction procedure.

The artefact peaks are discarded after doing a Lorentz fitting similar to Fig 6.8.

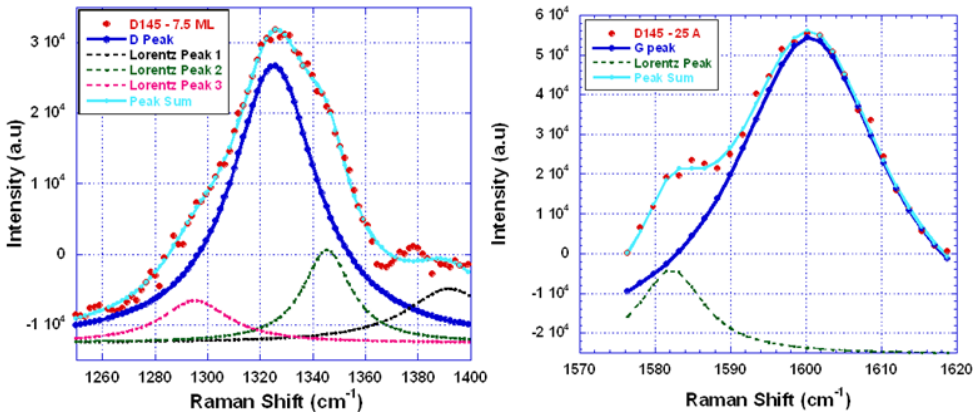

Figure 6.10: The D and G peak contribution of D145 which is the thickest sample of thickness 25.0 Å with a $\frac{I(D)}{I(G)} = 0.63$ is shown. The figure shows the G peak contribution at 1600 cm^{-1} on the right and the D peak contribution at 1322 cm^{-1} on the left. TThe artefact peaks after the subtraction procedure are discarded after a Lorentz curve fitting.

Fig 6.10 shows the extracted D and G peaks for a 7.5 ML (25 Å) thick graphene sample grown with $\frac{I(D)}{I(G)} = 0.63$. This has the most conspicuous D peak compared to the background. This is a completely granular and polycrystalline film confirmed by AFM and RHEED (not reported here). Plugging in $\frac{I(D)}{I(G)} = 0.63$ in Eq 6.2 gives the crystallite domain size as $\sim$ 22 nm. As shown in the rightmost image of Fig 6.5, the contribution due to the D peak is significantly higher than the artefact peaks which become negligibly small when the subtraction is performed and can be easily discarded even without performing a Lorentz curve fitting.

Table 6.2 shows that with increase of thickness of graphene layers, the crystallite domain size decreases as the epitaxy with the underlying substrate starts to lose after $\sim$ 4 MLs. Another important finding here is that $\frac{I(D)}{I(G)} < 1$ is always true even for the thickest graphene film grown contrary to what has been seen in the graphene grown on c-plane sapphire. It was shown earlier that graphene films grown on c-plane sapphire always had $\frac{I(D)}{I(G)} > 2$ irrespective of the thickness and morphology of the grown film and had a crystallite domain size < 10 nm. But, the crystallite domain sizes obtained using 4H-SiC $(000\bar{1})$ as the substrate for the MBE growth are at least 2 orders of magnitude greater than what was obtained

with the growths on c-plane sapphire. This is a big advantage choosing 4H-SiC $(000\bar{1})$ as the substrate over c-plane sapphire for graphene growth. Because of the difference in the crystallite domain size, the graphene films grown on 4H-SiC $(000\bar{1})$ is at least two orders of magnitude more conducting than those grown on c-plane sapphire as will be shown in the next chapter.

Table 6.2: Tabulation of the graphene crystallite domain size of the films shown in Fig 6.7, Fig 6.8, Fig 6.9 and Fig 6.10.

Sample	ML	$\frac{I(D)}{I(G)}$	$L_a(nm)$
D170	2.2	0.0	-
D169	2.5	0.11	125
D146	3.6	0.27	55
D145	7.5	0.63	22

6.2.2 Dispersion of the 2D peak with thickness and evidence of compressive stress

As has been shown in Fig 6.4, the 2D-peak region is devoid of any substrate induced Raman peaks. Hence, subtracting the background due to the substrate should be enough in order to extract the 2D peak which is straightforward compared to the extraction of D and G peaks.

Fig 6.11 shows the corresponding 2D peaks for all the samples for which the D and G peaks have been discussed except sample D169. Sample D170 (2.3 MLs) and D169 (2.9 MLs) being so very close in thickness, the position and intensity of the 2D peak are very similar and so is not included in Fig 6.11. All the 2D peaks shown could be fit to a single lorentzian irrespective of the thickness of the sample. Fig 6.11 shows that the 2D peak intensity scales with the thickness of the sample. The other striking feature is that the 2D peak position shifts to lower wavenumbers with increase of thickness contrary to what has been seen in the exfoliated graphene case [17]. It has been shown in the last chapter that the 2D peak of graphene grown on c-plane sapphire disperses to higher wavenumbers in accordance with the exfoliated case. Consistent with our

observation of the dispersion of the 2D peak to lower wavenumbers with respect to thickness, graphene grown by carbon molecular beam deposition on 6H-SiC (0001) (Si face) [57] and graphene grown by graphitization of the C-SiC substrate [86] also show a similar behavior.

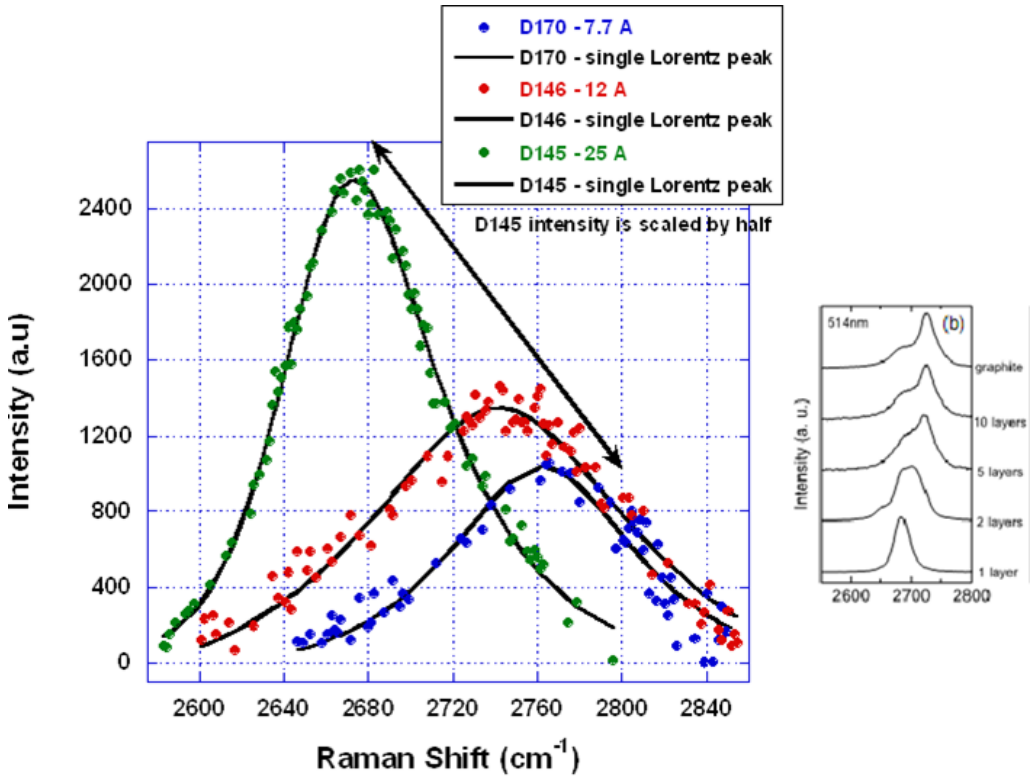

Figure 6.11: The figure shows the 2D peak of films of different thickness after subtracting the background due to the substrate which is a simple procedure. The 2D peak disperses to lower wavenumbers with increase of thickness contrary to what was seen in the c-plane sapphire case. All the 2D peaks shown have been fit to a single lorentzian implying that the peak shape does not change with thickness. The 2D peak of sample D169 is excluded in the plot which is exactly of the same intensity as D170 because they are of very similar thickness. The dispersion of the 2D peak in the exfoliated graphene case is shown for reference.

The striking feature is the position of the 2D peak at $\sim 2760cm^{-1}$ for the thinnest sample (D170) compared to a single layer exfoliated graphene which is at $\sim 2680cm^{-1}$. Rohrl et al [87] reason for such a large upshift of the 2D peak due to the presence of compressive strain in the grown epitaxial film. Rohrl [87] argues that although there is a 22 % lattice mismatch of graphene with SiC

substrate, the epitaxial graphene film is still under compressive stress instead of tensile stress contrary to what is seen in the case of c-plane sapphire. The real reason is the mismatch in the coefficient of thermal expansion (CTE) of graphene and SiC (CTE of graphene is lower than that of SiC). It was shown earlier that although the CTE mismatch in case of graphene on sapphire is double to that of graphene on SiC, but no such upshift of the 2D peak signifying compressive stress was seen. It was reasoned out that the interaction of the graphene overlayer with the underlying sapphire substrate is much weaker compared to what is seen in the case of SiC. RHEED studies have already established that the initial few graphene layers grown on 4H-SiC $(000\bar{1})$ substrate are clamped to the substrate and follow the exact lattice structure of the substrate. Whereas, in the case of sapphire, the graphene lattice relaxed with the progression of the growth. Hence, the CTE mismatch is bound to have a huge effect in case of graphene grown on SiC compared to the graphene-sapphire system.

After the growth at 1050 °C, when the grown graphene sample is cooled down, SiC contracts at a much faster rate compared to graphene putting the graphene overlayer under a lot of compressive stress. Even the 22 % lattice constant mismatch is not enough to offset this compressive stress. Lee et al [74] performed a simple experiment where they transfer the grown graphene on SiC to SiO_2 substrates and the Raman position of the 2D peak of the transferred graphene sample shifted back to a position comparable to the exfoliated case which is devoid of any compressive stress. Rohrl [87] argues that as the growth progresses and the thickness of the graphene overlayer increases, this compressive stress is released and the 2D peak disperses to lower wavenumbers. This is precisely what is seen in our case of MBE grown graphene on 4H-SiC $(000\bar{1})$ which confirms that the grown graphene overlayer is under compressive stress contrary to the presence of tensile stress in the case of graphene grown on c-plane sapphire.

As is shown in Fig 6.11, the shape of the 2D peak does not change with thickness which is a normal feature for exfoliated graphene [17]. It was shown earlier that the 2D peak of graphene grown on c-plane sapphire did not change in shape with

increase in thickness as well. Hass [52] and Latil [69] have shown that multi-layer graphene grown by graphitization of SiC on the C face have a single-lorentzian 2D peak. This is also a characteristic feature of turbostatic graphite. Hass and Latil argue that the stacking of graphene layers on the C face is not **AB** stacked but follows a random sequence. Hence, each layer is electronically decoupled from its neighboring layer. So, the single layer character is preserved even in a multi-layer film. We believe that our MBE graphene film grown on the C face which also shows a symmetrical 2D peak characteristic of a single layer graphene is the consequence of the loss of **AB** stacking order.

Thus, Raman studies confirm that the MBE grown graphene on 4H-SiC $(000\bar{1})$ substrate are under a compressive stress rather than a tensile stress contrary to the graphene grown on c-sapphire. The Raman data corroborate the RHEED and the AFM results that the interaction of the grown graphene layer with the underlying substrate is strong as a result of which the initial few graphene MLs are clamped to the substrate, thus following the substrate lattice structure. This conformal morphology of the graphene overlayer with the underlying substrate shows up in the low temperature electrical transport to be studied in the next chapter.

6.3 Conclusion

The major differences drawn from the Raman studies of the graphene films grown on c-plane sapphire and 4H-SiC $(000\bar{1})$ substrate are as follows:

- Raman spectroscopy of graphene grown on 4H-SiC $(000\bar{1})$ is tough since the typical graphene peaks are exactly in the location of very intense SiC substrate peaks which led to a very careful extraction procedure in order to isolate the typical graphene features. On the contrary, no such interference due to the substrate happens in the case of Raman studies of graphene grown on c-plane sapphire.

- Graphene films grown on c-plane sapphire have a $\frac{I(D)}{I(G)} > 2$ which gives a crystallite domain size < 10 nm irrespective of the thickness of the film. Whereas, the graphene films grown on 4H-SiC $(000\bar{1})$ substrate always has the $\frac{I(D)}{I(G)} < 1$ which gives a crystallite domain size at least two orders of magnitude higher than that of the graphene films grown on c-plane sapphire. This result is in resonance with what is seen from the AFM studies studied in the previous chapter where it was seen that even the thinnest epitaxial graphene grown has hexagonal faceting and hence the presence of grain boundaries. But, the graphene films grown on 4H-SiC $(000\bar{1})$ is very conformal to the underlying substrate implying less grain boundaries and bigger crystallite domain sizes. In fact, the D peak was absent in the 2ML epitaxial graphene film. This result is very crucial in determining why the graphene films grown on 4H-SiC $(000\bar{1})$ is more conducting than the films grown on c-plane sapphire. The $\frac{I(D)}{I(G)}$ increases with increase of thickness as the growth progresses into the polycrystalline phase in both the classes of graphene films resulting in progressive decrease in the crystallite domain size.

- The split of the G peak for the thinnest graphene film (1.5 ML) grown on c-plane sapphire confirms the presence of tensile stress in the initial few MLs of graphene grown. The 2D peak position in the case of graphene grown on 4H-SiC $(000\bar{1})$ is upshifted by $\sim 50 cm^{-1}$ confirming the presence of compressive stress in the film due to the mismatch of coefficient of thermal expansion (CTE) of graphene and SiC. This compressive stress is released with increase of thickness resulting in the restoration of the 2D peak to its relaxed position. Although the CTE mismatch exists in the graphene-sapphire system as well, but the graphene films grown are not as conformal as in the case of graphene-SiC system. Hence, the CTE mismatch in the graphene-sapphire system has a very negligible effect and only tensile stress dominates.

- The 2D peak position in the case of graphene films grown on c-plane sapphire shifts to higher wavenumbers with increase of thickness in accordance to the exfoliated graphene case. Whereas the 2D peak position in the graphene films grown on 4H-SiC $(000\bar{1})$ shifts to lower wavenumbers with increase of thickness.

- The symmetric nature of the 2D peak does not change with thickness confirming monolayer character in multilayer graphene films grown both on c-plane sapphire and 4H-SiC $(000\bar{1})$ which is an indication of the loss of **AB** stacking order.

CHAPTER 7

ELECTRICAL TRANSPORT STUDIES OF THE GROWN GRAPHENE FILMS

In this chapter, the electrical transport studies in terms of temperature dependence of sheet resistance (R_s) of the MBE grown graphene films on c-plane sapphire and 4H SiC $(000\bar{1})$ will be described in detail. The electrical transport results which are non-metallic in nature will corroborate the findings from the growth and morphology studied in Chapter 5 and the Raman studies done in Chapter 6. As it has already been established in Chapter 5, graphene films grown on each substrate progressively lose epitaxy with increase of thickness resulting in polycrystalline (granular) films. The electrical transport studies will be performed on graphene films which range from the thin epitaxial regime to completely granular regime. The electrical transport results will be split into low and high temperature regimes where the transport behavior is different. Our interpretation of the transition of the transport behavior seen at high temperatures to the low temperatures will be presented.

It will be shown that the graphene films grown on c-plane sapphire follow a power-law behavior at high temperatures for all thicknesses which transitions to a Variable Range Hopping (VRH) type behavior (interplay of 2D and 3D VRH) at lower temperatures. However, the thick polycrystalline graphene films grown show a power-law behavior at lower temperatures as well.

The graphene films grown on 4H SiC $(000\bar{1})$ will also be shown to follow a power-law behavior at high temperatures for all thicknesses. But, the low temperature transport does not show any evidence of power-law transport unlike the c-plane sapphire case. VRH type behavior of the Efros Shklovskii type dominates the low temperature transport of these graphene films.

Thus, a transition from a power-law type behavior seen at higher temperatures to a VRH type behavior seen at lower temperatures is seen in all the graphene films. But, it will be shown that the type of VRH behavior seen in both the classes of graphene films is different which is a direct consequence of the difference in morphology of the graphene films grown on each substrate.

7.1 Electrical transport of graphene grown on c-plane sapphire

The temperature dependent sheet resistance (R_s) of graphene films grown on c-plane sapphire shows a non-metallic behavior. All the samples that will be discussed in this section have been grown under the same growth conditions (growth temperature = 1050 °C and growth rate of C = 0.1 Å/s). The samples range from very thin epitaxial regime which have an extremely flat morphology (from the AFM studies) to completely polycrystalline films which have a granular AFM. The samples with intermediary thickness are semi-epitaxial where the RHEED is a superposition of streaks and rings as has already been discussed. All the samples discussed here follow a power law transport at high temperatures which follow a systematic trend in terms of thickness of the film. At lower temperatures, it will be shown that the temperature dependent behavior departs from power law and follows a generalized Variable Range Hopping (VRH) behavior (described in detail in this section).

7.1.1 High temperature regime

At high temperatures, sheet resistance (R_s) follows a power law behavior given as:

$$R_s = R_{s_0} T^{-p} \tag{7.1}$$

where R_{s_0} is a constant and p is the exponent. At high temperatures, p is given by p_H and at low temperatures, p is given by p_L.

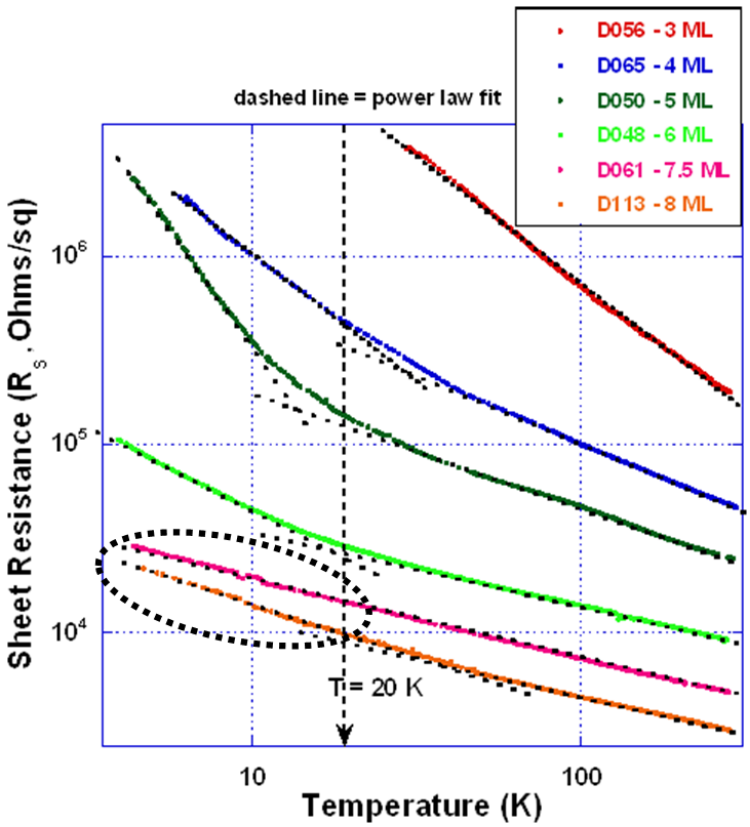

Figure 7.1: Variation of sheet resistance with temperature for graphene films of different thicknesses grown on c-plane sapphire. The power law exponent changes at $\sim$ 20 K: the exponents at high temperature (p_H) and at low temperatures (p_L) are mentioned. Below 20K, the circled polycrystalline films (D061 and D113) show a power law behavior whereas the rest will show a VRH type behavior.

The data shown in Fig 7.1 shows samples which are completely epitaxial (Sample D056 and D065), semi-epitaxial (Sample D050 and D048) and polycrystalline (Sample D061 and D113). But, Raman spectroscopy shows that all the samples have a defect related D peak with the graphene crystallite size $<$ 10 nm irrespective of the thickness of the samples signifying disorder. The data is plotted in a log-log scale and an agreement to the power law would mean the data points would lie on a straight line. All the samples presented here show excellent agreement to the power law, where the exponent of the power law changes at $\sim$ 20 K except for samples D056 and D061 which follow a single power law down to the lowest temperature at which a legitimate resistance value could be measured for

these samples. The low p_L and high p_H temperature exponents from the power law fittings are tabulated below.

Table 7.1: Tabulation of the low temperature p_L and high temperature p_H power law exponents

Sample	ML	p_H	p_L
D056	3	-0.92	-
D065	4	-0.69	-1.3
D050	5	-0.60	-2.4
D048	6	-0.47	-1.1
D061	7.5	-0.38	-0.38
D113	8	-0.35	-0.6

Looking carefully at the data shown in Fig 7.1, it can be seen that the modulus of the exponent of the power law at high temperatures (p_H) systematically decreases with increase of thickness and $|p_H| < 1$. This systematic behavior is demonstrated in Fig 7.2 where the absolute value of the high temperature exponent p_H is shown. This dependence of p_H on thickness is called power-law localization [23] seen in our graphene films. Imry et al [23] have seen a similar power law behavior at

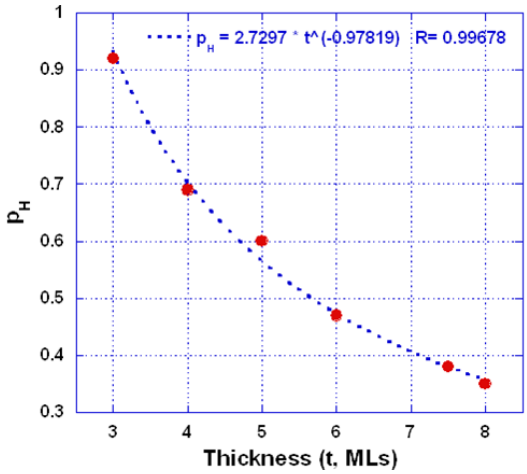

Figure 7.2: p_H systematically decreases with increase of thickness t: $p_H \propto \frac{1}{t}$. According to Imry et al [23], this particular dependence of power-law exponent on thickness is a sign of power-law localization.

higher temperatures in their indium oxide thin films which transitions to a VRH type behvaior at lower temperatures. We also a see a similar VRH type behavior

at lower temperatures to be discussed next. Imry argues that if the inelastic scattering time (τ_{in}) is power-law dependent on the temperature ($\tau_{in} \propto T^{-p}$), then the sheet resistance which is proportional to the inelastic scattering time (τ_{in}) is also power law dependent on temperature. When the inelastic scattering time (τ_{in}) is exponentially dependent on temperature, then the temperature dependent transport is described by VRH models to be discussed next. The transport current in an insulating regime is aided by the inelastic scattering events which allow a charge to move from one localized trap to another. Thouless [88] raised the possibility of conductivity increasing as a power law of temperature in highly resistive quasi-one-dimensional (1D) wires where he argues that in a strongly-localized phase, the inelastic scattering time (τ_{in}) is larger than the time it takes for a quasiparticle to diffuse quantum mechanically a distance comparable with the localization length ξ. In this case, τ_{in} is equivalent to a hopping time seen in a transport regime described by VRH. But, in a weakly localized regime, τ_{in} can be power-law dependent on temperature. Our observation is similar to what Imry has seen in his indium oxide thin films where the high temperature behavior is described by a power law where the localization is "weak". It will be shown next that at low temperatures, the localization becomes stronger and the transport behavior is described by a VRH model.

Around 20K, the modulus of the exponent of the power law changes to a value > 1 for all the samples except D056, D061 and D113 as shown in Table 7.1. Thinnest epitaxial sample, D056 (p = -0.92) and polycrystalline sample, D061 (p = -0.38) follow the same power law to the lowest temperature measured whereas polycrystalline sample, D113 ($p_L = -0.6$) follows a change in power law below 20 K. But, the samples with intermediary thickness (D065, D050 and D048) have ($|p_L| > 1$) at lower temperatures. We believe, that the temperature dependent sheet resistance for these samples have an exponential dependence described by Variable Range Hopping (VRH) models to be described in detail next.

The high temperature behavior for all the samples irrespective of thickness is described by a legitimate power law. But, the low temperature transport behavior

looks that it can be either power-law dependent as shown in Fig 7.1 (for the thicker polycrystalline samples D061 and D113) or exponentially activated described by a VRH model (for samples with intermediary thickness: D065, D050 and D048 where $|p_L| > 1$). Let us first analyze the low temperature behavior of all the samples with a VRH model before we arrive at a conclusion.

The non-exponential (power law) behavior seen at higher temperatures signifies enhanced electrical transport between the crystal domains formed and is an indication of the presence of intermediate level of disorder. Similar power law behavior has also been seen in nano crystalline graphene [89], single-walled carbon nano tubes [90] and other semi-metallic systems [91].

7.1.2 Low temperature regime

The temperature dependent transport departs from power law behavior with lowering of temperature except D056 which follows power law dependence of sheet resistance from room temperature down to 30 K (the lowest temperature at which a legitimate value of resistance could be registered). Intuitively it looks like that the temperature dependent sheet resistance (R_s) becomes exponential below ∼20 K implying either Arrhenius type, Variable Range Hopping (VRH) type or Weak Localization (WL) type behavior. It will be shown below that graphene grown on c-plane sapphire does not follow Arrhenius transport at low temperatures. In systems with disorder, the probability of finding an electron at its original position is enhanced due to positive interference between two phase coherent time-reversal trajectories in any closed loop, known as electron Weak Localization (WL). Although WL might be a plausible explanation [92, 93, 94, 95, 18] for the insulating behavior below 20 K, we have verified that the fittings to the WL model are good only below 5 K. So, unless proper magnetotransport measurements are done on these samples, it is very difficult to conclusively establish the WL dependence of sheet resistance for such a small temperature range ($5K < T < 4.2K$).

The only reasonable explanation for the low temperature transport (below 20

K) lies in the VRH regime. Since, it will be shown that the samples do not strictly adhere to any established VRH model, we explain the transport using a generalized VRH model. The low temperature behavior of all the samples (whose high temperature behavior has already been described above) will be described here so that we are convinced whether the low temperature transport is governed by a power law or VRH.

Mott's Variable Range Hopping model gives the relation between sheet resistance R_s and temperature T as:

$$R_s \propto \exp(C/T^p) \tag{7.2}$$

where C is a constant. The model is valid for a 3D system for $p = 1/4$, for a 2D system for $p = 1/3$ and for a 1D system for $p = 1/2$. But, Mott does not take into account Coulomb interaction between the charged states in the VRH model.

Considering the Coulomb interaction between the charged states, Efros and Shklovskii show that the resistance follows $p = 1/2$ in the Mott VRH model described in Eq 7.2. This is famously known as Efros Shklovskii VRH model.

But, in our case, it is not clear from the temperature dependence of sheet resistance which VRH law holds. Hence, we analyze the data below ∼20 K in a generalized VRH scheme as shown below :

$$R_s = R_{s_0} \exp\left(\frac{T_0}{T}\right)^p \tag{7.3}$$

where R_{s_0}, T_0 are constants and p is the exponent.

Taking natural log on both sides of Eq 7.3:

$$\ln(R_s) = \ln(R_{s_0}) + \left(\frac{T_0}{T}\right)^p \tag{7.4}$$

Further simplying :

$$\ln(R_s) = A + B\left(\frac{1}{T}\right)^p \tag{7.5}$$

where $A = \ln(R_{s_0})$, $B = T_0^p$ and p is the exponent. This would be referred to as the generalized VRH model henceforth.

The data below ~20 K is fit according to Eq 7.5 where A, B and p are the fit parameters from which the exponent p is determined as shown in Fig 7.3. Only the temperature dependent sheet resistance data below ~20 K is shown here. The full scale temperature data has been shown in in the previous section in Fig 7.1. The evaluated fitting parameters A and B are not displayed in Fig 7.3.

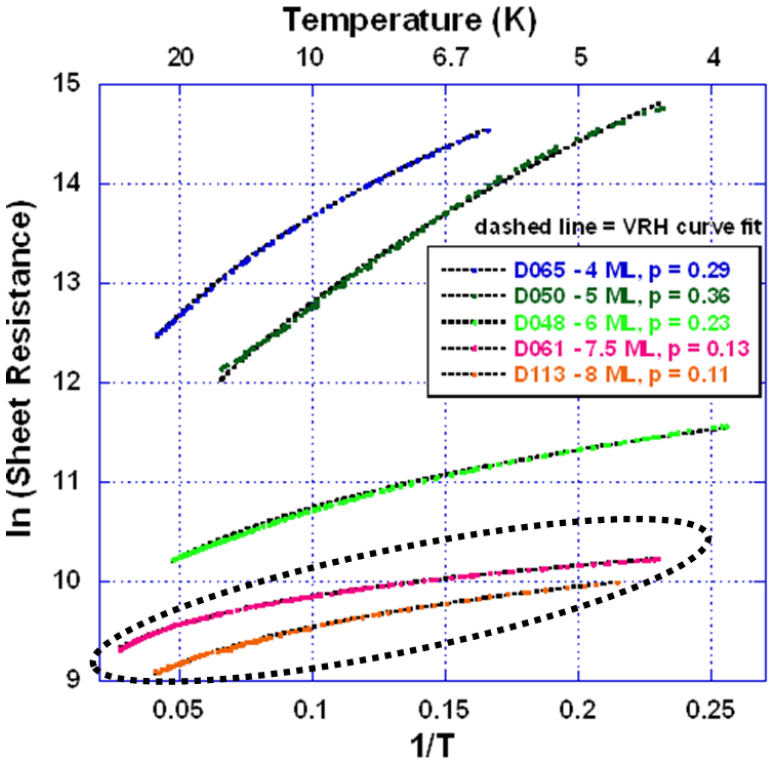

Figure 7.3: Variation of sheet resistance with temperature fit to a generalized VRH model for T $\leq$ 20 K. The exponent (p) of the generalized VRH fit (displayed by dashed lines) to the data is mentioned for each sample. The circled curves of the polycrystalline samples D061 and D113 do not follow any established VRH model.

Fig 7.3 shows the fittings to the generalized VRH model (Eq 7.5) of the temperature dependent sheet resistance. It can be seen that only the samples with intermediary thickness: D065, D050 and D048 yield VRH exponent p: 0.29, 0.36 and 0.23 respectively. These values are close to the 2D and 3D Mott VRH models. Whereas the polycrystalline samples D061 and D113 have VRH exponent p: 0.13

and 0.11 respectively which are not close to any realistic VRH model. Hence, we are absolutely convinced that the low temperature transport of thick polycrystalline graphene films grown on c-plane sapphire is governed by a power-law and not by VRH.

For samples with intermediary thickness: D065, D050 and D048 displayed in Fig 7.3, it can be seen that the exponent p lies within the scope of both 2D ($p = 0.33$) and 3D ($p = 0.25$) Mott VRH. The values of the exponent obtained from the fits show that D065 ($p = 0.29$) and D050 $p = 0.36$ are closer to being governed by the 2D Mott VRH transport whereas the thicker sample (D048 $p = 0.23$) is closer to being governed by the 3D Mott VRH. From the RHEED studies, it has already been established that with the progression of growth, graphene progressively loses epitaxy with the substrate. The growth tends to become polycrystalline where the graphene domains become nanocrystalline with increase of thickness. Thus, with increase of thickness 3D character tends to set in described by a granular morphology. Thus the low temperature transport data described by a 3D Mott VRH for the thickest film (D048) which is polycrystalline and a 2D Mott VRH for the films with intermediary thickness (D065 and D050) which are semi-epitaxial in nature is consistent with the AFM and RHEED studies. But, the range of values of p obtained definitely indicates an interplay of both the 2D and 3D Mott VRH transport where one behavior might be dominant over the other; but the other behavior can not be disregarded altogether. Similar behavior has also been seen in graphene grown by graphitization of SiC as shown in the PhD thesis [18].

The transport behavior for graphene grown on c-plane sapphire is conclusively described by a power law in the high temperature regime for samples with all thicknesses. Whereas, at lower temperatures (below 20 K), the samples which range from being epitaxial to semi-epitaxial are described by a generalized VRH model (where the 2D and 3D Mott VRH are dominant). But, the thicker polycrystalline samples follow a legitimate power law behavior even at lower temperatures. Hence, a transition from a "weak" localization (described by a power-law) to a "strong" localization (described by VRH) happens for all the graphene films grown

on c-plane sapphire.

7.2 Electrical transport of graphene grown on 4H SiC $(000\bar{1})$

Similar to the transport of graphene grown on c-plane sapphire, the electrical transport of MBE grown graphene on 4H-SiC $(000\bar{1})$ substrates exhibit a non-metallic behavior for all thicknesses. All the samples that will be discussed in this section have been grown under the same growth conditions (growth temperature = 1050 °C and growth rate of C = 0.2 Å/min). The temperature dependence of sheet resistance of samples of varying thickness will be discussed here. These samples range from being completely epitaxial described by a flat and non-granular morphology to being completely polycrystalline. It will be shown here that the electrical transport of all these samples display a power law dependence of the sheet resistance in the high temperature regime followed by a generalized VRH transport at lower temperatures.

7.2.1 High temperature regime

At high temperatures, sheet resistance (R_s) follows a power law behavior given as:

$$R_s = R_{s_0} T^{-p} \tag{7.6}$$

where R_{s_0} is a constant and p is the exponent. At high temperatures, p is given by p_H and at low temperatures, p is given by p_L.

Fig 7.4 shows sheet resistance vs temperature plotted in a log-log scale. Agreement to a power law would imply the data points would lie on a straight line. Unlike the graphene films grown on c-plane sapphire, the low temperature transport in this case does not follow a legitimate power law (p_L does not hold any meaning here). Hence, the power law dependent sheet resistance is only analyzed in the high temperature regime.

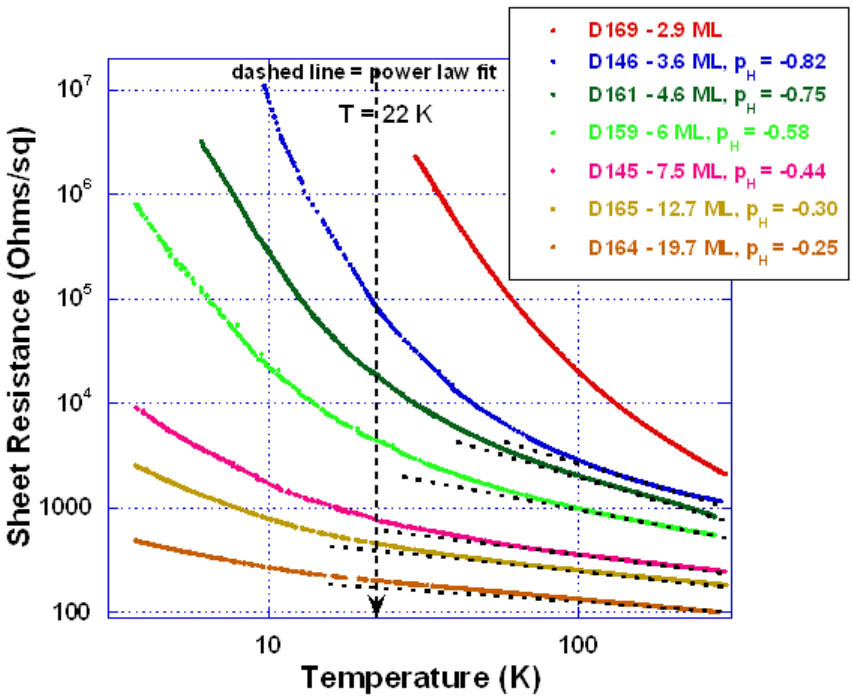

Figure 7.4: Variation of sheet resistance with temperature for graphene films of different thicknesses grown on 4H SiC $(000\bar{1})$. The data is plotted in a log-log scale and fits to a power law in both the high and low temperature regimes where the exponent of the power law changes at $\sim$ 16 K. The exponents for the low p_L and high p_H temperatures are mentioned.

The data displayed in Fig 7.4 shows that the samples can be classified into three categories : the thin epitaxial sample (D169) of thickness $<$ 3 ML, the semi-epitaxial samples (D146, D161 and D159) of thickness t lying in the range: 3 ML $< t \leq$ 6 ML and the polycrystalline samples (D145, D165 and D164) of thickness $>$ 6 ML. All these samples shown follow a reasonable power law behavior at high temperatures upto $\sim$ 22 K. The thinnest epitaxial sample D169 does not follow any reasonable power law in any temperature regime; but it will be shown to follow the VRH model (to be described next) at all temperatures.

The semi-epitaxial samples (D146, D161 and D159) and the polycrystalline samples (D145, D165 and D164) have the high temperature exponent p_H lying in the range : $0.25 \leq |p_H| \leq 0.82$. The modulus of the high temperature exponent p_H systematically decreases with increase of thickness for all the samples as shown in Fig 7.5. This dependence of p_H on thickness is termed as power-law

localization seen in our graphene films in the high temperature regime. Similar

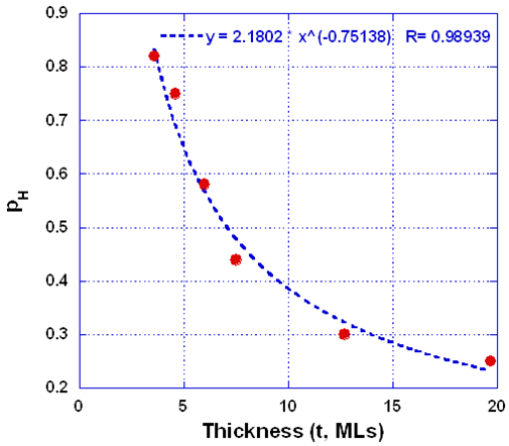

Figure 7.5: p_H systematically decreases with increase of thickness t: $p_H \propto \frac{1}{t^{0.75}}$. According to Imry et al [23], this particular dependence of power-law exponent on thickness is a sign of power-law localization.

to the high temperature behavior of graphene films grown on c-plane sapphire, power-law localization is also seen in the graphene-SiC system as well. The reason that the high temperature behavior of the sheet resistance is described by a power-law is because that the inelastic scattering time τ_{in} is power-law dependent on temperature [23]. As has already been described, a similar kind power-law behavior was seen by Imry et al [23] in their Indium Oxide thin films at high temperatures which transitions to a VRH type behavior at low temperatures. It will be described next that the low temperature behavior is indeed described by a VRH model. Imry [23] describes this transition of temperature dependent sheet resistance described by a power law at high temperatures to a VRH law at low temperatures as a weaker to a stronger localization. Power-law dependent sheet resistance is a signature of "weak" localization whereas VRH dependent sheet resistance is a signature of "strong" localization.

The non-exponential dependence of sheet resistance with temperature described by a power law model strongly indicates an enhanced electrical transport between the neighboring nanocrystals. This power law like behavior has been seen in nanocrystalline graphene [89], single-walled carbon nano tubes [90] and other

semi-metallic systems [91]. As explained by Tan et al [94], confirmation to power law transport is an indication of the presence of intermediate level of disorder in graphene. Tan et al [94] argue that the Dirac fermions in graphene tend to be delocalized against disordering yielding a Kosterlitz-Thouless type of critcial behavior [96] in the presence of strong disorder. It will be shown in the following section that the departure from power law transport below ∼22 K is best described in the VRH regime.

7.2.2 Low temperature regime

Similar to the graphene grown on c-plane sapphire described in the last chapter, the low temperature transport is intuitively exponential, but not Arrhenius type (as will be shown below). In systems with disorder, the probability of finding an electron at its original position is enhanced due to positive interference between two phase coherent time-reversal trajectories in any closed loop, known as electron Weak Localization (WL). Although WL might be a reasonable explanation [92, 93, 94, 95, 18] of the low temperature transport data, but the WL model fits our data only below 5 K. Hence, without performing any magnetotransport measurements, it is difficult to make any definite conclusions of the presence of WL in our low temperature transport data just on the basis of fits in the temperature range : $5K < T < 4.2K$. An approach (generalized VRH model) similar to what has been described in the graphene-sapphire system will be presented for the low temperature analysis of the data. All the samples discussed in the previous section will be again described here below $\leq$ 22 K.

Following the approach already described in the last section, the generalized VRH model is given as:

$$\ln(R_s) = A + B\left(\frac{1}{T}\right)^p \tag{7.7}$$

where $A = \ln(R_{s_0})$, $B = T_0^p$ and p is the exponent.

The data below ∼22 K is analyzed according to Eq 7.7 where A, B and p are

the fit parameters from which the exponent p is determined as shown in Fig 7.6. The evaluated fitting parameters A and B are not displayed in Fig 7.6.

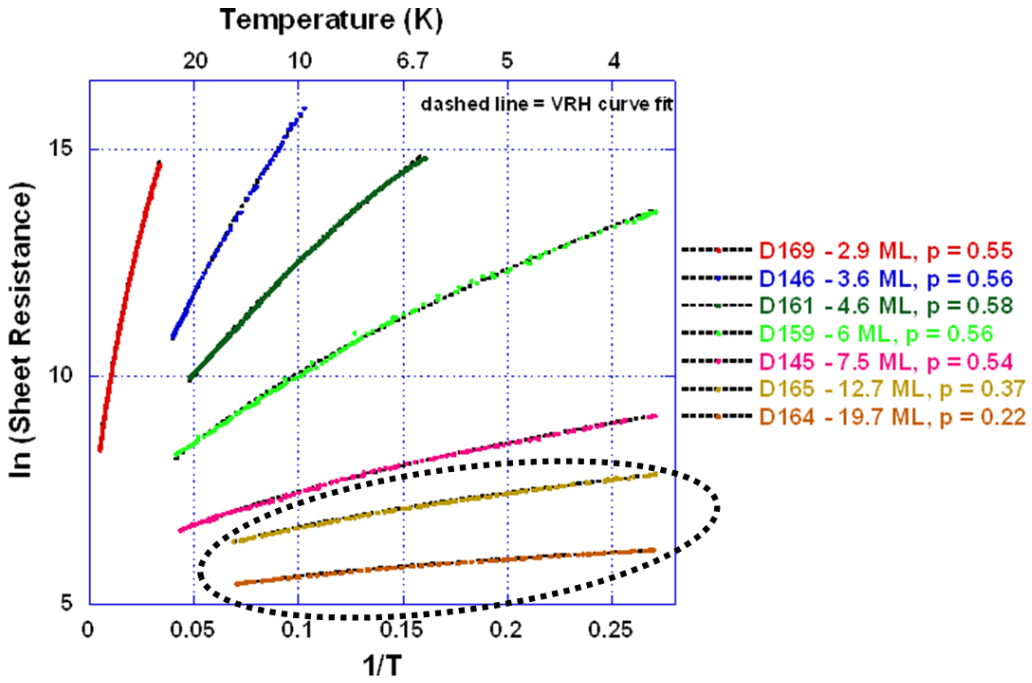

Figure 7.6: Variation of sheet resistance with temperature fit to a generalized VRH model for T $<$ 22 K except D169 which fits the model in the range 30 K $<$ T $<$ 200 K. Except for the circled samples: D165 and D164 which have a granular morphology, the rest of the samples show an Efros Shklovskii VRH behavior. The exponent (p) of the generalized VRH fit to the data is mentioned for each sample.

Fig 7.6 shows the temperature dependent transport fit to the generalized VRH model as has been done on graphene grown on c-plane sapphire in the previous section. All the samples are analyzed below $\sim$22 K except D169 which is the completely epitaxial non-granular 3 ML graphene film. D169 exhibits the generalized VRH transport from 200 K down to 30 K (the lowest temperature at which a legitimate value of the sheet resistance could be measured). As a reminder, sample D169 did not follow a legitimate power law contrary to the completely epitaxial graphene grown on c-plane sapphire. The rest of the samples analyzed here range from being semi-epitaxial (D146, D161 and D159) and polycrystalline (D145 and D165).

Analyzing the fitting results displayed in Fig 7.6, it can be seen that the ex-

ponent p hover around 0.5 for all the samples which are less than 8 ML thick. Thicker polycrystalline samples: D165 has $p = 0.37$ and D164 has $p = 0.22$. Reiterating the Mott VRH and Efros Shklovskii VRH models, p can take values: 0.5 (for 1D Mott VRH and disordered systems with significant Coulomb interactions), 0.33 (for 2D Mott VRH) and 0.25 (for 3D Mott VRH). The range of values of p in Fig 7.6 definitely indicates that Efros Shklovskii VRH best describes the low temperature transport for graphene films less than 8 ML thick. With increase of thickness, as the epitaxy with the underlying substrate is progressively lost resulting in completely polycrystalline granular films, the low temperature behavior departs from the Efros Shklovskii VRH type and tends towards 3D Mott VRH. It can be seen that all the samples described here except D165 and D164 have $p \sim 0.5$ described by Efros Shklovskii VRH where the Coulomb interactions are significant. All the samples which follow the Efros Shklovskii VRH behavior are epitaxial (D169, 2.9 ML), semi-epitaxial (D146 (3.6 ML), D161 (4.6 ML) and D159 (6 ML)) and polycrystalline (D145, 7.5 ML).

The fact that all these samples have a dominant Efros Shklovskii VRH behavior irrespective of its crystalline nature for thickness below 8 ML is because of its conformal morphology with the underlying substrate. It was studied in Chapter 5 that the graphene films grown on 4H-SiC $(000\bar{1})$ are clamped to the underlying substrate. Hence, the interaction between the graphene layers in such a conformal configuration is bound to be pronounced which shows up in the low temperature transport behavior (Efros Shklovskii VRH). On the contrary, the low temperature transport of graphene grown on c-plane sapphire did not have any evidence of Efros Shklovskii VRH. The AFM results of graphene films grown on c-plane sapphire described in Chapter 5 showed a faceted morphology where the graphene layers were being delaminated from the surface where it looked as if the layers were detached from each other. Thus, the inter-layer coupling is weaker in the graphene-sapphire system and hence, the Efros Shklovskii VRH behavior is absent at lower temperatures. The difference in the low temperature electrical transport proves the fact that the inter-layer coupling in the graphene-SiC system

is definitely stronger than that in the graphene-sapphire system.

Samples: D165 (12.7 ML) and D164 (19.7 ML) are the completely polycrystalline samples which have the VRH exponents: $p = 0.37$ and $p = 0.22$ respectively. With the increase of thickness (beyond 12 ML), the epitaxy with the underlying substrate is progressively lost and 3D order sets in shown by the granularity in the films. Hence, these films depart from the Efros Shklovskii VRH type behavior and tend towards 3D Mott VRH type behavior with increase of thickness as the films remain no longer two dimensional. But, the Coulomb interaction even in the thickest D164 sample can not be ruled out altogether. Similar transport behavior has also been observed in graphene grown by graphitization of SiC as shown in the PhD thesis [18].

The transport behavior for graphene grown on 4H-SiC $(000\bar{1})$ is conclusively described by a power law in the high temperature regime for all the samples which are semi-epitaxial to polycrystalline in nature. But, the thin epitaxial sample has a dominant Efros Shklovskii VRH type behavior in almost the whole range of temperature measured. There is no evidence of power-law behavior at low temperatures at all. Whereas, at lower temperatures (below 22 K), the samples which range from being semi-epitaxial to polycrystalline are described by a generalized VRH model (where the Efros Shklovskii VRH is dominant). With increase of thickness as 3D order sets in, the low temperature behavior departs from the Efros Shklovskii VRH behavior and tends towards the 3D Mott VRH type. The conformal morphology of the graphene films on 4H-SiC $(000\bar{1})$ is the main reason why Efros Shklovskii VRH plays a dominant role in the low temperature transport of graphene on 4H-SiC $(000\bar{1})$ contrary to the graphene-sapphire system. This tells us that the inter-layer coupling in the graphene-SiC system is stronger than that in the graphene-sapphire system. Hence, similar to the graphene-sapphire system, a transition from "weak" (power-law) localization to "strong" (VRH) localization also takes place in the graphene-SiC system.

7.3 Conclusion

Before drawing the conclusions based on the electrical transport results of graphene films grown on c-plane sapphire and 4H-SiC $(000\bar{1})$, it is important to understand the effect of the substrate on the sheet conductance per ML of graphene. Fig

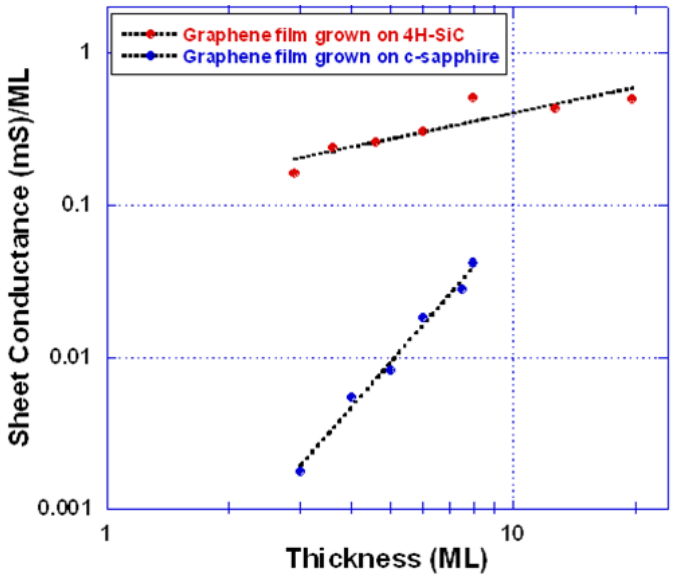

Figure 7.7: Sheet conductance/ML of graphene on c-plane sapphire and 4H-SiC $(000\bar{1})$ at room temperature.

7.7 shows the sheet conductance/ML of graphene on c-plane sapphire and 4H-SiC $(000\bar{1})$ at room temperature. The data is plotted in a log-log scale to highlight the fact that graphene grown on 4H-SiC $(000\bar{1})$ is atleast 2 orders of magnitude more conducting than that grown on c-plane sapphire. So, the underlying substrate plays a major role in the sheet conductance of the graphene overlayer. This result corroborates the Raman results discussed in Chapter 6 where it was estimated that the graphene crystallite domain size (in-plane coherence length) on 4H-SiC $(000\bar{1})$ is atleast 2 orders of magnitude bigger than the graphene films grown on c-plane sapphire. Since, the in-plane coherence length of graphene on 4H-SiC $(000\bar{1})$ is bigger than that on c-plane sapphire, the graphene grown on 4H-SiC $(000\bar{1})$ is more conducting than that on c-plane sapphire. One major similarity is that the effect of the substrate limits the sheet conductance of the initial few

MLs of graphene grown on either substrate. We speculate that the first couple of MLs of graphene on either substrate is ionically bonded to the substrate which limits the electrical conductivity. The conductivity per ML picks up with increase of thickness as a result of which the effect of the substrate is reduced. The graphene domains coalesce with increase of thickness and better continuity over a macro-scale is achieved which also results in higher conductivity per ML.

From the electrical transport results of graphene on c-plane sapphire and 4H-SiC $(000\bar{1})$, we conclude as follows:

- Temperature dependent sheet resistance shows a power-law behavior at high temperatures in the graphene films grown on both the substrates. The fact that the power-law exponent is dependent on thickness implies that power-law localization exists in the high temperature regime.

- At low temperatures, no power-law dependent transport is seen in the graphene films grown on 4H-SiC $(000\bar{1})$. But, thick polycrystalline graphene films grown on c-plane sapphire show a legitimate power-law at low temperatures.

- The low temperature transport in the case of graphene-sapphire system is an interplay of both 2D and 3D Mott VRH. Whereas, Efros Shklovskii VRH dominates the low temperature transport in the graphene-SiC system. For thicker granular films grown on 4H-SiC $(000\bar{1})$, the low temperature transport tends towards 3D Mott VRH. This difference is a direct consequence of the difference of morphology of graphene films grown on each substrate where the graphene on c-plane sapphire shows a faceted growth whereas the grapheen on 4H-SiC $(000\bar{1})$ shows a very conformal growth. Hence, inter-layer coupling in the graphene-SiC system is more than that in the graphene-sapphire system.

- The effect of substrate limits the conductance/ML of graphene on both the substrates which picks up with increase of thickness when the effect of

substrate is minimal.

- The sheet conductance/ML of graphene at room temperature grown on 4H-SiC $(000\bar{1})$ is atleast two orders of magnitude higher than that of graphene films grown on c-plane sapphire. This is a direct consequence of the difference in the graphene crystallite domain sizes (the in-plane coherence length) estimated with the help of Raman studies on each substrate. The in-plane coherence length of graphene on 4H-SiC $(000\bar{1})$ is atleast two orders of magnitude bigger than that of graphene grown on c-plane sapphire and hence the difference in the conductivity of graphene on each substrate.

CHAPTER 8

CONCLUSION AND FURTHER SCOPE

The initial foray into exploring the growth of macroscopic graphene films by MBE has yielded many interesting and fruitful results. Although this approach of growing graphene is around in the community for a year now, much more work is needed before this technique can establish itself in the modern day semiconductor industry. While the development of a full-scale manufacturable film is out of the realm of a single dissertation, there are a few more achievable near-term goals to be accomplished. This concluding chapter will summarize the results and provide directions for future research towards reliable manufacturing of uniform graphene films.

8.1 Summary of results

This dissertation proves that graphene can be grown by MBE in an epitaxial manner on an insulating substrate which has a decent lattice-matching with graphene. I have tried the growth on two different classes of insulating substrates with hexagonal symmetry: c-plane sapphire and 4H-SiC $(000\bar{1})$. The grown films were uniform in thickness over a wafer-scale (10 mm $\times$ 10 mm) and they are electrically conducting although the transport behavior is non-metallic. This proves that Molecular Beam Epitaxy (MBE) is another alternative route in the direction of achieving uniform graphene films over a wafer-scale directly on an insulating surface where one can achieve independent control over the growth rate of graphene, the deposition rate of C and the substrate temperature. This is what has been particularly missing in the growth of graphene by thermal decomposition of SiC.

Although the lattice constant of c-plane sapphire is double the lattice constant of graphene, the graphene lattice aligns itself on the c-plane sapphire lattice to reduce the lattice-mismatch down to 12 %. The growth starts in an epitaxial manner where the epitaxy lasts for about 4-5 MLs beyond which the growth becomes polycrystalline evolving through a "semi-epitaxial" phase (which has both epitaxial and polycrystalline order). The AFM images of the epitaxial graphene films are so strained to the substrate that the surface ruptures into hexagonal facets. RHEED studies confirm that with the progression of the growth, the strain in the grown film is released as the lattice relaxes described by a pseudomorphic growth mode. The haxagonal faceting of the surface seen in the AFM images are evidence of dislocations which are associated with the relaxation of the graphene lattice with the progression of the growth. The Raman Spectroscopy studies corroborate the tensile stress in the films where the G peak splits into G^+ and G^-. Furthermore, Raman studies confirm that the stacking order of the epitaxial graphene is not **AB** type since the shape of the 2D peak does not change with thickness of the graphene layers as was the the case with exfoliated graphene although the 2D peak disperses to higher wavenumbers with increase of thickness similar to exfoliated graphene. The electrical transport studies performed in terms of temperature dependence of sheet resistance shows that at high temperatures, the transport behavior is governed by a power law. Whereas at lower temperatures, the transport behavior departs from power law behavior and is described by a generalized VRH model. It is established that in most of the epitaxial and semi-epitaxial samples, the low temperature transport is an interplay of both 2D and 3D Mott VRH behavior. But, thicker polycrystalline samples show a legitimate power law behavior even at lower temperatures. Thus, the electrical transport through the flat epitaxial connected graphene domains are governed by a VRH model. As the epitaxial flat connected graphene domains get buried under the densely packed polycrystalline grains for thicker samples, the electrical transport is enhanced described by a power law type behavior at all temperatures. The description of the transport behavior at higher temperatures described by a power

law is the case of "weak" localization which switches to a "strong" localization behavior at lower temperatures described by a VRH model. Hence, a transition from "weak" to "strong" localization is seen in the electrical transport behavior.

The growth of graphene on 4H-SiC $(000\bar{1})$ substrates becomes a bit trickier as the potential source of graphene lies in the substrate itself. Since, the growths take place at 1050 °C, it is enough to sublimate Si. In fact, the sublimation of Si does happen in this case, but the formation of graphitic domains are completely ruled out by XPS studies. This is crucial since the main philosophy of this dissertation has been to independently control the growth of graphene by C deposition and not from intrusive graphitization. RHEED studies show that the growth progresses in an epitaxial manner and becomes polycrystalline beyond 5-6 MLs transitioning through a semi-epitaxial phase. The AFM studies do not show any faceting of the surface as was the case in the growths on c-plane sapphire. The AFM micrographs show a smooth, flat and terraced surface following the morphology of the underlying substrate thus confirming a pseudomorphic growth process which was corroborated by RHEED studies. Since, Si sublimation does take place, it divides the surface of every atomic terrace of the bare substrate into a smoother and a rougher portion with the rougher portion being at the terrace edge. And when the graphene growth takes place on this kind of a terraced surface, the grown graphene forms 2 phases as shown by Phase AFM microscopy since the graphene overlayer tends to bond in a different fashion to the Si desorbed portion of the terrace compared to the Si undesorbed portion. Raman studies of graphene grown on SiC is always very non-trivial since the typical graphene peaks are located exactly at the positions of the intense SiC substrate peaks. Hence, a very careful subtraction procedure is adopted to extract the graphene film peaks. The symmetric nature of the 2D peak in multi-layered graphene samples confirm the loss of **AB** stacking order similar to the growths on c-plane sapphire. The high upshift of the 2D peak in the Raman studies confirm the fact that the graphene films grown are under a lot of compressive stress rather than tensile stress as was seen in the c-plane sapphire case because of the difference in the coefficient of

thermal expansion (CTE) of graphene and SiC which does play a vital role here. The electrical transport behavior is non-metallic similar to the graphene grown on c-plane sapphire. The high temperature transport is dominated by a power law whereas the low temperature transport for the thin films ($\sim$ 7 ML) is described by a generalized VRH model where the dominant behavior is Efros Shklovskii VRH. No power law transport behavior is seen at lower temperatures unlike in the case of graphene grown on c-plane sapphire. Thus, similar to the case of c-plane sapphire, a transition from "weak" to "strong" localization is also seen in the electrical transport behavior in graphene films grown on 4H-SiC $(000\bar{1})$.

8.2 Directions for future research

The growth of graphene by MBE is still in its state of infancy with a lot more that is still need to be done which has been beyond the scope of this dissertation. Some insights into the directions for future work are presented here.

First, the quest for an insulating substrate which is exactly lattice-matched to graphene should never cease. The only insulating substrate which is exactly lattice-matched to graphene is Pyrolytic Boron Nitride (PBN); but it is not available in the epi-ready form. If an MBE growth can be designed where a flat buffer layer of PBN can be grown on the top of which graphene can be deposited, it would solve big problems related to strain associated with lattice mismatch. And doing these growths in-situ would be the key since the interface of graphene with PBN needs to be clean; and the best way to do this is by MBE.

Second, the research presented in this dissertation can be taken further if good magnetotransport measurements can be performed. This might require magnetic fields greater than 10 Tesla because of the higher electron density in the present films.

Third, since we have the potential to grow multiple materials on graphene in-situ, newer functional materials can be engineered out of epitaxial heterostructures involving graphene. This could be the key in the ongoing research of coupling

graphene with ferromagnets and superconductors. Hence, cleaner interface between graphene with the ferromagnet or a superconductor can be achieved which could be a great advancement in the area of graphene based spin-valve devices and proximity induced superconductivity in graphene.

Finally, another interesting avenue is developing an effective top gate on graphene which is being researched for a long time now. MBE has the potential to carry out the epitaxial growth of top-gate oxide dielectric in-situ on graphene resulting in a cleaner interface with the dielectric deposited. As a result, the electron concentration of graphene grown on an insulating surface can be effectively tuned for many device applications.

REFERENCES

[1] M. L. Bolen, "Exploration of epitaxial graphene on sic," Ph.D. dissertation, Purdue University, 2010.

[2] X. Li, "Epitaxial graphene films on sic : Growth, characterization and devices," Ph.D. dissertation, Georgia Institute of Technology, 2008.

[3] G. M. Rutter, "Atomic scale properties of epitaxial graphene grown on sic (0001)," Ph.D. dissertation, Georgia Institute of Technology, 2008.

[4] J. R. Hass, "Structural characterization of epitaxial graphene on sic," Ph.D. dissertation, Georgia Institute of Technology, 2008.

[5] J. Drowart et al., "Thermodynamic study of sic utilizing a mass spectrometer," *J. Chem. Phys.*, vol. 29, p. 1015, 1958.

[6] Z. Li et al., "Thermal expansion of the hexagonal 6h polytype of sic," *J. Am. Ceram. Soc.*, vol. 69, p. 863, 1986.

[7] D. K. L. Tsang et al., "Graphite thermal expansion relationship for different temperature ranges," *Carbon*, vol. 43, p. 2902, 2005.

[8] E. Moreau et al., "Graphene growth by molecular beam epitaxy using a solid carbon source," *Phys. Status Solidi A*, vol. 207, p. 300, 2010.

[9] E. Moreau et al., "Graphene growth by molecular beam epitxay on the carbon-face of sic," *Applied Physics Letters*, vol. 97, p. 241907, 2010.

[10] S. K. Jerng et al., "Nanocrystalline graphite growth on sapphire by carbon molecular beam epitaxy," *J. Phys. Chem. C*, vol. 115, p. 4491, 2011.

[11] X. Li, "Epitaxial graphene films on sic: Growth, characterization and devices," Ph.D. dissertation, Georgia Institute of Technology, 2008.

[12] J. R. Hass, "Structural characterization of epitaxial graphene on silicon carbide," Ph.D. dissertation, Georgia Institute of Technology, 2008.

[13] P. Welander, "Epitaxial aluminium oxide thin films on niobium (110): A study of their growth and their use in superconducting tunnel-junctions," Ph.D. dissertation, University of Illinois at Urbana-Champaign, 2007.

[14] S. Chen, "Structural dynamics by ultrafast electron crystallography," Ph.D. dissertation, California Institute of Technology, 2007.

[15] P. Begat et al., "The effect of mechanical processing on surface stability of pharmaceutical powders: Visualization by atomic force microscopy," *Journal of Pharmaceutical Sciences*, vol. 92, p. 611, 2002.

[16] N. Sharma, "Microscopic and spectroscopic studies of growth and electronic structure of epitaxial graphene," Ph.D. dissertation, Georgia Institute of Technology, 2009.

[17] A. C. Ferrari et al., "Raman spectrum of graphene and graphene layers," *Physical Review Letters*, vol. 97, p. 187401, 2006.

[18] G. L. Creeth, "Growth and magnetotransport studies of epitaxial graphene," Ph.D. dissertation, University of Leeds, 2010.

[19] M. Mohai, "Development and applications of quantitative x-ray photoelectron spectroscopy," Ph.D. dissertation, Institute of Materials and Environmental Chemistry, Chemical Research Center,Hungarian Academy of Sciences.

[20] L. B. Biedermann et al., "Insights into few-layer epitaxial graphene growth on 4h-sic$(000\bar{1})$ substrates from stm studies," *Physical Review B*, vol. 79, p. 125411, 2009.

[21] F. J. Ferrer et al., "Initial stages of graphitization on sic $(000\bar{1})$, as studied by phase atomic force microscopy," *Journal of Applied Physics*, vol. 109, p. 054307, 2011.

[22] Mohiuddin et al., "Uniaxial strain in graphene by raman spectroscopy: G peak splitting, gruneisen parameters, and sample orientation," *Phys. Rev. B*, vol. 79, p. 205433, 2009.

[23] Z. Ovadyahu and Y. Imry, "Conductivity power-law temperature dependence of thin indium oxide films," *J. Phys. C: Solid State Phys.*, vol. 18, p. L19, 1985.

[24] Y. Zhang et al., "Experimental observation of the quantum hall effect and berry's phase in graphene," *Nature*, vol. 438, p. 201, 2005.

[25] K. S. Novoselov et al., "Unconventional quantum hall effect and berrys phase of 2π in bilayer graphene," *Nature Physics*, vol. 2, p. 177, 2006.

[26] N. Stander et al., "Evidence for klein tunneling in graphene p-n junctions," *Phys Rev Lett*, vol. 102, p. 026807, 2009.

[27] K. S. Novoselov et al., "Room-temperature quantum hall effect in graphene," *Science*, vol. 315, p. 1379, 2007.

[28] K. I. Bolotin et al., "Observation of the fractional quantum hall effect in graphene," *Nature*, vol. 462, p. 196, 2009.

[29] X. Du et al., "Fractional quantum hall effect and insulating phase of dirac electrons in graphene," *Nature*, vol. 462, p. 192, 2009.

[30] K. S. Novoselov et al., "Electric field effect in atomically thin carbon films," *Science*, vol. 306, p. 666, 2004.

[31] M. Orlita et al., "Approaching the dirac point in high-mobility multilayer epitaxial graphene," *Phys Rev Lett*, vol. 101, p. 267601, 2008.

[32] Y. M. Lin et al., "100-ghz transistors from wafer-scale epitaxial graphene," *Science*, vol. 327, p. 662, 2010.

[33] C. Lee et al., "Measurement of the elastic properties and intrinsic strength of monolayer graphene," *Science*, vol. 321, p. 385, 2008.

[34] A. A. Balandin et al., "Superior thermal conductivity of single-layer graphene," *Nano Lett*, vol. 8, p. 902, 2008.

[35] J. S. Bunch et al., "Impermeable atomic membranes from graphene sheets," *Nano Lett*, vol. 8, p. 2458, 2008.

[36] P. R. Wallace, "The band theory of graphite," *Physical Review*, vol. 71, p. 622, 1947.

[37] G. D. R. Saito and M. S. Dresselhaus, *Physical Properties of Carbon Nanotubes*. Imperial College Press, London, 1998.

[38] H. P. Boehm et al., "Thinnest carbon foils," *Z. Naturforschg*, 1962.

[39] A. Karu and M. Beer, "Pyrolytic formation of highly crystalline graphite films," *Journal of Applied Physics*, vol. 37, p. 2179, 1966.

[40] C. Oshima and A. Nagashima, "Ultra-thin epitaxial films of graphite and hexagonal boron nitride on solid surfaces," *J. Phys.: Condens. Matter*, vol. 9, p. 1, 1997.

[41] D. V. Badami, "Graphitization of α-silicon carbide," *Nature*, vol. 193, p. 570, 1962.

[42] C. Berger et al., "Ultrathin epitaxial graphite: 2d electron gas properties and a route toward graphene-based nanoelectronics," *J. Phys. Chem. B*, vol. 108, p. 19912, 2004.

[43] K. S. Novoselov et al., "Electric field effect in atomically thin carbon films," *Science*, vol. 306, p. 666, 2004.

[44] Y. S. Dedkov et al., "Intercalation of copper underneath a monolayer of graphite on ni(111)," *Phys. Rev. B*, vol. 64, p. 035405, 2001.

[45] Q. Yu et al., "Graphene segregated on ni surfaces and transferred to insulators," *Appl. Phys. Lett.*, vol. 93, p. 113103, 2008.

[46] S. W. Bae et al., "Roll-to-roll production of 30-inch graphene films for transparent electrodes," *Nat. Nanotechnol.*, vol. Advance online publication, 2010.

[47] H. Ueta et al., "Highly oriented monolayer graphite formation on pt(111) by a supersonic methane beam," *Surf. Sci.*, vol. 560, p. 183, 2004.

[48] T. A. Land et al., "Stm investigation of single layer graphite structures produced on pt(111) by hydrocarbon decomposition," *Surf. Sci.*, vol. 264, p. 261, 1992.

[49] J. Coraux et al., "Growth of graphene on ir(111)," *New J. Phys.*, vol. 11, p. 023006, 2009.

[50] P. W. Sutter et al., "Epitaxial graphene on ruthenium," *Nat. Mater.*, vol. 7, p. 406, 2008.

[51] L. I. Johansson et al., "Stacking of adjacent graphene layers grown on c-face of sic," *Phys. Rev. B*, vol. 84, p. 125405, 2011.

[52] J. Hass et al., "Why multilayer graphene on 4h-sic $(000\bar{1})$ behaves like a single sheet of graphene," *Physical Review Letters*, vol. 100, p. 125504, 2008.

[53] Luxmi, "Structural studies of epitaxial graphene formed on sic surfaces," Ph.D. dissertation, Carneggie Mellon University, 2010.

[54] W. A. de Heer et al., "Large area and structured epitaxial graphene produced by confinement controlled sublimation of silicon carbide," *PNAS*, vol. 108, p. 16900, 2011.

[55] S. K. Banerjee et al., "Bilayer pseudospin field-effect transistor (bisfet): A proposed new logic device," *IEEE Electron Device Lett.*, vol. 30, p. 158, 2009.

[56] S. K. Banerjee et al., "Direct observation of a widely tunable bandgap in bilayer graphene," *Nature*, vol. 459, p. 820, 2009.

[57] J. Park et al., "Epitaxial graphene growth by carbon molecular beam epitaxy (cmbe)," *Adv. Matter.*, vol. 22, p. 4140, 2010.

[58] F. Maeda et al., "Molecular beam epitaxial growth of graphene and ridge-structure networks of graphene," *J. Phys. D: Appl. Phys.*, vol. 44, p. 435305, 2011.

[59] J. Hackley et al., "Graphitic carbon growth on si (111) using solid source molecular beam epitaxy," *Applied Physics Letters*, vol. 95, p. 133114, 2009.

[60] J. M. Garcia et al., "Multilayer graphene films grown by molecular beam deposition," *Solid State Communications*, vol. 150, p. 809, 2010.

[61] F. Maeda et al., "Study of graphene growth by gas-source molecular beam epitaxy using cracked ethanol: Influence of gas flow rate on graphitic material deposition," *Japanese Journal of Applied Physics*, vol. 50, p. 06GE12, 2011.

[62] G. Lippert et al., "Direct graphene growth on insulator," *Phys. Status Solidi B*, p. 1, 2011.

[63] A. Gupta et al., "Raman scattering from high-frequency phonons in supported n-graphene layer films," *Nano Letters*, vol. 6, no. 12, p. 2667, 2006.

[64] L. G. Cancado et al., "Influence of the atomic structure on the raman spectra of graphite edges," *Physical Review Letters*, vol. 93, p. 247401, 2004.

[65] L. G. Cancado et al., "Anisotropy of the raman spectra of nanographite ribbons," *Physical Review Letters*, vol. 93, no. 4, p. 047403, 2004.

[66] A. C. Ferrari, "Raman spectroscopy of graphene and graphite: disorder,electron-phonon coupling, doping and non-adiabatic effects," *Solid State Communications*, vol. 143, p. 47, 2007.

[67] L. M. Malard, "Thermal enhancement of chemical doping in graphene: a raman spectroscopy study," *J. Phys.: Condens. Matter*, vol. 22, p. 334202, 2010.

[68] R. Yang et al., "Substrate doping effects on raman spectrum of epitaxial graphene on sic," *Journal of Applied Physics*, vol. 107, p. 034305, 2010.

[69] S. Latil et al., "Massless fermions in multilayer graphitic systems with misoriented layers: Ab initio calculations and experimental fingerprints," *Physical Review B*, vol. 76, p. 201402 (R), 2007.

[70] D. M. Basko, "Theory of resonant multiphonon raman scattering in graphene," *Physical Review B*, vol. 78, p. 125418, 2008.

[71] A. C. Ferrari and J. Robertson, "Interpretation of raman spectra of disordered and amorphous carbon," *Physical Review B*, vol. 61, p. 14095, 2000.

[72] L. G. Cancado et al., "General equation for the determination of the crystallite size l_a of nanographite by raman spectroscopy," *Applied Physics Letters*, vol. 88, p. 163106, 2006.

[73] C. Faugeras et al., "Few-layer graphene on sic, pyrolytic graphite, and graphene: A raman scattering study," *Applied Physics Letters*, vol. 92, p. 011914, 2008.

[74] D. S. Lee et al., "Raman spectra of epitaxial graphene on sic and of epitaxial graphene transferred to sio_2," *Nano Letters*, vol. 8, p. 4320, 2008.

[75] D. Briggs and J. Grant, *Surface Analysis by Auger and X-ray Photoelectron Spectroscopy.* IM Publications and Surface Spectra Limited, Chichester, UK, 2003.

[76] C. S. Fadley, *Basic Concepts of X-ray Photoelectron Spectroscopy, Electron Spectroscopy: Theory, Techniques, and Applications Vol. 2.* Academic, New York, 1978.

[77] S. Doniach and M. Sunjic, "Many-electron singularity in x-ray photoemission and x-ray line spectra from metals." *J. Phys. C*, vol. 3, p. 285, 1970.

[78] D. A. Shirley, "High-resolution x-ray photoemission spectrum of the valence bands of gold," *Phys. Rev. B*, vol. 5, p. 4709, 1972.

[79] J. Robinson et al., "Nucleation of epitaxial graphene on sic (0001)," *ACS Nano*, vol. 4, p. 153, 2010.

[80] J. B. Hannon et al., "Pit formation during graphene synthesis on sic (0001): In situ electron microscopy," *Phys. Rev. B*, vol. 77, p. 241404(R), 2008.

[81] L. Muehlhoff et al., "Comparative electron spectroscopic studies of surface segregation on sic (0001) and sic ($000\bar{1}$)," *J. Appl. Phys.*, vol. 60, p. 2842, 1986.

[82] I. Gierz et al., "Electronic decoupling of an epitaxial graphene monolayer by gold interaction," *Phys. Rev. B*, vol. 81, p. 235408, 2010.

[83] C. S. Fadley, *Basic Concepts of X-ray Photoelectron Spectroscopy, Vol. 2 of Electron Spectroscopy: Theory, Techniques, and Applications.* Academic Press Inc., New York, 1978.

[84] S. Unarunotai et al., "Layer-by-layer transfer of multiple, large area sheets of graphene grown in multilayer stacks on a single sic wafer," *ACS Nano*, vol. 4, p. 5591, 2010.

[85] "Nist srd-82 ed.1.1," *National Institute of Standards and Technology, Gaithersburg, MD*, 2001.

[86] Z. H. Ni et al., "Raman spectroscopy of epitaxial graphene on a sic substrate," *Physical Review B*, vol. 77, p. 115416, 2008.

[87] J. Rohrl et al., "Raman spectra of epitaxial graphene on sic(0001)," *Applied Physics Letters*, vol. 92, p. 201918, 2008.

[88] D. J. Thouless, "Maximum metallic resistance in thin wires," *Phys. Rev. Lett.*, vol. 39, p. 1167, 1977.

[89] Turchanin et al., "Conversion of self-assembled monolayers into nanocrystalline graphene: structure and electric transport," *ACS Nano*, vol. 5, p. 3896, 2011.

[90] Nygard et al., "Electrical transport measurements in single-walled carbon nanotubes," *Appl. Phys. A*, vol. 69, p. 297, 1999.

[91] M. Huth et al., "Conductance regimes of w-based granular metals prepared by electron beam induced deposition," *New J. Phys.*, vol. 11, p. 033032, 2009.

[92] S. V. Morozov et al., "Strong suppresion of weak localization in graphene," *Phys Rev Lett*, vol. 97, p. 016801, 2006.

[93] X. S. Wu et al., "Weak antilocalization in epitaxial graphene: Evidence of chiral electrons," *Phys Rev Lett*, vol. 98, p. 136801, 2007.

[94] C. Tan et al., "Observation of electron weak localization and correlation effects in disordered graphene." *Sci China Ser G-Phys Mech Astron*, vol. 52, p. 1293, 2009.

[95] F. V. Tikhonenko et al., "Weak localization in graphene flakes," *Phys Rev Lett*, vol. 100, p. 056802, 2008.

[96] Y.-Y. Zhang et al., "Localization and the kosterlitz-thouless transition in disordered graphene," *Phys Rev Lett*, vol. 102, p. 106401, 2009.